

DESIGN, OPTIMIZATION AND STUDY ON MULTIPLE ELECTROCHEMICAL
SYSTEMS IN ENERGY DENSE RECHARGEABLE LITHIUM BATTERIES

A Dissertation

Submitted to the Faculty

of

Purdue University

by

Yi Cui

In Partial Fulfillment of the

Requirements for the Degree

of

Doctor of Philosophy

August 2019

Purdue University

West Lafayette, Indiana

THE PURDUE UNIVERSITY GRADUATE SCHOOL
STATEMENT OF COMMITTEE APPROVAL

Dr. Likun Zhu, Co-Chair

School of Mechanical Engineering

Dr. Liang Pan, Co-Chair

School of Mechanical Engineering

Dr. Partha P. Mukherjee

School of Mechanical Engineering

Dr. Peter J. Schubert

School of Electrical and Computer Engineering

Approved by:

Dr. Anil K. Bajaj

Head of Mechanical Engineering

This is dedicated to my parents, Junling Cui and Lei Yuan; my fiancée, Wei Cai, who love me, believe in me, inspire me and have supported me every step of the way.

ACKNOWLEDGMENTS

I would like to thank my ex-advisor Prof. Yongzhu Fu for the enlightenment into research, imparting knowledge, and his support, without whom I wouldn't start my Ph.D. study. I would like to acknowledge my advisor Prof. Likun Zhu for his extensive guidance, selfless assistance and strong support, without whom my dissertation would never be finished. He usually comes up with detailed ideas and novel views which help a lot for our experiments. Besides work, I also learned a lot from him to be an honest and passionate man in either life or research. I would also like to give acknowledgements to my co-advisor Prof. Liang Pan for his kind advice and help in my research. I would also like to appreciate the help from Prof. Partha P. Mukherjee and Prof. Peter J. Schubert for their advice and being my committee members. In addition, I would like to thank Prof. Ying Ma and Joseph D. Ackerson from University of Wisconsin-Eau Claire for being collaborators and providing me the first-principles calculation results, which is the support from the Materials Science program and the Materials Science and Engineering Centre at the University of Wisconsin-Eau Claire, in the phenyl selenosulfides project. I would like to thank Prof. Ruihua Cheng and Aaron Mosey from Physics Department for doing copper sputtering in the tin foil anode project. I would also like to acknowledge Dr. Yuzi Liu from Argonne National Laboratory for providing the transmission electron microscope (TEM) characterizations, which is supported by the U.S. Department of Energy, Office of Science, Office of Basic Energy Sciences, under Contract No. DE-AC02-06CH11357. I would also like to appreciate Prof. Amar H. Flood and Dr. Christopher R. Benson from Indiana University-Bloomington for being collaborators and providing me the cyanostar, control chemicals and UV-vis titration results in the polysulfide-selective molecular receptors for Li-S batteries project. I would like to thank Dr. Jonathan A. Karty from Indiana University-Bloomington for operating mass spectrometry (MS) and pro-

viding me the results. I would also appreciate the help from Prof. Wei Guo for her helps and advices in multiple projects.

In addition to those professors and scientists, I would also extend my special thanks to the previous and current members in our group. Dr. Cheolwoong Lim, Min Wu and Amruth Bhargav as previous group members helped me a lot on the battery test, characterization analysis and acquiring new ideas. Tianyi Li and Xinwei Zhou as current group members helped me a lot on battery projects, materials studies and electrochemical system designs. Finally, I would like to give my special thanks to Ms. Cathy Elwell, Mr. Jerry Mooney and Ms. Monica Stahlhut for their help on my dissertation formatting and deposition.

Finally, I would like to thank US National Science Foundation under Grant No. 1335850 and US National Science Foundation under Grant No. 1603847 for the support of the research project. I would also like to acknowledge the Integrated Nanosystems Development Institute (INDI) for use of their Bruker D8 Discover XRD Instrument, which was awarded through the NSF Grant MRI-1429241 and for use of their JEOL7800F Field Emission SEM, which was awarded through NSF Grant MRI-1229514. I would like to appreciate Purdue Research Foundation as fellowships for funding support.

TABLE OF CONTENTS

	Page
LIST OF TABLES	ix
LIST OF FIGURES	x
ABBREVIATIONS	xvi
ABSTRACT	xvii
1 INTRODUCTION	1
1.1 Motivation	1
1.2 Objectives	4
2 BACKGROUND AND LITERATURE REVIEW	6
2.1 Introduction of Lithium-ion Batteries (LIBs)	6
2.2 Introduction of Lithium-Sulfur Batteries (LSBs)	9
2.3 Introduction of Lithium-Selenium (Li-Se) Batteries	16
3 PHENYL SELENOSULFIDES AS CATHODE MATERIALS FOR RECHARGE- ABLE LITHIUM BATTERIES	21
3.1 Abstract	21
3.2 Introduction	21
3.3 Experimental	23
3.3.1 Materials and Instruments	23
3.3.2 Preparation of electrolyte and PDSe/S hybrid compounds	24
3.3.3 Preparation of PDSe, pristine S and PDSe/S hybrid electrodes	25
3.3.4 Cell fabrication and electrochemical evaluation	25
3.3.5 Characterizations	26
3.3.6 Computations	27
3.4 Results and Discussion	28
3.5 Conclusion	48

4	ELECTROCHEMICAL BEHAVIOR OF TIN FOIL ANODE IN HALF CELL AND FULL CELL WITH SULFUR CATHODE	49
4.1	Abstract	49
4.2	Introduction	49
4.3	Experimental	52
4.3.1	Materials and Instruments	52
4.3.2	Electrolyte preparation	53
4.3.3	Preparation of Sn anode and S cathode	53
4.3.4	Preparation of carbon-coated separator	54
4.3.5	Sn half-cell fabrication and electrochemical evaluation	55
4.3.6	S half-cell fabrication and electrochemical evaluation	55
4.3.7	Sulfur-tin full cell fabrication and electrochemical evaluation . .	56
4.3.8	Characterization	56
4.4	Results and discussion	57
4.5	Conclusion	73
5	SELENIUM NANOCOMPOSITE CATHODE WITH LONG CYCLE LIFE FOR RECHARGEABLE LI-SE BATTERIES	74
5.1	Abstract	74
5.2	Introduction	74
5.3	Experimental	76
5.3.1	Materials and Instruments	76
5.3.2	Preparation of electrolyte	78
5.3.3	Preparation of selenium nanowires/CNTs composite cathode . .	78
5.3.4	Cell fabrication and electrochemical evaluation	79
5.3.5	Characterizations	80
5.4	Results and Discussion	81
5.5	Conclusion	101
6	SUPPRESSION OF SHUTTLING IN LI-S BATTERIES USING POLYSULFIDE- SELECTIVE MOLECULAR RECEPTORS	102

	Page
6.1 Abstract	102
6.2 Introduction	102
6.3 Experimental	104
6.3.1 Materials and Instruments	104
6.3.2 Preparation of electrolyte and polysulfide catholyte	106
6.3.3 Preparation of S electrodes	106
6.3.4 Preparation of CS-coated separator and control compound-coated separators	106
6.3.5 Linear voltage sweep measurement	107
6.3.6 Cell fabrication and electrochemical evaluation	107
6.3.7 Characterizations	108
6.4 Results and Discussion	109
6.5 Conclusion	132
7 FUTURE WORK	133
7.1 Future Work on Solid Polymer Electrolyte (SPE) Project	133
7.2 Future Work on Liquid Metal Alloy Anode Project	133
REFERENCES	135
VITA	146

LIST OF TABLES

Table	Page
3.1 Materials	23
3.2 Instruments	24
4.1 Materials	52
4.2 Instruments	53
5.1 Materials	77
5.2 Instruments	78
6.1 Materials	105
6.2 Instruments	105

LIST OF FIGURES

Figure	Page
2.1 Schematic illustration of the commonly used Li-ion battery based on graphite anodes and LiCoO_2 cathodes (LiCoO_2 //electrolyte//graphite).	7
2.2 Voltage-capacity ranges for some cathode and anode materials.	9
2.3 Charge/discharge profile indicating intermediate products (various polysulfides) of a typical Li-S battery.	10
2.4 (a) Average mass density versus electrolyte/sulfur (E/S) ratio, (b) specific energy and energy density of sulfur cathode vary with the function of average mass density.	11
2.5 Illustration of the polysulfides shuttle effect occurring in a Li-S battery. . .	14
2.6 Schematic of the voltage profiles of a Li-Se battery in different electrolytes.	16
2.7 Illustration of lithiation and de-lithiation processes of Li-Se batteries. . . .	17
3.1 Schematic of addition reactions of phenyl diselenide (PDSe) with one sulfur atom to form phenyl selenosulfide (PDSe-S) and phenyl selenodisulfide (PDSe-S ₂). The values shown in the boxes are their theoretical specific capacities.	28
3.2 The reaction and energy difference of forming (a) PDSe-S and (b) PDSe-S ₂ .	30
3.3 Mass spectra of (a) PDSe-S and (b) PDSe-S ₂	31
3.4 DSC plots of DPSe, DPSe-S, and DPSe-S ₂	33
3.5 XRD patterns of PDSe, pristine sulfur, PDSe-S and PDSe-S ₂	34
3.6 Synthesized compounds stability for PDSe-S and PDSe-S ₂ at variable temperatures.	35
3.7 (a) cross-section SEM image and EDS showing (b) selenium and (c) sulfur mapping of the PDSe-S ₂ electrode.	36
3.8 SEM image of (a) the pristine carbon paper, (b) moderate magnification, (c) high magnification of PDSe-S electrode, (d-h) EDS scan for carbon, selenium, sulfur and overlapping, (i) SEM image of cross-section of PDSe-S electrode, (j-l) EDS scan on cross-section for overlapping, selenium and sulfur.	37

Figure	Page
3.9 Cyclic voltammogram of PDSe, PDSe-S, and PDSe-S ₂	38
3.10 Cyclic voltammogram of PDSe, S, and PDSe-S.	39
3.11 Voltage profile of PDSe, PDSe-S, and PDSe-S ₂	40
3.12 Voltage-capacity profile of (a) PDSe, (b) PDSe-S, and (c) PDSe-S ₂ at C/5 rate in different cycles.	41
3.13 Calculated energy efficiencies of PDSe, PDSe-S, and PDSe-S ₂	42
3.14 Redox reactions of (a) PDSe-S and (b) PDSe-S ₂ in rechargeable lithium batteries.	43
3.15 The lithiation reaction and energy difference of forming (a) PDSe-S-Li and (b) PDSe-S ₂ -Li.	44
3.16 Cyclic voltammogram of the 1 st , 2 nd , 5 th , and 10 th cycles of (a) PDSe, (b) PDSe-S, and (c) PDSe-S ₂	45
3.17 Cycling performance (a) of PDSe, PDSe-S, and PDSe-S ₂ at C/5 rate, rate performance (b) of PDSe-S and PDSe-S ₂ in rechargeable lithium batteries.	46
3.18 Coulombic efficiency (CE) of cells with PDSe, PDSe-S, and PDSe-S ₂ electrodes at C/5 rate.	48
4.1 (a) Cycling performance of the Sn foil at 0.03 C rate, (b) cyclic voltammogram of the 1 st , 2 nd , 5 th , and 10 th cycles.	57
4.2 (a) Voltage-capacity profile showing collected XRD patterns points, (b) XRD patterns of the Sn foil in the 1 st cycle.	58
4.3 XRD patterns of the Sn foil in the 2 nd cycle.	59
4.4 (a) Pictures showing the morphological changes from pristine Sn foil to lithiated product, the atomic structures of (b) Sn and (c) Li ₂₂ Sn ₅ . Tin and lithium atoms are represented in green and gray, respectively.	60
4.5 Voltage-capacity profile of the Sn foil at 10 $\mu\text{A cm}^{-2}$ current density.	61
4.6 Cycling performance of the Sn foil at 0.03 C rate with lithiation capacity limit of 2.04 mAh cm ⁻²	63
4.7 XRD patterns in the 1 st cycle of the Sn foil at 0.03 C rate with lithiation capacity limit of 2.04 mAh cm ⁻²	64
4.8 Selected voltage-capacity profiles of the Sn foil at 0.03 C rate with lithiation capacity limit of 2.04 mAh cm ⁻²	65
4.9 (a) SEM image and (b-c) EDS scan for carbon and sulfur in the sulfur cathode.	67

Figure	Page
4.10	Cycling performance of the sulfur cathode. 68
4.11	(a) Selected voltage-capacity profiles, and (b) cyclic voltammogram of the sulfur cathode. 69
4.12	(a) Picture of the Sn foil after pre-lithiation, (b) picture of the Sn foil, (c) SEM image and (d-g) EDS scan for overlapping, nitrogen, oxygen and tin for the Sn foil anode at discharged state after 10 cycles in the S-Sn full cell. 70
4.13	Cycling performance with an inset schematic of construction of the S-Sn full cell. 71
4.14	(a) Selected voltage-capacity profiles and (b) cyclic voltammogram of the S-Sn full cell. 72
5.1	Schematic of the experimental procedure synthesizing the selenium nanowire and CNT composite electrode, with the SEM image showing the morphology of the composite electrode. 81
5.2	EDS scan for (a) carbon and (b) selenium of the selenium nanowire/CNT composite electrode. 82
5.3	(a) TEM image, (b) HRTEM image and (c) SAED pattern of the synthesized selenium nanowires. 82
5.4	TGA plots of the initial (a) SeCE-1, (b) SeCE-2 and (c) TSeCE. 83
5.5	DSC plots for (a) SeCE-1, SeCE-2 and pure Se comparisons and (b) TSeCE and pure Se comparisons, respectively. 84
5.6	(a) Cross-section SEM image of the initial SeCE-2, (b) XRD patterns of the composite electrode at different states of cycling. 86
5.7	Cycling performance of SeCE-1 and SeCE-2 at 1C rate. 87
5.8	(a) Surface SEM image of SeCE-2 at discharged state, (b-d) EDS scan for selenium, carbon and oxygen, respectively. 88
5.9	(a) Surface SEM image, (b) cross-section SEM image and (c) EDS showing selenium of the SeCE-2 at the discharged state. 89
5.10	EDS scan for (a) carbon and (b) oxygen at cross-section of the SeCE-2 at the discharged state. 90
5.11	(a) Surface SEM image of SeCE-2 at charged state, (b-d) EDS scan for selenium, carbon and oxygen, respectively. 91
5.12	(a) Surface SEM image, (b) cross-section SEM image and (c) EDS showing selenium of the SeCE-2 at the charged state. 92

Figure	Page
5.13 EDS scan for (a) carbon and (b) oxygen at cross-section of the SeCE-2 at charged state.	92
5.14 (a) Cross-section SEM image, (b) EDS showing selenium of the initial TSeCE, (c) cross-section SEM image, (d) EDS showing selenium of the TSeCE at the discharged state, (e) cross-section SEM image and (f) EDS showing selenium of the TSeCE at the charged state.	94
5.15 EDS scan for (a) overlapping and (b) carbon at cross-section of the TSeCE before cycling.	96
5.16 EDS scan for (a) carbon and (b) oxygen at cross-section of the TSeCE at discharged state.	97
5.17 EDS scan for (a) carbon and (b) oxygen at cross-section of the TSeCE at charged state.	98
5.18 (a) Cycling performance and (b) voltage profile of the TSeCE at 1C rate in rechargeable lithium batteries.	98
5.19 (a) Cyclic voltammogram and (b) rate performance of the TSeCE in rechargeable lithium batteries.	99
5.20 Nyquist plots of the SeCE-2 and TSeCE (a) before cycling, (b) after discharge and (c) after charge with inset pictures showing the intercepts in the high-frequency regions.	100
6.1 (a) Chemical structures of cyanostar, sulfur (S_8) and tetrasulfide dianion (S_4^{2-}). (b) scheme showing the diffusion of various polysulfides out of sulfur cathodes and through standard separators. (c) scheme showing the introduction of cyanostar into separator pores and its role in binding polysulfides to stop their shuttling over to the anode.	109
6.2 (a) Cartoon representation showing the host-guest association of polysulfides with cyanostar; only one possible inclusion complex is shown for simplicity, (b) isotopic splitting patterns observed in the ESI-MS titration compared with the predicted distribution.	110
6.3 Spectra of the UV-Vis titration following the addition of polysulfide to a solution of cyanostar.	112
6.4 Cyclic voltammetry (CV) experiments as a model for sulfur cathodes. (a) CV sweep of a solution of S_8 . (b) CV sweep of a solution of S_8 with 6 equivalents of cyanostar added. Conditions: 1 mM sulfur (S_8), 0.1 M TBA(TFSI) electrolyte solution (CH_2Cl_2), 1 mm glassy carbon working electrode, platinum wire counter electrode, polished silver wire pseudoreference.	114

Figure	Page
6.5 SEM image of (a) surface morphology and (b) cross-section.	116
6.6 Low magnified SEM image of the CS-coated separator.	117
6.7 Current density-voltage profile of cells with 0.25 M polysulfide solution and pristine Celgard 2400, pure PVdF-coated separator and CS-coated separator at voltage sweeping rate of 1.0 mV s^{-1}	118
6.8 (a) Cycling performance and (b) Coulombic efficiency (CE) of cells with pristine separator and CS-coated separator at C/10 rate, selected voltage profile for (c) pristine separator and (b) CS-coated separator in rechargeable lithium batteries.	119
6.9 (a) Cycling performance and (b) selected voltage profile of cells with pure PVdF-coated separator at C/10 rate.	121
6.10 (a) Cycling performance and (b) selected voltage profile of cells with curcubit[6]uril-coated separator at C/10 rate.	122
6.11 (a) Cycling performance and (b) selected voltage profile of cells with β -cyclodextrin-coated separator at C/10 rate.	123
6.12 (a) Cycling performance and (b) Coulombic efficiencies of cells with variable sulfur loading cathodes and CS-coated separator at C/10 rate. . . .	124
6.13 Rate performance of cells with 1.0 mg sulfur cathode and CS-coated separator.	126
6.14 (a) Picture of the lithium anode side of the separator, (b) picture of the lithium metal surface, (c) SEM image of the separator of the lithium anode side, EDS showing (d) overlap elemental mapping, (e) sulfur, (f) carbon and (g) oxygen of the cells with pristine separator at discharge state. . .	127
6.15 (a) Picture of the lithium anode side of the separator, (b) picture of the lithium metal surface, (c) SEM image of the separator of the lithium anode side, EDS showing (d) overlap elemental mapping, (e) sulfur, (f) carbon and (g) oxygen of the cells with pristine separator at charge state. . . .	128
6.16 (a) Picture of the lithium anode side of the separator, (b) picture of the lithium metal surface, (c) SEM image of the separator of the lithium anode side, EDS showing (d) overlap elemental mapping, (e) sulfur, (f) carbon and (g) oxygen of the cells with CS-coated separator at discharge state. .	129
6.17 (a) Picture of the lithium anode side of the separator, (b) picture of the lithium metal surface, (c) SEM image of the separator of the lithium anode side, EDS showing (d) overlap elemental mapping, (e) sulfur, (f) carbon and (g) oxygen of the cells with CS-coated separator at charge state. . .	130

6.18	Picture of the lithium anode side of the separator at (a) discharge state, (f) charge state, picture of the lithium metal surface at (b) discharge state, (g) charge state, SEM image of the separator of the lithium anode side at (c) discharge state, (h) charge state, EDS showing overlap elemental mapping and sulfur at (d,e) discharge state, (i,j) charge state of the cells with PVdF-coated separator.	131
------	---	-----

ABBREVIATIONS

LIBs	Lithium-ion batteries
LSBs	Lithium-sulfur batteries
Li-S	Lithium-sulfur
Li-Se	Lithium-selenium
PEDs	Portable electronic devices
LPF	Lithium iron phosphate (LiFePO_4)
NMC	Lithium nickel cobalt manganese oxides
LMO	Lithium manganese oxide
EVs	Electronic vehicles
CS	Cyanostar
PS	Polysulfides
AMD	Average mass density
CE	Coulombic efficiency
PDSe	Phenyl diselenide (PhSeSePh)
PDSe-S	Phenyl selenosulfide (PhSe-S-SePh)
PDSe-S ₂	Phenyl selenodisulfide (PhSe-SS-SePh)
CNTs	Carbon nanotubes
SeCE	Selenium composite electrode
TSeCE	Thin selenium composite electrode
LVS	Linear voltage sweep

ABSTRACT

Cui, Yi. Ph.D., Purdue University, August 2019. Design, Optimization and Study on Multiple Electrochemical Systems in Energy Dense Rechargeable Lithium Batteries. Major Professors: Likun Zhu, Liang Pan.

Lithium-ion batteries (LIBs) are commonly and widely applied in current numerous devices such as smart phones, laptops, electric vehicles and medical devices. The LIBs are considered as a mature technology in today's commercial market benefited from their uncomplicated lithium intercalation and de-intercalation reactions, stable cycling performance and good working life as energy storage devices and power resources. However, the conventional LIBs with technical limits such as high weight, low lithium utilization and low specific energy density hit the bottlenecks of further improvements and optimizations for meeting the growing power supply requirements. It is urgent to develop the second generations of rechargeable lithium batteries, which have the benefits of low cost, high specific capacity and high energy density with light weight.

In this context, lithium-sulfur batteries (LSBs) and lithium-selenium (Li-Se) batteries attract much attention due to the high possibility to meet the requirements of high specific capacity and high energy density. However, the technical challenges they are facing put some barriers before they can be successfully commercialized. By a brief summary, the challenges to be solved are current low energy density because of requiring large amount of liquid electrolyte, the highly flammability and unsafety of lithium metal, low active material content due to the necessary requirement of carbon and binder, and severe so-called shuttle effect resulting in low Coulombic efficiency. Before solving these challenges, Li-S batteries or Li-Se batteries are unlikely to be successfully commercialized in our market. Therefore, numerous research is aimed at

solving the challenges and further developing more advanced Li-S and Li-Se battery systems.

In the present dissertation, the contributions are mainly focused on sulfur-based and selenium-based materials, which aim to solve the current existing challenges and improve the battery performance, herein obtain a higher potential for application. Four chapters are included in this dissertation, which aim to present the four studied projects. The first research conducted in this dissertation is developing organo S/Se hybrid materials which require low E/S ratios of liquid electrolyte and show light shuttle effect, therefore indicate promising high energy density and cycling life. Secondly, the tin foil is used as lithium sources instead of metallic lithium anode, then incorporated with sulfur cathode as a full cell. The full cell design provides the potential using a metallic anode other than pure lithium and increase the safety factor of a battery system. In addition, nano-scale selenium/carbon nanotubes composite electrode is synthesized via a chemical reduction method. With the optimization on thickness of the composite electrodes, the Se cathode has an active material content of $\sim 60\%$ and shows stable long cycling life with maximizing the utilization of selenium. The final research conducted in this dissertation is applying a macro molecule named cyanostar, which has the ability to chemically bind with polysulfide species, thereupon to alleviate the shuttle effect in Li-S batteries. With the evidence from chemistry analysis and electrochemical comparison results presented in this dissertation, cyanostar is proven to have the potential for further applications in Li-S batteries.

1. INTRODUCTION

1.1 Motivation

During the information era, many world organizations tried to develop green energy storage technologies (e.g., batteries, wind power technology, solar cell, nuclear power, etc.) in response to the immense consumption of coal and fossil fuel, and the consequent environmental contamination. Among them, battery became a promising technology due to its high efficiency, low maintenance cost and large energy density [1]. In the 1970s, before the successful commercialization of lithium-ion batteries (LIBs), Dr. M. Stanley Whittingham at Binghamton University was the first scientist who proposed the concept of lithium-ion batteries by applying intercalations between titanium disulfide and lithium metal [2]. However, the high activity and unsafety of lithium limit the practical application for such system. In 1979, Dr. John B. Goodenough at University of Texas at Austin found that LiCoO_2 has the ability to accept and release lithium ions as a replacement of pure lithium metal [3]. In 1980, graphite was found to be able to have reversible lithium intercalation electrochemical behaviors in organic electrolyte by Rachid Yazami [4]. Then graphite was further studied and used as lithiated graphite anode for battery system by two scientists at Illinois Institute of Technology, Dr. Agarwal and Dr. Selman. With the knowledge of applying the combination of LiCoO_2 cathode and lithiated graphite anode, SONY firstly succeeded in commercially inventing the lithium-ion batteries in 1991, which was a revolutionary invitation that could work as reliable rechargeable batteries for multiple portable electronic devices (PEDs). At the end of the 20th century, LIBs with better cycling life and higher safety were required for the rapid growing market. Olivine structure material such as lithium iron phosphate (LiFePO_4 , LPF) had been proposed as a cathode material [5]. With the modification of LiFePO_4 into nano-

scale particles, the capacity and cycling performance of LIBs were further improved. Advancing toward to the 21st century, the landscape of using renewable energy as a green energy in motor vehicles was greatly increased, which requires the development of LIBs with better cycling life and higher energy density. Numerous efforts have been put into the studies of cathode materials for LIBs. Many intercalation type materials, such as lithium nickel cobalt manganese oxides (NMC) [6, 7], lithium manganese oxide (LMO) [8–10] and Vanadium oxide (V_2O_5) et al. [11, 12], have been developed for rechargeable batteries. Nowadays, many types of lithium-ion batteries are widely applied as indispensable energy resources in peoples daily existences and activities.

However, the cathode materials in LIBs hit a bottleneck and share a common weakness which is the low specific capacity between 150-300 mAh g^{-1} [13]. In the meantime, the required capacity that LIBs need to provide for devices keeps growing every day. On one hand, without the materials that can provide high energy densities and specific capacities, it becomes impossible to develop advanced PEDs and long-driving-distance electric vehicles (EVs) for each charge while maintaining the weight and the amount of the used batteries at a low level. The low electron transfer number (usually less than 1) during charge and discharge intercalation process put a barrier for the provided specific capacity of most lithium-ion battery materials. On the other hand, the cost of most materials in lithium-ion batteries are kept at a high level. Using these materials makes the product prices not easy to decrease to an affordable level. Therefore, developing new cathode materials that can provide high specific capacity and energy density for rechargeable batteries becomes an urgent target for the growing demand of daily energy supply for PEDs and EVs. Some materials with low molecular weight, high electron utilization and chemical reaction during charge/discharge process attract much attention for studies. For conventional LIBs, only lithium intercalation/de-intercalation process happens based on the lithium ions transportation between metal oxide cathode and lithiated graphite anode. In this process, the cathode structure could totally collapse resulting in incorporation of

lithium ions, which makes the electrochemical system irreversible and the battery performance fading. Unlike the intercalation cathode materials, the new materials will have chemical reactions with lithium, convert into new products and change to new structures. In the conversion process, the product can release the lithium to make the electrochemical system reversible.

In such a context, sulfur (S) and selenium (Se) attract much attention as promising candidates for cathode materials. Sulfur can provide a much higher specific capacity of 1672 mAh g^{-1} comparing to lithium-ion battery cathode materials [14, 15]. In comparison with sulfur, Se has a lower specific capacity of 675 mAh g^{-1} , but it is still higher than most cathode materials in LIBs [16]. In addition, sulfur has a high theoretical specific energy of 2600 Wh kg^{-1} , which could potentially be 2-3 times higher than LIBs ($300\text{-}500 \text{ Wh kg}^{-1}$) [17]. On the other hand, selenium has a high volumetric capacity density of 3253 mAh cm^{-3} , which is almost the same of that for Li-S batteries (3467 mAh cm^{-3}), due to the high mass density of selenium (4.8 g cm^{-3}) [18]. Besides these advantages, sulfur as a cathode material has low cost, abundance and environmental benignity benefits, which has the potential decreasing the total cost of a battery. On the other hand, selenium has a high conductivity ($1 \times 10^{-3} \text{ S m}^{-1}$), which provides the potential to develop pure selenium cathode or electrode with low carbon content [19]. The energy density of Li-Se batteries could potentially be higher than the cathode materials in LIBs. However, both Li-S and Li-Se batteries are facing some unsolved technical challenges which prevent them from practical applications. The challenges in Li-S batteries, such as the so-called shuttle effect, volume expansion, poor electronic conductivity, unsafety of using pure lithium metal and requirement of large amount of liquid electrolyte, are the target issues waiting to solve. In Li-Se batteries, the similar polyselenides shuttle effect, volume expansion and materials loading in electrodes put barriers in front of practical applications. As a prospect, numerous studies and much effort for Li-S and Li-Se batteries have been made in recent years. At the same time, significant advancements have been achieved for such two electrochemical systems. To successfully make the

high energy dense Li-S and Li-Se batteries commercialized for daily growing energy demands, more fundamental studies and solutions are required for solving the existing challenges.

1.2 Objectives

This dissertation has been separated into several parts based on Li-S batteries and Li-Se batteries. Each part is trying to understand, study and solve one issue to further improve the battery performance, hence further improve the potential for practical application. Below are the main objectives included in this dissertation in detail:

- Development of organo selenosulfides ($R_2-Se_x-S_y$) hybrid compounds as cathode materials for rechargeable lithium batteries.
- Study on tin (Sn) foil as an anode material and incorporating with sulfur (S) cathode to form S-Sn full cells.
- Chemical synthesis of selenium (Se) nanowires with carbon nanotubes (CNTs) as nanocomposite cathode in rechargeable Li-Se batteries.
- A macrocycle molecule: cyanostar (CS) as membrane materials to suppress the polysulfides (PS) shuttle effect in Li-S batteries.

Various characterization methods have been applied to achieve the objectives, as shown below:

- Battery (coil cell type) cycling test on Arbin BT2000 battery cycler.
- Cyclic voltammogram (CV) test.
- Nyquist analysis.
- Thermal gravity analysis (TGA) and differential scanning calorimetry (DSC) analysis.
- Powder X-ray diffraction (XRD).
- Mass spectrometry (MS) analysis.

- Scanning electron microscope (SEM).
- Transmission electron microscope (TEM).
- Study and understanding on first-principles calculations based on density functional theory (DFT).
- UV-vis titration analysis.

2. BACKGROUND AND LITERATURE REVIEW

2.1 Introduction of Lithium-ion Batteries (LIBs)

In the second half of the 20th century, the trepidation about the excessive consumption of the limited fossil fuels and the rapid increased demand for the electric energy motivated us to develop new energy storage devices. Diverse primary batteries were first successfully invented for use as convenient energy resource. However, the disposal for them after use was a big waste of resources, and also caused the environmental hazards and concerns. Later on the rechargeable batteries (also called secondary batteries) were developed and put into the market to meet the requirements of reusing the batteries. Multiple types of rechargeable batteries, such as lead acid batteries, nickel hydride batteries, nickel zinc batteries and nickel cadmium batteries, were widely applied in portable electronic devices (PEDs) and vehicles. But the disadvantages of this generation of rechargeable batteries limit the further application in advanced electronic devices. For instance, the memory effect, low capacity, low efficiency and heavy weight drive people to invent new generation of rechargeable batteries.

The invention of lithium-ion batteries (LIBs) by SONY in 1991 was a revolutionary event at the end of the 20th century. LIBs are energy storage devices that can convert electrical energy into chemical energy stored by electrode materials upon charging and release it in the form of electrical energy. In addition, the simple lithium insertion reactions between cathode and anode make LIBs highly controllable and highly efficient [20]. In comparison with the primary batteries and previous generation of secondary batteries, LIBs have many obvious advantages. For example, LIBs have much higher efficiency than the other rechargeable batteries. The specific capacity and energy density are higher than the previous secondary batteries. LIBs have no

such memory effect but have much longer cycle life and shelf life [21]. These advantages make the LIBs successfully commercialized and to conquer the market in PEDs and electric vehicles for almost 40 years.

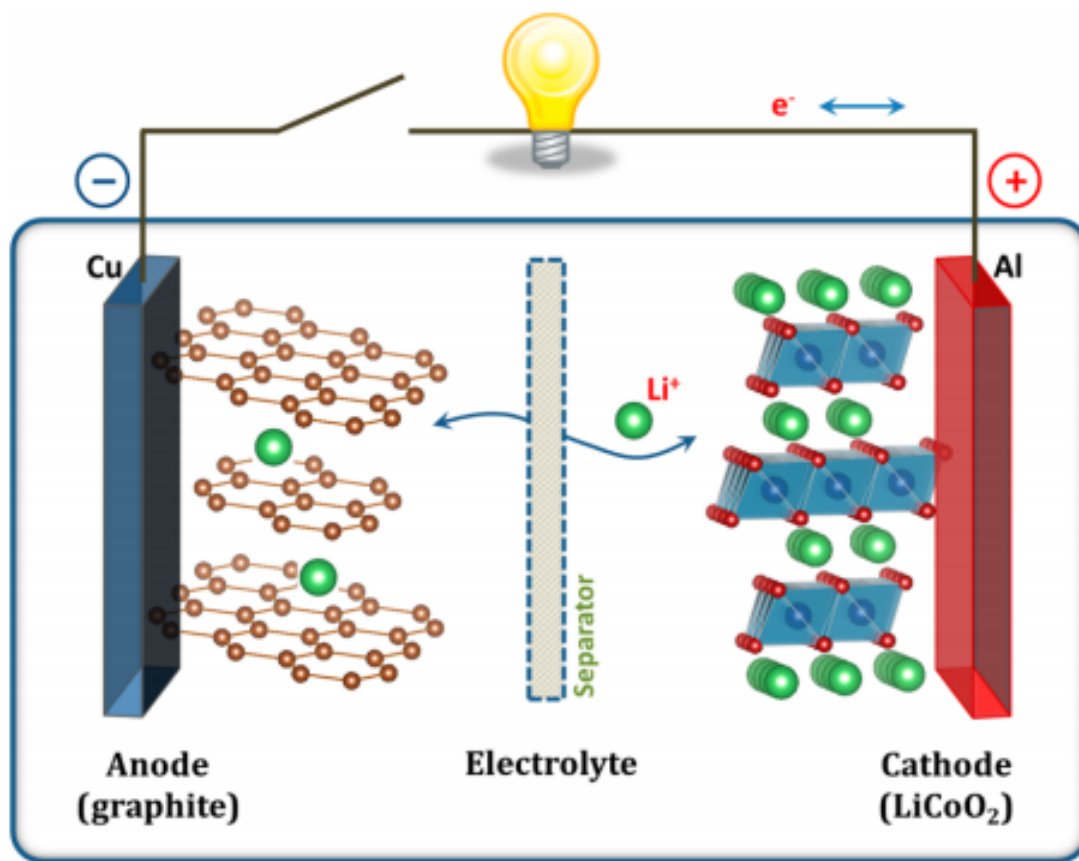
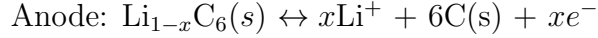


Figure 2.1. Schematic illustration of the commonly used Li-ion battery based on graphite anodes and LiCoO_2 cathodes (LiCoO_2 //electrolyte//graphite).

Figure 2.1 illustrates a basic LIB system that is the most widely and commonly used in current battery market [22]. A typical Li-ion battery consists of four major components, which are cathode, membrane (also called separator), anode and electrolyte. The major battery reactions are the reversible lithium cations intercalation and de-intercalation cycles between two layered materials. The cathode and anode reactions are shown below:



$$0 \leq x \leq 1$$

In order to ensure the stability of cathode material (LiCoO_2), the lithium extraction number is usually limited to up to 0.5 or the potential of delithiation is limited to 4.2 V, which means common obtained capacity is only half of the theoretical capacity by converting LiCoO_2 to $\text{Li}_{0.5}\text{CoO}_2$. For the LIBs, the first process is always the charging process, in which the cathode side has oxidation and delithiation, and the graphite anode material has the reduction and lithiation to form LiC_6 as the final product. In the discharge, the lithium cations (Li^+) are released from the anode side and the stored back to the Li_xCoO_2 cathode. At the meantime, the electrons will travel from anode to cathode via the external circuits so that the electrical energy will be delivered to devices. As mentioned above, the transportation mechanisms and the lithium sources of the metal oxides materials ensure a very long cycling life and excellent safety operations. With these advantages discussed above, LIBs have been undoubtedly become the best choice as power sources in PEDs and EVs.

However, looking to the future, there are still some doubts for LIBs to provide the power for worlds need. For some applications such as transportations and grids, the short age of Li metal and the transition metals currently used could be an issue. In addition, the LIBs are costly at present, which increases the difficulty of widely using them. The costs of manufacturing LIBs and the prices of cobalt make the LIBs more expensive for use. One the other hand, the rapid growth that requiring high energy density delivery, low cost, having large volume but light in weight for advanced electrical devices exceeds the limit of LIBs. The limited provided electrons in each molecule of the most cathode materials in LIBs barriers the overall specific capacity. The high molecular weight of the transition metal compounds increases the overall weight, herein decreases the overall energy density. Therefore, exploring new battery materials with high specific capacity and high energy density are urgent and required.

2.2 Introduction of Lithium-Sulfur Batteries (LSBs)

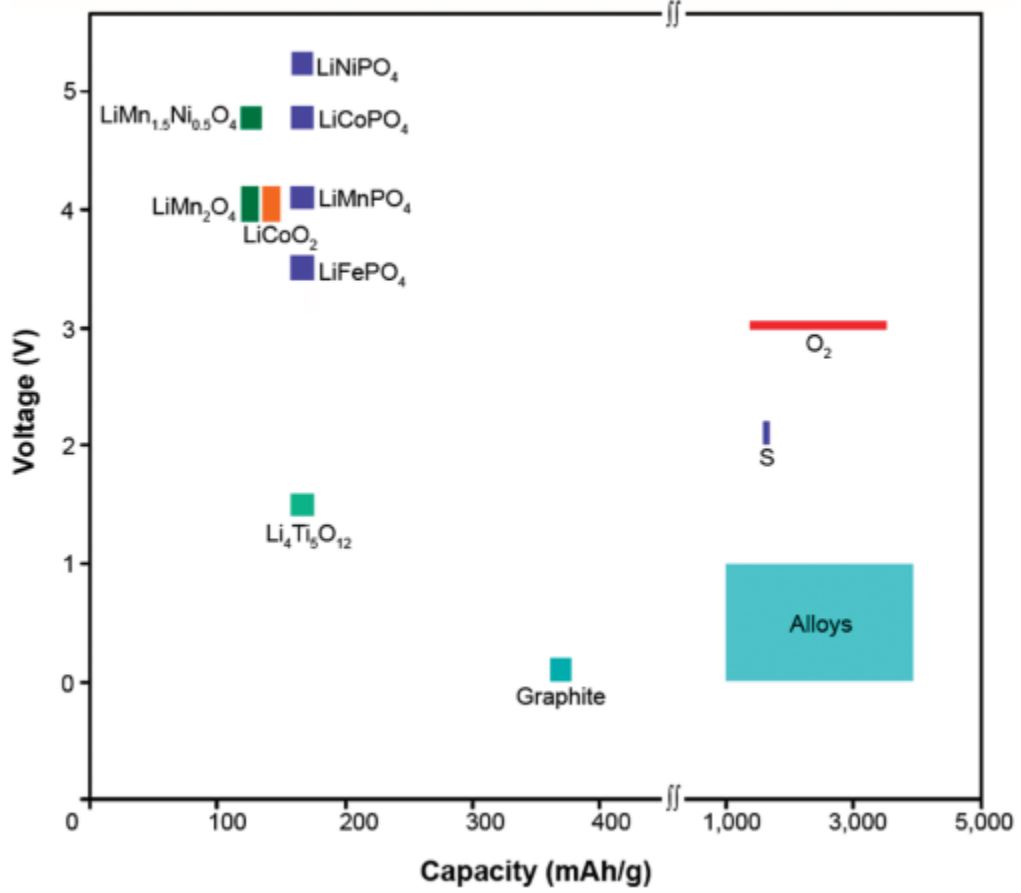


Figure 2.2. Voltage-capacity ranges for some cathode and anode materials.

Over the past decades, rechargeable lithium-sulfur (Li-S) batteries have become an important energy storage system. Sulfur has an extremely high theoretical specific capacity of 1672 mAh g^{-1} , which is much higher than the LIBs cathode materials, as shown in **Figure 2.2** [23]. In addition, the provided specific energy of sulfur can potentially reach a theoretical number of 2600 Wh kg^{-1} , which is almost double or triple of that of the LIBs. Another unique advantage is the combination of sulfur with lithium, which provides a large specific capacity of 3860 mAh g^{-1} as an anode material [24]. This combination of two large-capacity materials highly improves the

energy density. Besides these advantages, sulfur as a cathode material has low cost, abundance and environmental benignity benefits, which has the potential decreasing the total cost of a battery [25]. Due to the multiple advantages, much effort has been put in developing Li-S electrochemical systems via numerous paths and directions [26–31].

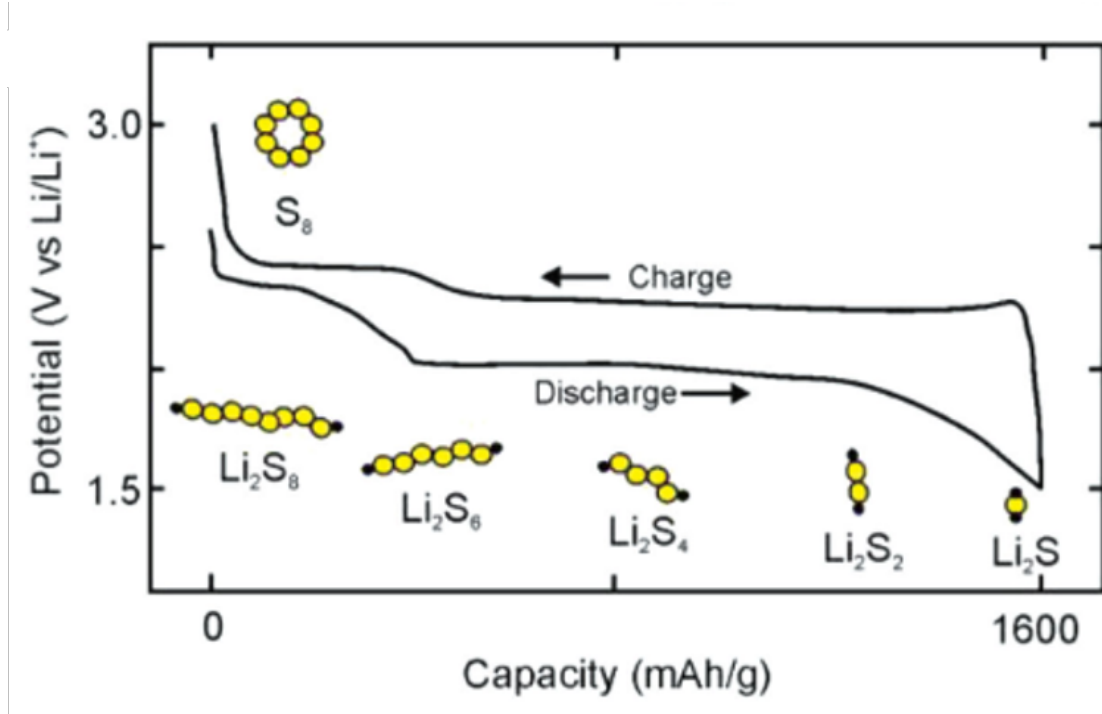
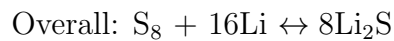


Figure 2.3. Charge/discharge profile indicating intermediate products (various polysulfides) of a typical Li-S battery.

In the Li-S electrochemical system, sulfur undergoes through a series of electrochemical redox reactions with lithium anode. **Figure 2.3** shows the discharge and charge reactions in a typical Li-S battery [32]. The overall reactions can be simply described by the follow equation:



If considering the formation of polysulfides (PS) as liquid intermediates, the overall reaction can be described by the follow equation:

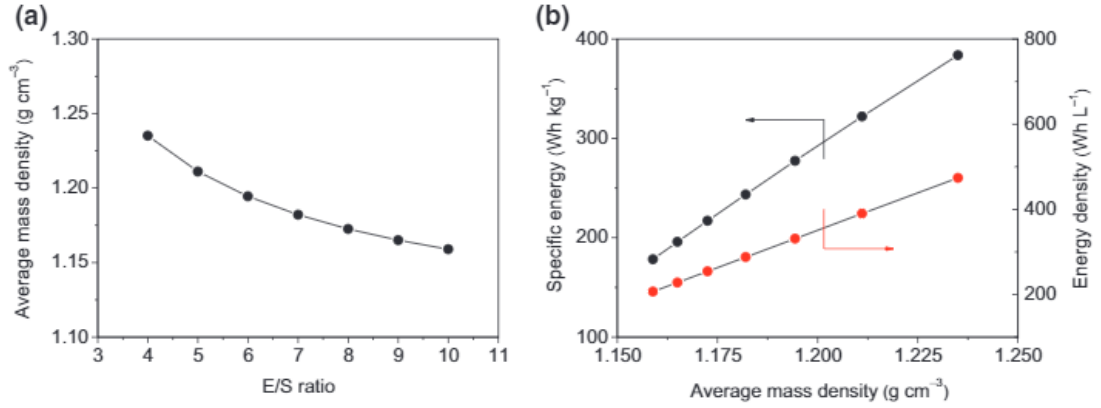
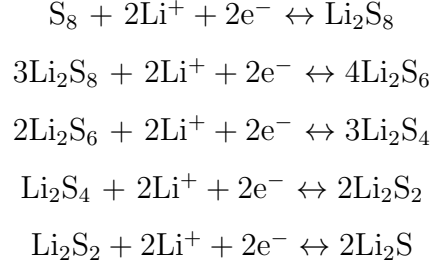


Figure 2.4. (a) Average mass density versus electrolyte/sulfur (E/S) ratio, (b) specific energy and energy density of sulfur cathode vary with the function of average mass density.

However, Li-S batteries are still facing some technical challenges from their widespread applications. For the Li-S batteries, the first challenge is to minimize the electrolyte/sulfur (E/S) ratio. Guo et al. highlighted the relation between the real energy density and applicable amount of electrolyte, also the relation between the energy density and mass of active materials in ref. [33]. **Figure 2.4** shows relations between the average mass density (AMD) of sulfur with the amount of using liquid electrolyte, and the obtained specific energy and energy density as a function of the AMD of sulfur. In a Li-S liquid battery, the E/S ratio is a critical factor in

determining the energy density. On the other hand, the cycling performance in Li-S batteries are greatly affected by the used amount of liquid electrolyte due to the effects by concentration of the dissolved polysulfides and the contingent disproportionation of polysulfides in the electrolyte solutions. Therefore, the AMD can be introduced to evaluate the specific energy and energy density of Li-S batteries. From a literature, the AMD of a sulfur cathode decreases when the E/S ratio increases. Two important targets, specific energies (Wh kg^{-1}) and energy densities (Wh L^{-1}), are functions of the active materials (here is sulfur, S) in the electrode, which can be calculated by AMD. By evaluation, when the AMD is $\sim 1.24 \text{ g cm}^{-3}$ corresponding to an E/S ratio of $4 \mu\text{L mg}^{-1}$, the Li-S battery can contribute approximately 400 Wh kg^{-1} specific energy and 500 Wh L^{-1} energy density, which are close to those of LiCoO_2 cathode in Li-ion batteries. Several studies operate the Li-S batteries with a low E/S ratio ($< 4 \mu\text{L mg}^{-1}$), but they show fast faded cycling performance and low sulfur utilization. Much effort has been made to understand the E/S mechanisms and to obtain a high energy density with low E/S ratio electrolyte for Li-S batteries. For instance, Hagen et al. studied the relationships between the cell energy density and the electrolyte/sulfur ratio in ref. [34]. Luo et al. studied and calculated the cell energy densities based on the active materials used in a whole battery system by various calculation perspectives, which includes or excludes the separator mass, anode mass and electrolyte mass in ref. [35]. Zhang optimized the E/S ratio herein obtained an improved cycling life in ref. [36]. Fan et al. studied the effect of applying low E/S ratios in battery on electrodeposition kinetics in ref. [37]. Therefore, different paths have been developed to obtain high energy density with low E/S ratio. For instance, the materials of organo-sulfide families and metal polysulfide materials can be alternative cathode materials instead of sulfur cathode [38]. In addition, Fu's group has studied different organo-sulfides and organo-selenides materials in organo cathode materials family for rechargeable batteries [39–45]. The organo materials can provide a stable cycling performance and high energy density by using low amounts of electrolyte. Therefore, optimizing Li-S batteries with low E/S ratio and promising

cycle life is an important research direction to obtain high specific energy and energy density, which could make Li-S batteries compete with conventional Li-ion batteries.

The second challenge is the highly flammability and unsafety concern of using pure lithium (Li) metal anode. Li metal has been known to greatly affect the safety of Li-S batteries [46,47]. With the lifted temperature during the charging process, the thermal runaway of Li metal arises the chemical reactions with polysulfides, including the possible side reactions with electrolyte solvent and oxygen/water from air. Therefore, replacing the Li metal anode with other lithium resource is an effective approach to enhance the safety of Li-S batteries [48,49]. For instance, one idea from the applications of LIBs using lithiated carbon anode (Li_xC_6) has been proposed, in which the lithium transportation is kinetically limited at a low level [50]. In addition, the much higher melting point of Li_xC_6 than pure lithium metal further increases the safety factor for using carbon-based anode [51]. Many other approaches are also developed for safer anode design, such as applying tin (Sn) metal, tin dioxide (SnO_2), germanium (Ge) and silicon (Si) anodes et al. to incorporate with appropriate cathode materials. Hassoun et al. evaluated the safety of using Sn-C anode incorporated with $\text{LiNi}_{0.5}\text{Mn}_{1.5}\text{O}_4$ cathode in ref. [52], in which the battery undergoes good stability without thermal decomposition at nearly 200 °C. Liu et al. employed a SnO_2 anode for Li-S batteries to obtain a highly safed electrochemical system in ref. [53]. Liu et al. developed silicon nanowires for lithium-ion batteries in [54], in which the silicon provides high capacity and stability as a replacement of pure lithium metals. On the other hand, Ge-based, Si-based and Ti-based anodes are also promising possibilities for replacing metallic lithium, which are included in various contributions [55–61]. These anode materials are applicable for Li-S batteries, in which the Li-Sn, Li-Ge and Li-Si alloys can limit the lithium release and donate the equivalent lithium ions to Li_2S or sulfur for redox reactions, herein assumed to highly improve the safety for Li-S batteries.

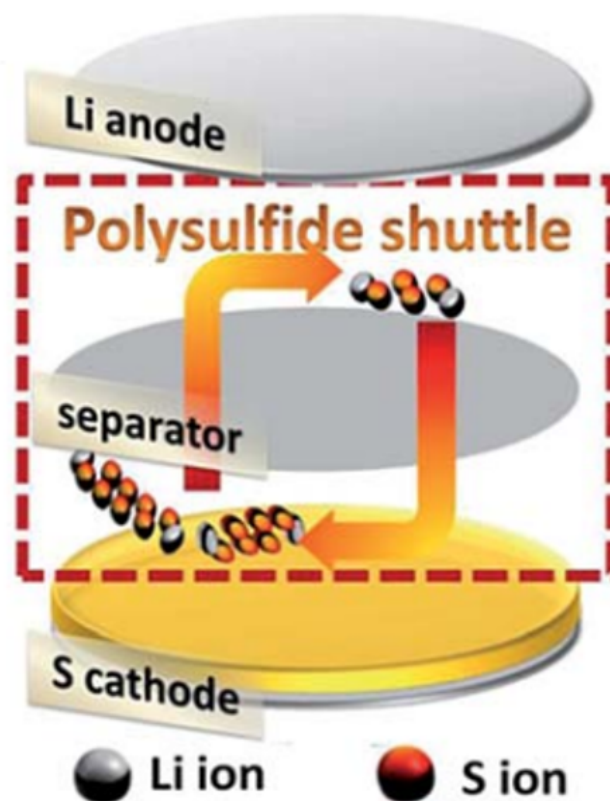


Figure 2.5. Illustration of the polysulfides shuttle effect occurring in a Li-S battery.

The third primary challenge is the so-called shuttle effect, as shown in **Figure 2.5** [62]. In the charging process, high-order soluble polysulfide species ($\text{Li}_2\text{S}_{6-8}$) will be formed and transport through the separator to the lithium metal anode. The soluble high-order polysulfide species can be electrochemically and chemically reduced by lithium to form short-chain polysulfide species, which then participate into repeated charging reactions, herein results in low Coulombic efficiency (CE) for charging [63]. The shuttle effect also causes the huge consumption of sulfur during cycling, corrosion of lithium metal and unexpected polarization of lithium anode [64]. LiNO_3 is first discovered to have the ability forming a passivation layer on lithium metal surface, therefore prevent the polysulfides shuttle effect in 2008-2009 [65]. After that the LiNO_3 is widely and commonly used as additives in organic electrolyte for Li-S batteries, herein prevents the polysulfides redox reactions on the lithium metal

to stop the shuttle effect [66]. However, the continuous consumption of LiNO_3 leads to kept decreased amounts of additives and ultimate faded performance [67]. Many other approaches have been made to solve the shuttle issues discussed above. The first promising approach is using physical barrier layers such as carbon, metal-oxides and functional materials for absorption and trapping the dissolved polysulfides. Chung et al. developed polymer supported carbon coating separator as a polysulfides trap to stop the shuttle effect in ref. [68]. Kong et al. created MnO_2 /graphene oxide/carbon nanotube interlayers as shields for trapping the polysulfide shuttle effect in ref. [69]. Al Salem et al. used catalyst nanoparticles for absorption of polysulfide species, therefore trapping the polysulfide shuttle effect in ref. [70]. On the other hand, another area is using functional polymers, bifunctional materials and developing new membranes to suppress the shuttle effect [71–76]. Other than that, a chemical concept has been proposed to bond with polysulfides or sulfur to maintain all the sulfur at the cathode side. Therefore, applying a specific chemical which has binding ability to polysulfide species or shows strong affinity could also be an efficient way to trap the polysulfides, herein suppresses the shuttle effect.

Besides the challenges discussed above, the other challenges are the insulating nature of sulfur, and the poor conductivity of the discharge products Li_2S and Li_2S_2 ($3 \times 10^{-5} \text{ S m}^{-1}$), and the volume changes of sulfur during cycling [77,78]. Thus, Li-S batteries have a poor rate performance and increased electronic resistance due to the embarrassments to rapidly obtain and release electrons from the current collector. In addition, the poor conductivity requires large amounts of carbon in the electrode to help the electron transfer for both S and Li_2S , which decrease the total energy density. In addition, the insulated sulfur and Li_2S could also become insoluble agglomerates over prolonged cycling, which decrease the active material utilization and capacity fading. On the other hand, based on the mass densities of sulfur (2.03 g cm^{-3}) and Li_2S (1.66 g cm^{-3}), the volume variation of sulfur cathode can be up to 80% when fully reducing sulfur to Li_2S [79]. This results in unexpected structure collapse of sulfur/carbon electrode upon cycling.

2.3 Introduction of Lithium-Selenium (Li-Se) Batteries

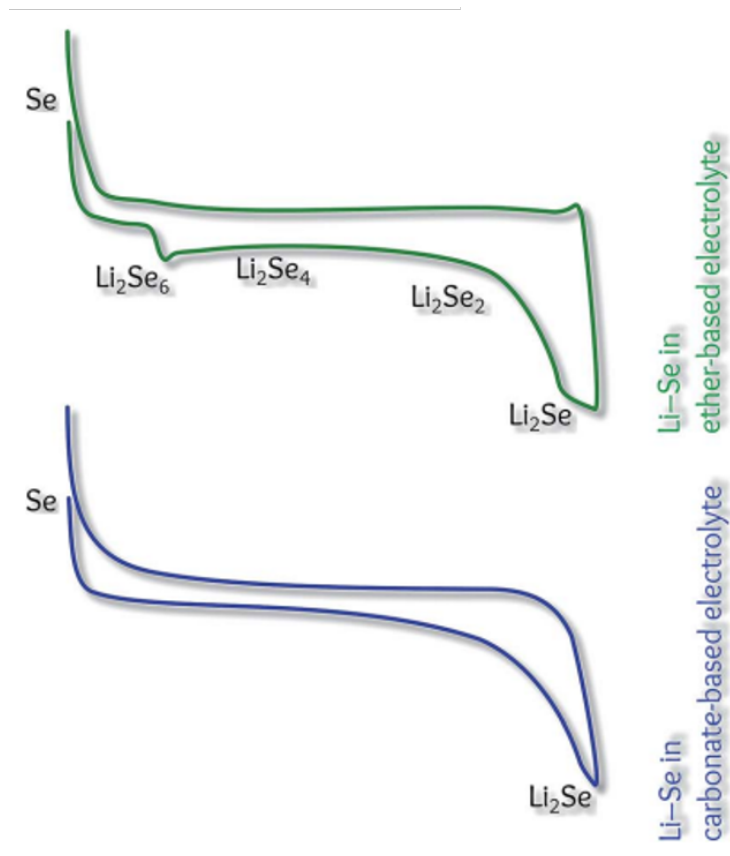


Figure 2.6. Schematic of the voltage profiles of a Li-Se battery in different electrolytes.

Selenium is a d-electron-containing element below sulfur in the family of chalcogenides, thus it has similar properties to sulfur. The history of lithium-selenium (Li-Se) batteries is almost as long as that of Li-S batteries. In 1970, the prospect of using Li-Se batteries in vehicles and medical devices was mentioned by Dr. Elton J. Cairns at Argonne National Laboratory. However, both electrochemical systems were facing issues for practical applications in the 20th century. With the massive demand of energy storage in the 21st century, Li-Se batteries are revisited by scientists and attract much attention as a new generation of rechargeable batteries. In comparison with sulfur, selenium is a less reactive and more controllable material in electrochem-

ical systems. Although Se has a lower specific capacity (675 mAh g^{-1}) than S (1672 mAh g^{-1}), it has a high volumetric capacity density of 3253 mAh cm^{-3} because of its high mass density of selenium (4.8 g cm^{-3}). In addition, the electrical conductivity of selenium ($1 \times 10^{-3} \text{ S m}^{-1}$) is much higher than that of sulfur ($5 \times 10^{-28} \text{ S m}^{-1}$). Selenium has different electrochemical behaviors in different electrolyte systems. **Figure 2.6** shows the schematic of typical electrochemical behaviors of a Li-Se battery in both ether-based electrolyte and carbonate-based electrolyte [80]. The contribution in this dissertation is mainly focused on the Li-Se battery with ether-based electrolyte.

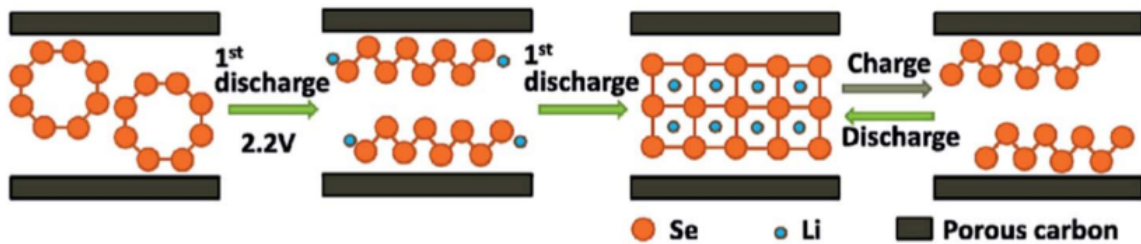
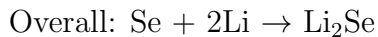
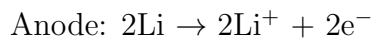


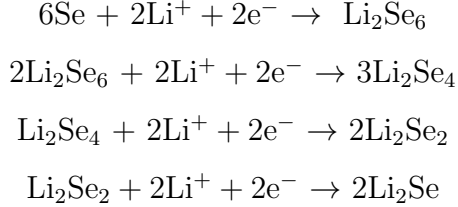
Figure 2.7. Illustration of lithiation and de-lithiation processes of Li-Se batteries.

As a result, Li-Se batteries have been studied as considerable candidates during the past few years. In Li-Se batteries, selenium undergoes a series of electrochemical redox reactions which are similar to the reactions of sulfur in ether-based electrolyte. However, the different part is that the Se_8 ring will form chain-format Se_8 initially in the 1st discharge process, followed by continuous discharging to Li_2Se , as shown in **Figure 2.7** [80]. In the conversion reactions, the Li_2Se will be charged to chain-format Se_8 instead of the original ring format. The overall reactions can be simply described by the equation below:



It should be paid attention that the selenium is not undergoing an exact one-step reaction in the carbonate-based electrolyte, but in the disappearance of the

forming polyselenides intermediates. The study here is in ether-based electrolyte, selenium starts to be discharged from a selenium ring with the formation of the polyselenides intermediates [19]. If considering the formation of polyselenides as liquid intermediates, the overall reaction can be described by the follow equation:



Selenium is a more stable and more controllable material with higher electronic conductivity than sulfur [81]. Therefore, it is technically possible to have a pure selenium electrode that can achieve a high volumetric capacity density. However, Li-Se batteries have some unsolved technical challenges that prevent their widespread applications. The first primary challenge is the polyselenides shuttle effect during charging. Due to the similarity to sulfur, Se also has a so-called shuttle effect, in which the soluble high-order polyselenides have redox reactions with lithium metal, resulting in low Coulombic efficiency and loss of selenium [82, 83]. In addition, like the other conversion-based materials, Li-Se batteries also have a challenge of the real contents of Se in the whole electrode system. Although it is possible to have a pure selenium cathode because of its high electronic conductivity and good controlled ability, carbon is still necessary to be provided as connections and electronic conductive intermediates. In addition, the volume expansions of selenium during redox reactions could need carbon as protective matrix. During the discharge, the Se lattice greatly expands to have enough space for the insertion of lithium atoms. Therefore, the ratio of selenium to carbon is also a key factor in Se cathodes. In many reported works, different auxiliary materials other than selenium, such as polymer binders, carbon black and carbon host materials, are necessarily needed, which although could decrease the contents of selenium, herein decrease the whole energy density [84, 85].

To overcome these challenges, many approachs have been utilized. The combinations of functional carbon hosts with selenium have been proven as one effective path

for the Se utilization and polyselenides shuttle alleviation. For instance, Luo et al. combined mesoporous carbon with selenium to form composite selenium electrodes, which showed amazing long cycle life and electrochemical performance in both Li-Se and Na-Se battery systems [86]. In addition, microporous carbon nanofibers can be applied to bind with selenium under particular treatments therefore alleviate the polyselenides from being dissolved, reported by Liu et al. in ref. [87]. Luo et al. captured selenium in an in-situ way by using perylene-3,4,9,10-tetracarboxylic dianhydride and selenium mixture, herein achieved good performance and high Coulombic efficiency in ref. [88].

With the purpose to further increase the volumetric energy and energy density of Li-Se batteries, developing a binder-free and free-standing selenium electrode becomes an efficient way to achieve the goal of having high selenium contents and high energy density. Due to the high difficulty of synthesizing advanced carbon hosts and employing Se, the Se content is usually below 50%, which is not a favor of achieving the possible high energy density. Much effort has been put to develop easy composite electrodes with high selenium contents. For instance, Wang et al. designed multi-walled carbon nanotube/selenium composite electrodes by using nano-scaled selenium via a solution-based processing strategy to achieve a selenium content of $\sim 60\%$ and high specific capacity in ref. [89]. Nitrogen-containing hierarchical porous carbon can also be used to combine with selenium to achieve composite electrodes with 56.2% selenium showing good cycling performance reported by Qu et al. in ref. [90]. Jiang et al. prepared carbon/selenium composite electrodes by applying 3-dimensional interconnected hierarchical porous carbon aerogels to capture selenium, which achieves a 56% selenium content and stable performance [91]. For a few works increasing the Se loading to over 60% in ether-based electrolytes, the Se cathode still shows continuous capacity fading and severe shuttle effect.

With the acknowledgements of similarities of selenium to sulfur and unsolved shuttle phenomenon in ether-based electrolyte. Much effort has also been put on using different approaches to increase Se area loadings or studying different electrolyte

systems, such as carbonate-based electrolytes. However, the Se has been found to have high compatibility but lower specific capacity in carbonate-based electrolytes, and high specific capacity but severe shuttle phenomenon in ether-based electrolyte. On the other hand, sulfur has high specific capacity in both two types of electrolytes, but bad compatibility in carbonate-based electrolyte. Therefore, other approaches other than developing advanced carbon matrix can be developing Se-based or Se/S hybrid compounds, which could be a prospect to solve the challenges of Li-Se batteries.

3. PHENYL SELENOSULFIDES AS CATHODE MATERIALS FOR RECHARGEABLE LITHIUM BATTERIES

3.1 Abstract

The Se-Se bond in an organo-diselenide (RSeSeR , R is an organic group) can break in a 2e^- reduction reaction, but it has limited capacity as a cathode material for rechargeable lithium-ion batteries. To increase its capacity, redox active species (e.g., sulfur) can be added in the middle of the selenium atoms. Herein, phenyl diselenide (PDSe, PhSeSePh) is mixed with sulfur to form two hybrid compounds with 1:1 and 1:2 molar ratios, which almost double and triple the capacity of PDSe, respectively. Theoretical calculations suggest that phenyl selenosulfide (PDSe-S, PhSe-S-SePh) and phenyl selenodisulfide (PDSe-S₂, PhSe-SS-SePh) can form via addition reactions, which is supported by mass spectrometry analysis. The hybrid materials exhibit three highly reversible redox plateaus and enhanced cycling stability due to the reduced solubility of the discharge products. PDSe-S and PDSe-S₂ show initial capacities of 252 and 330 mAh g^{-1} , respectively, followed by stable cycling performance with a capacity retention of $>73\%$ after 200 cycles at $C/5$ rate. In addition, they show steady rate capabilities. This study reports a novel strategy to increase the electrochemical performance of organo-diselenide by addition of sulfur.

3.2 Introduction

Lithium-ion (Li-ion) batteries have been widely used in portable electronics and are being adopted in all electric vehicles due to their high energy densities compared to other battery chemistries [92]. In Li-ion batteries, transition metal oxides are used

as the cathode materials which have reached their capacity limits. The growing demand for high energy batteries has inspired great interest in exploring high-capacity cathode materials [23]. In this regard, lithium-sulfur (Li-S) and lithium-selenium (Li-Se) batteries are promising because elemental sulfur and selenium have high theoretical specific capacities of 1672 mAh g^{-1} and 675 mAh g^{-1} , respectively. Each sulfur or selenium atom can take up to 2Li^+ and 2e^- when electrochemically reduced in lithium batteries. Conversion reactions are predominant in Li-S and Li-Se batteries, which are different from the ion intercalation reactions occurred in transition metal oxides. Because of the insulating nature of sulfur ($5 \times 10^{-28} \text{ S m}^{-1}$) and its non-conductive discharged products, high contents of carbon are usually needed in electrodes. In contrast, selenium below sulfur in the periodic table has a much higher electronic conductivity ($1 \times 10^{-3} \text{ S m}^{-1}$) and it also has a high volumetric capacity density of 3253 mAh cm^{-3} because of its high mass density (4.8 g cm^{-3}).

Both Li-S and Li-Se battery systems are facing some technical challenges that prevent them from the widespread application. In Li-S batteries, one primary challenge is the so-called shuttle effect, in which high-order soluble polysulfides species ($\text{Li}_2\text{S}_{6-8}$) are formed and then transport to lithium metal anode during the charging process, which results in low Coulombic efficiency, continuous loss of sulfur, and insoluble agglomerates over prolonged cycling [93]. Similarly, Se cathode also has the issue of shuttle effect. To reduce shuttle, several strategies have been developed, such as use of microporous carbon hosts, fabrication of core-shell structure, and adoption of interlayer cell configuration. Recently, our group has demonstrated that organopolysulfides (RS_nR , $n = 3-6$, R is an organic group) are a class of high-capacity cathode materials for rechargeable lithium batteries [44, 94–97]. The unique character of linear organopolysulfides is that short sulfur chains are chemically capped by R groups, therefore high-order polysulfides are significantly reduced initially and upon cycling. The obvious benefit is their low dependence on liquid electrolyte, in another word, the electrolyte/active material ratio is low (e.g., $3 \mu\text{L mg}^{-1}$) which can enable high energy

densities of batteries [98]. In addition, they have tunable electrochemical properties (e.g., voltage plateau) and performance (e.g., cycling stability) [44].

In this contribution, we select phenyl diselenide (PDSe) as a model compound which has a low specific capacity and poor cycling performance because of its solubility in liquid electrolyte. One or two molar equivalent of sulfur as active redox species is chemically added to increase its capacity and reduce the solubility of discharged products. Interesting electrochemical phenomena are revealed experimentally and computationally, and enhanced cycling performance is achieved.

3.3 Experimental

3.3.1 Materials and Instruments

All materials were used as received and listed in table 3.1. All instruments used were listed in table 3.2.

Table 3.1. Materials

Chemical Name	Purity	Provider
Lithium bis(trifluoromethanesulfonimide) (LiTFSI, $\text{LiN}(\text{CF}_3\text{SO}_2)_2$)	99%	Acros Organics
Lithium nitrate (LiNO_3)	99.999%	Acros Organics
1,2-dimethoxyethane (DME)	99.5%	Sigma Aldrich
1,3-dioxolane (DOL)	99.8%	Sigma Aldrich
Phenyl diselenide (PDSe, $\text{C}_{12}\text{H}_{10}\text{Se}_2$)	99%	Acros Organics
Sulfur (S)	99.5%	Alfa Aesar
Carbon disulfide (CS_2)	Certified ACS	Fishers Scientific

Table 3.2. Instruments

Instrument	Provider
Battery cycler	Arbin BT2000
VSP potentiostat	BioLogic
Differential scanning calorimetry (DSC)	TA 2000 instruments SDT Q600 analyzer
Vacuum Oven	Isotemp 281A
Mass spectrometry	Thermo MAT-95XL magnetic sector instrument
Glove box	MBraun
Scanning electron microscopy (SEM)	JEOL JSM-7800F
X-ray diffraction (XRD)	Bruker D8 Discover XRD Instrument

3.3.2 Preparation of electrolyte and PDSe/S hybrid compounds

The electrolyte is composed of 1.0 M LiTFSI and 0.1 M LiNO₃ in a mixture solvent of DME and DOL (1:1 v/v). The PDSe solution was prepared by dissolving PDSe in CS₂ to form 0.5 M solution. Elemental sulfur solution was prepared by adding sulfur in CS₂ to form 0.5 M solution as well. To prepare hybrid compounds, PDSe and sulfur solutions with appropriate amounts of PDSe and S (PDSe:S = 1:1 and 1:2 molar ratios) were mixed in CS₂ to render 0.5 M PDSe-S and PDSe-S₂ solutions, respectively. The synthesized materials are stable in CS₂, which remains clear for days. Chloroform can also be used for making these hybrid compounds.

3.3.3 Preparation of PDSe, pristine S and PDSe/S hybrid electrodes

Commercial binder-free carbon nanotube paper called buckypaper (NanoTechLabs Composites, Inc) was used as the current collector in this study. The carbon paper was cut into 0.97 cm^2 discs ($D = 11 \text{ mm}$, about 1.9 mg each) and dried at 100°C for 24 hours in a vacuum oven before use. $20 \mu\text{L}$ prepared PDSe solution was added into dried carbon paper in a petri dish. Then the carbon paper electrode was dried in a vacuum oven at room temperature for 12 hours for the control experiment. The elemental sulfur electrode and hybrids electrodes of DPSe-S and DPSe-S₂ were prepared by following the same procedure.

3.3.4 Cell fabrication and electrochemical evaluation

CR2032 Coin cells were used and cells were fabricated in an Ar-filled glove box. First, $15 \mu\text{L}$ electrolyte was added into the prepared carbon paper electrode. The mass of PDSe on carbon paper is 3.1 mg corresponding to a weight percent of 62%. The masses of PDSe-S and PDSe-S₂ on carbon paper are 3.4 mg and 3.8 mg , corresponding to weight percentages of 64% and 67%, respectively. Then a Celgard 2400 separator was placed on the top of the electrode followed by adding $15 \mu\text{L}$ electrolyte on the separator. Finally, a piece of lithium metal and nickel foam as a spacer was placed on the separator. The cell was crimped and taken out of the glove box for electrochemical evaluation. The mass loadings used in this study are optimized. Higher mass loadings would require thicker carbon paper current collectors.

Cells were galvanostatically cycled on an Arbin BT2000 battery cycler at different C rates ($1\text{C} = 172 \text{ mA g}^{-1}$ for PDSe, 312 mA g^{-1} for PDSe-S and 428 mA g^{-1} for PDSe-S₂, based on the mass of material in the cells) and in voltage ranges (C/10 and C/5: 1.8-2.8 V, C/2: 1.75-2.8 V, 1C: 1.7-2.8 V, 2C: 1.65-2.8 V). Cyclic voltammetry (CV) was performed on a BioLogic VSP potentiostat. The potential was swept from open circuit voltage to 1.8 V and then swept back to 2.8 V at a scanning rate of 0.02 mV s^{-1} .

3.3.5 Characterizations

Differential scanning calorimetry (DSC) was performed on a TA 2000 instruments SDT Q600 analyzer. The PDSe sample was prepared from the solution-drying process by using the PDSe solution in CS_2 . The PDSe solution was added in a small glass vial and then dried under room temperature in a vacuum oven. Once the solvent was removed by evaporation, the powder was collected and sealed in the vial. The PDSe-S and PDSe-S₂ hybrid samples were prepared by following the same solution-drying process for test. All the samples are between 5-7 mg and tested under Air flow at 50 mL min⁻¹ while heating from 25 to 350 °C with temperature ramping rate of 5 °C min⁻¹.

Mass spectrometry (MS) were analyzed for samples by electron ionization mass spectrometry using a Thermo MAT-95XL magnetic sector instrument. Samples were diluted approximately 1 mg mL⁻¹ in CS_2 ; 2 μL of this solution was placed in an aluminum crucible for MS. The crucible was placed in the source (1.8×10^{-5} mbar pressure) and heated at a temperature sufficient to volatilize the sample and generate ions (manually ramped between 75 °C and 225 °C). The mass scale was internally calibrated with ions from perfluorokerosene vapor that was leaked into the source throughout the experiment.

The morphological characterization of PDSe-S and PDSe-S₂ hybrids cathodes was conducted with a JEOL JSM-7800F field emission scanning electron microscopy (SEM). The elemental mapping was performed with energy-dispersive X-ray spectroscopy (EDS) attached to the SEM at 10 kV to confirm the presence of selenium and sulfur in particles of electrodes.

The X-ray diffraction (XRD) data of PDSe, elemental sulfur, and PDSe-S hybrids materials were collected on a Bruker D8 Discover XRD Instrument equipped with Cu K radiation. The scanning rate was 1.2° min⁻¹, for 2θ between 10° and 60°. The PDSe sample from the solution-drying process was added on a glass and protected

with Kapton tape. For comparison, elemental sulfur (0.5 M) in CS₂ and PDSe-S hybrids were also prepared for XRD by following the same procedure.

3.3.6 Computations

In this work, first-principles calculations based on the density functional theory (DFT) were performed using SPARTAN software package (Wave function, Irvine, CA) to determine the equilibrium geometry and energetics of various molecules. The M06-2X exchange-correlation functional and the 6-31G* basis set were used. To simulate the effect of the solvent, a polarizable continuum model (PCM) was used, and the dielectric constant was set to that of DME that was used as the electrolyte in this study (the dielectric constant of DOL is similar to that of DME).

The reaction voltage is determined by calculating the energy difference between the final product and the initial reactant. Lithium metal is used as the anode and the voltage is reported in reference to metallic lithium electrode. Since SPARTAN is a molecular modeling software, the energy of lithium metal is calculated using the following thermodynamic path:



Following this path, the lithium ion energy in the solution was calculated first, and converted to the energy of metallic lithium by adding experimental lithium ion solvation, ionization, and cohesive energy. It should be noted that the calculation of lithium ion energy in the solution subject to significant errors because of the limitation of current solvation models. Explicit calculation is also difficult since the electrolyte solution contains a mixture of different organic solvents and lithium salts. For these reasons, the lithium ion energy in the solution was fitted to the first voltage plateau observed experimentally, then the same energy was used to predict the voltage of the second and third voltage plateaus.

3.4 Results and Discussion

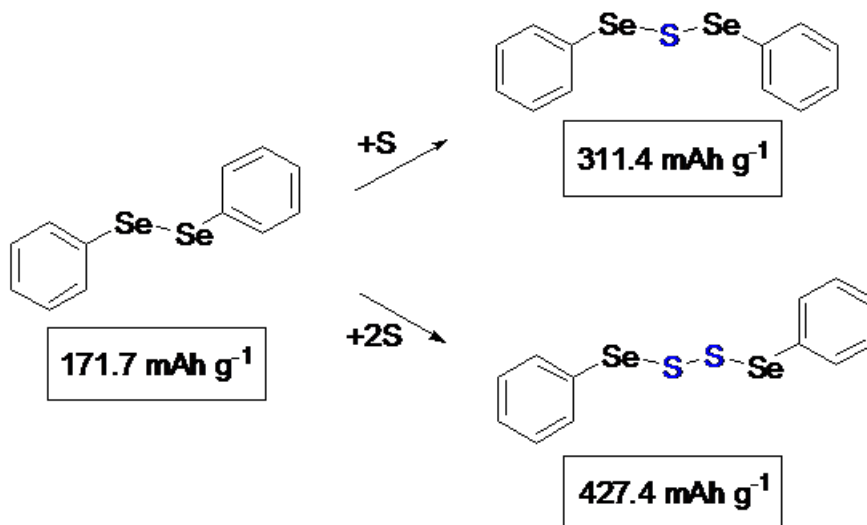


Figure 3.1. Schematic of addition reactions of phenyl diselenide (PDSe) with one sulfur atom to form phenyl selenosulfide (PDSe-S) and phenyl selenodisulfide (PDSe-S₂). The values shown in the boxes are their theoretical specific capacities.

Phenyl diselenide (PDSe) is one of the organic materials that can be used as cathode materials in rechargeable lithium batteries. The PDSe has two selenium atoms bonded each other in the middle with two phenyl rings as organic groups on both sides. When the PDSe is used as cathode materials in the batteries, 2 Li⁺ will be obtained for each molecule of PDSe to open the Se-Se bond in the discharge process. In the conversion process, the discharge products lose Li⁺ cations and form back to PDSe reversibly. PDSe has a low theoretical capacity of 171.7 mAh g⁻¹ based on the 2e⁻ reduction reaction. It is soluble in ethereal electrolyte, which makes it unsuitable to be used as a cathode material in rechargeable lithium batteries. Our first-principles calculation based on the density functional theory (DFT) suggests that the Se-Se bond in PDSe has an energy of 1.7 eV, which is lower than the S-S bond energy of 2.01 eV in phenyl disulfide (PhSSPh). First-principles calculation is first used as a base method to study the hypothesis that adding sulfur atoms between the

selenium atoms. In our previous study, PhS-S-SPh can be formed using PhSSPh and elemental sulfur as starting materials, where the S-S bond breaks and an additional sulfur atom can be added. In addition, more sulfur atoms can be added in PhSSPh to form PhS-S₂-SPh, or even higher-order polysulfide chains (PhS-S_x-SPh, x=5-8). However, high-order polysulfide chains between phenyl rings can become unstable in the solution, which results in decomposition and break of the multiple S-S bonds. The instability and weaken bonds of the high-order chains make it not being ideal synthesized materials. Therefore, we believe PhSe-S_x-SePh could also be formed using a similar synthesis method. PhSe-S-SePh (designated as PDSe-S) and PhSe-SS-SePh (designated as PDSe-S₂) are selected as the target compounds, so that the results could be compared with phenyl trisulfide (PhS₃Ph) and phenyl tetrasulfide (PhS₄Ph) we reported previously [44,96]. In addition, these compositions may avoid the formation of long-chain lithium polysulfides upon cycling, hence avert the shuttle effect of sulfur. By having one or two sulfur atoms in the chemical structure, PDSe-S and PDSe-S₂ have theoretical capacities of 311.4 mAh g⁻¹ and 427.4 mAh g⁻¹, respectively, as shown in **Figure 3.1**. The study of these hybrid compounds is helpful for understanding the electrochemical behavior of organic materials containing Se-S bonds in lithium batteries.

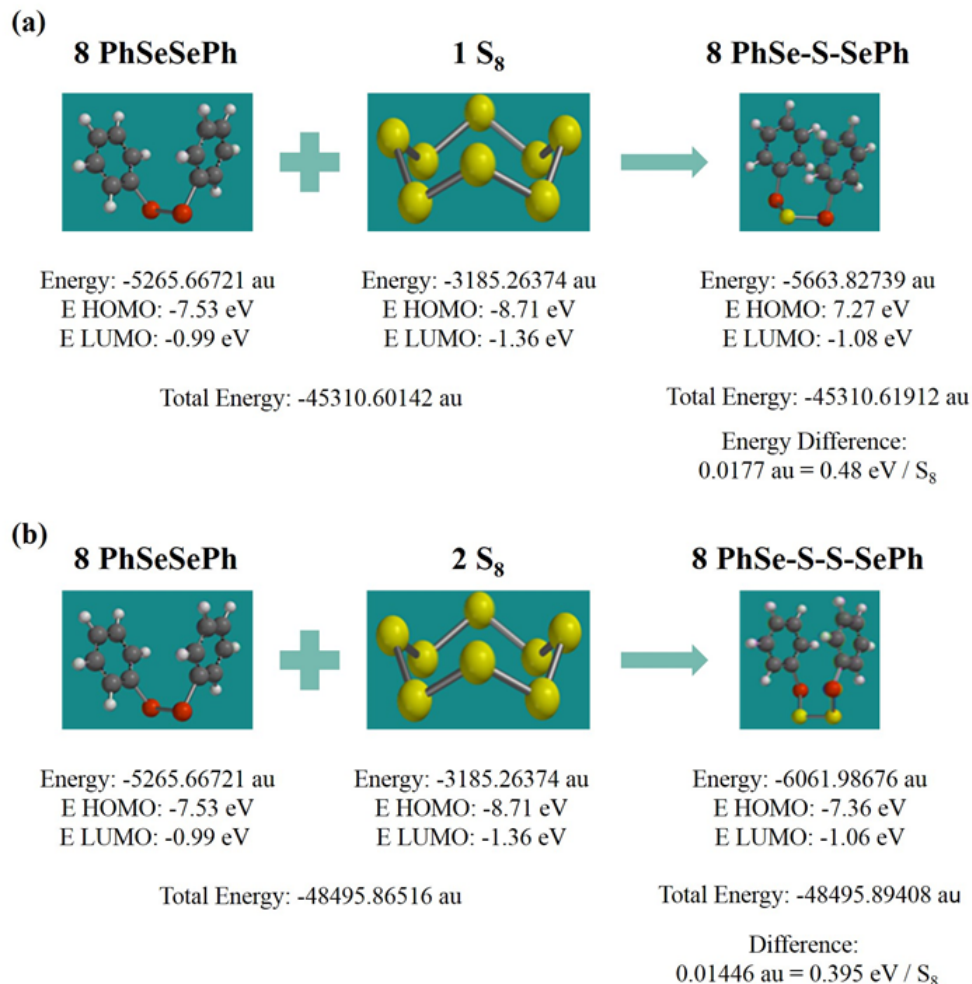


Figure 3.2. The reaction and energy difference of forming (a) PDSe-S and (b) PDSe-S₂.

Elemental sulfur (S₈) is in the form of a crystalline solid that is composed of octa-sulfur ring at room temperature. The PDSe can be dissolved in carbon disulfide to form a solution. When elemental sulfur is dissolved in carbon disulfide (CS₂) with PDSe, the PhSe radical may form because of the low Se-Se bond energy, for which the formed PhSe radical could attack and result in scission of the sulfur ring. To determine the most energetically favorable reactions, DFT computational screening of all possible routes is performed. As presented in **Figure 3.2**, reaction 1 gives the biggest energy lowering of 0.48 eV/S₈ when one equivalent of sulfur is added.

When two equivalents of sulfur are added, reaction **2** gives an energy lowering of 0.395 eV/S₈. It is also possible to have another reaction **3** as shown below. The reaction **3** is 0.0027 eV/S₈ lower in energy as compared to reaction **2**. Since the reaction has stoichiometric amount of sulfur atoms to PhSe radicals, the reaction **3** leads a possible route to have a mixture products solution. But overall the product can be regarded as the PhSe-SS-SePh. This energy difference is extremely small, and we expect that PhSe-SS-SePh is the dominated product, although other species such as PhSe-S₄-SePh and PhSe-S-SePh may be formed as a result of reaction **3**.

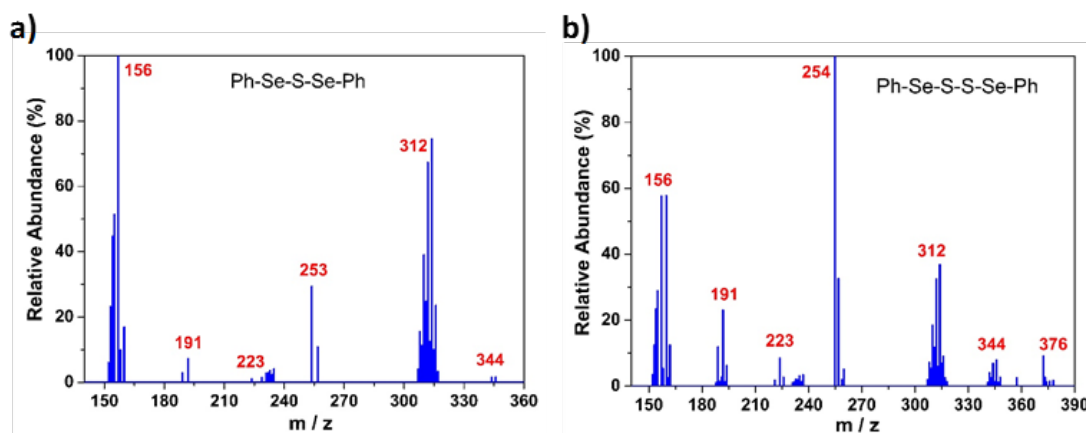
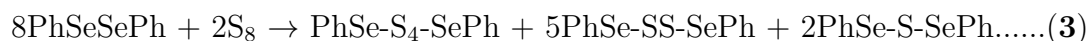
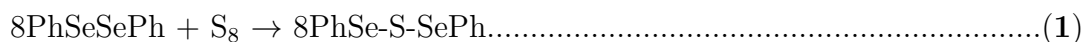


Figure 3.3. Mass spectra of (a) PDSe-S and (b) PDSe-S₂.

In order to verify the synthesized hybrids, mass spectrometry (MS) was performed. **Figure 3.3a** and **b** show the mass spectra of PDSe-S and PDSe-S₂ samples, respectively. The mass spectrum in **Figure 3.3a** has the parent ion peak at a m/z of 344 corresponding to the molar mass for PDSe-S. Other smaller fragmentation peaks corresponding to those of PhSeSePh (phenyl diselenide, m/z = 312), PhSe· (phenyl selenium radical, m/z = 156), ·Se-S-Se· (diselenosulfide radical, m/z = 191), and

PhSeS₃· (phenyl selenotrisulfide radical, $m/z = 253$). The deviations between some m/z values and molecular weights of the fragments could be due to the isotopes of carbon, selenium, and sulfur [99]. The mass spectrum in **Figure 3.3b** has the parent ion peak at a m/z of 376 corresponding to the molar mass for PDSe-S₂. The other smaller fragmentation peaks include those of PDSe-S, PhSeSePh, PhSe·, ·SeSSe·, and PhSeS₃·. The $m/z = 223$ corresponds to ·Se-SS-Se· (diselenodisulfide radical). In both spectra, PhSeS₃· is seen and no obvious peaks can be seen at m/z higher than 400, indicating a negligible amount of phenyl selenotetrasulfide or other selenopolysulfides. The MS results confirm that PDSe-S and PDSe-S₂ are formed by this synthesis method, which is consistent with the calculation results. The absence of phenyl selenotetrasulfide predicted by reaction **3** could be due to its low molar concentration. Another possibility is that the selenotetrasulfide compound and the compound with longer than 4-polysulfides chains could not be in stable formations in the solutions. The possibly formed selenotetrasulfide compound easily break into short-chains compounds. Either of the two reasons suggests that the selenotetrasulfide is not a favorable formation. On the other hand, PDSe-S and PDSe-S₂ are confirmed as the main products. However, the resultant samples may contain other impurities such as unreacted PDSe and PDSe-S₃. DPSe-S₃ may be in the form of PhSeS₃· and PhSe· radicals since no peaks of PhSe-S₃-SePh are seen in the MS spectra.

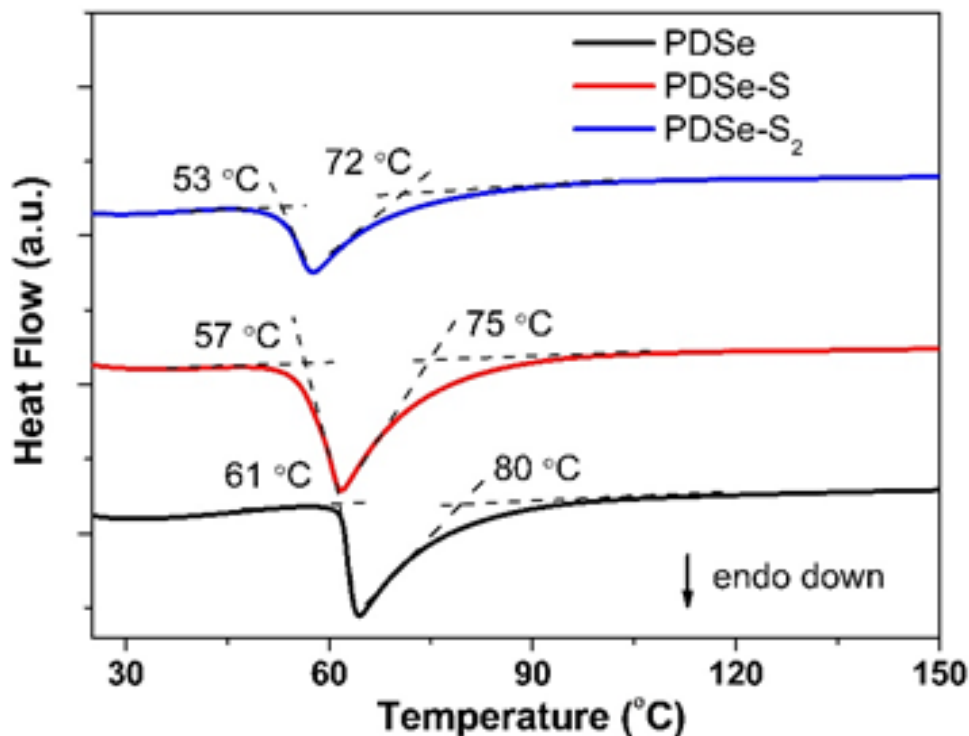


Figure 3.4. DSC plots of DPSe, DPSe-S, and DPSe-S₂.

To further characterize these hybrid compounds, differential scanning calorimetry (DSC) and X-ray diffraction (XRD) were performed on powder samples. The DSC spectra in **Figure 3.4** show that PDSe exhibits a narrow endothermic peak at 61-80 °C. The endothermic peak is attributed to the melting point. PDSe-S exhibits an endothermic peak at 57-75 °C and PDSe-S₂ exhibits an endothermic peak at 53-72 °C. The melting point of a material can be considered as the inflection going down to endothermal. The melting points of these compounds are in the order of PDSe (61 °C) > PDSe-S (57 °C) > PDSe-S₂ (53 °C). The additional sulfur atoms in PDSe lowers the melting point, which is same as the result of PhSSPh/PhS-S-SPh ($T_{m, \text{PhS-S-SPh}} < T_{m, \text{PhSSPh}}$) we reported previously [96]. The long Se-S-Se and Se-SS-Se chains result in more disorder in the structure, therefore PDSe-S and PDSe-S₂ are easier to melt. On the other hand, it has to be noted that elemental sulfur has a melting point of

115 °C, which is much higher than those of these synthesized compounds, therefore elemental sulfur is absent from the synthesized compounds.

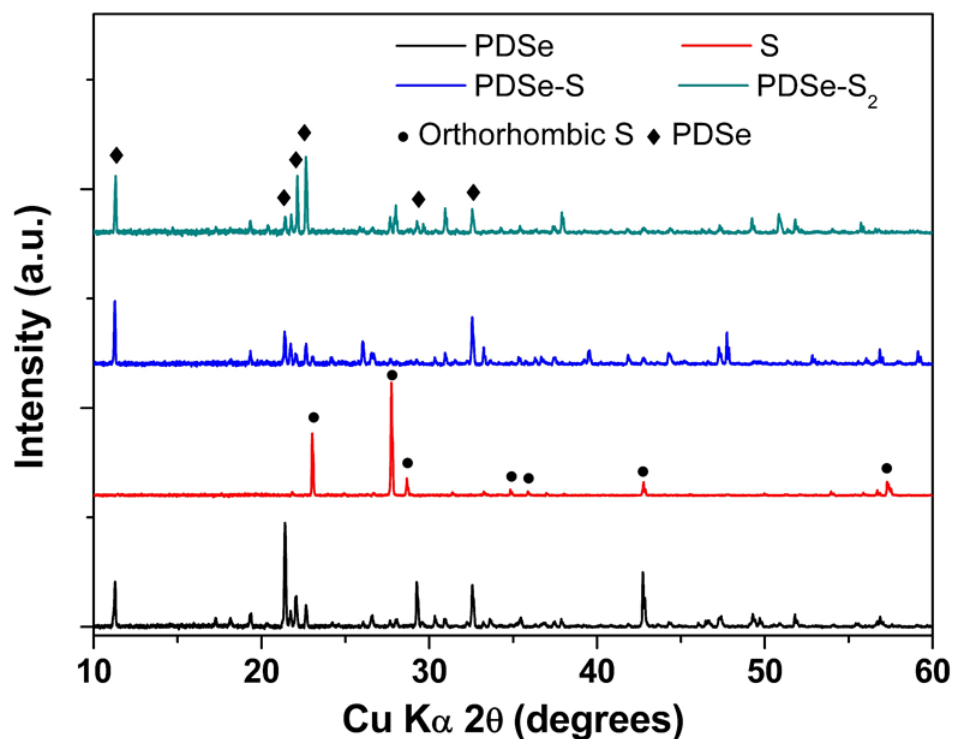


Figure 3.5. XRD patterns of PDSe, pristine sulfur, PDSe-S and PDSe-S₂.

In the XRD patterns shown in **Figure 3.5**, PDSe shows multiple crystalline peaks. The crystalline peaks are mainly from the crystallization of the phenyl rings. The sulfur has totally different crystalline peaks as compared to PDSe. The detected sulfur peaks show that the sulfur is in orthorhombic structure from the solution drying procedure. Major peaks between 20-30° and at 43° are matched by the database files. The formed PDSe-S and PDSe-S₂ show similar crystalline peaks as those of PDSe, but almost no sulfur peaks. This is because that the phenyl rings have big effects on the XRD detections. The disappearance of sulfur peaks suggests the addition reactions of sulfur into the PDSe reactants. Very rare intensity of the sulfur peaks could be due to the excess non-reacted sulfur under XRD detection. The DSC and

XRD results indicate elemental sulfur is mostly converted and added in PDSe to form PDSe-S and PDSe-S₂ hybrid compounds.

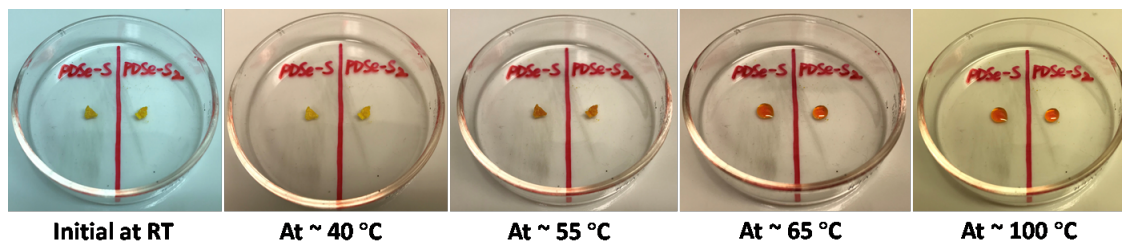


Figure 3.6. Synthesized compounds stability for PDSe-S and PDSe-S₂ at variable temperatures.

The synthesized compounds (PDSe-S and PDSe-S₂) are also tested for stability at variable temperature conditions, as shown in **Figure 3.6**. The compounds are initially synthesized and left for 1 month at room temperature (RT), PDSe-S and PDSe-S₂ show no change or decomposition for long time idle. At room temperature, the synthesized compounds can be stable and stored over a long time period. The sulfur is in light yellow color and the phenyl diselenide is in orange color. Both PDSe-S and PDSe-S₂ have a slightly dark yellow color, instead of the colors of pure sulfur or phenyl diselenide. Then the compounds are heated to approximately 40 °C on a hot plate in the fume hood, and the compounds have no morphological change or decomposition after heating for 15 minutes. The temperature is further increased to approximately 55 °C, it can be seen that the color of the compounds is becoming much darker, which is close to orange color. Both the compounds are in soft solid formation, which can be considered in the half-melted phase. It has to be noted that 55 °C is shown on the hot plate, but the actual temperature heating the materials could be 1 or 2 degrees less due to the transferred heat loss. When further increasing the temperature to 65 °C, the compounds have melted in orange liquid phase. Since 65 °C is far beyond the melting points, the compounds are no longer be able to stay in the solid phase. After the temperature being increased to 100 °C, the compounds

maintain stable liquid states without any observed decomposition. Although the phase of both PDSe-S and PDSe-S₂ transfers from solid to liquid, the synthesized compounds show good molecular stability at high temperature condition.

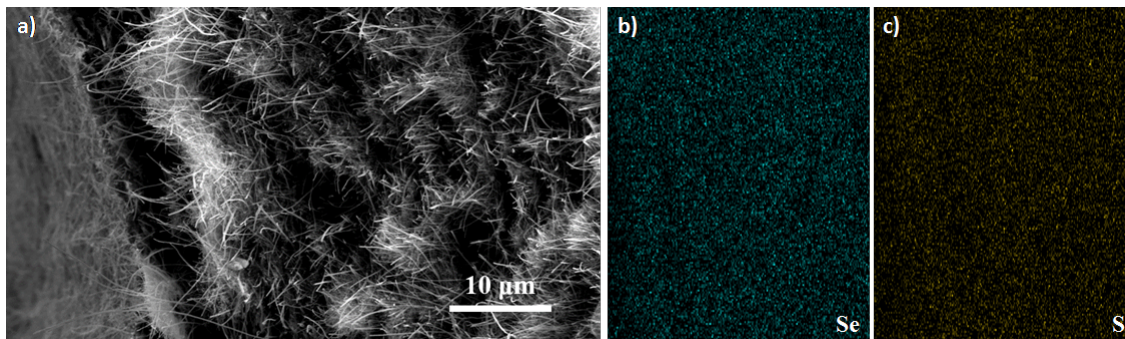


Figure 3.7. (a) cross-section SEM image and EDS showing (b) selenium and (c) sulfur mapping of the PDSe-S₂ electrode.

These compounds are formed in CS₂ solvent and dispersed in the carbon paper current collector followed by solvent evaporation. Scanning electron microscopy (SEM) and electron dispersive spectroscopy (EDS) were performed to examine the morphology and elemental distribution in the prepared electrodes, as shown in **Figure 3.7a**, **b** and **c**, respectively. The cross-section SEM image in **Figure 3.7a** shows carbon nanotubes and fibers of the carbon paper. The carbon paper has layered structure with enough spaces and pores as storage for materials. The EDS in **Figure 3.7b** and **c** reveals the uniform distribution of sulfur and selenium elements in the electrode. The synthesized compound is in small particles and stored between the carbon layers. The uniform distribution of selenium mapping suggests the uniform storage of materials. **Figure 3.8** shows additional SEM and EDS images of the surface/cross section of electrodes. The pristine carbon paper consists of carbon nanofibers and carbon nanotubes. The interwoven structures provide the porosities for holding active materials. After adding active material (e.g. PDSe-S), the materials are stored in the porous structure covered by carbon nanofibers and nanotubes. In the high magnified SEM image **Figure 3.8c**, the PDSe-S is uniformly distributed in the carbon paper

spaces. The EDS scan in **Figure 3.8e-h** confirms this uniform distribution. In the SEM image of the cross-section, it can be seen that the carbon paper is in layered structure, and the active materials are well held in the spaces. The electrode prepared by this method promises reliable evaluation of these materials in rechargeable lithium batteries.

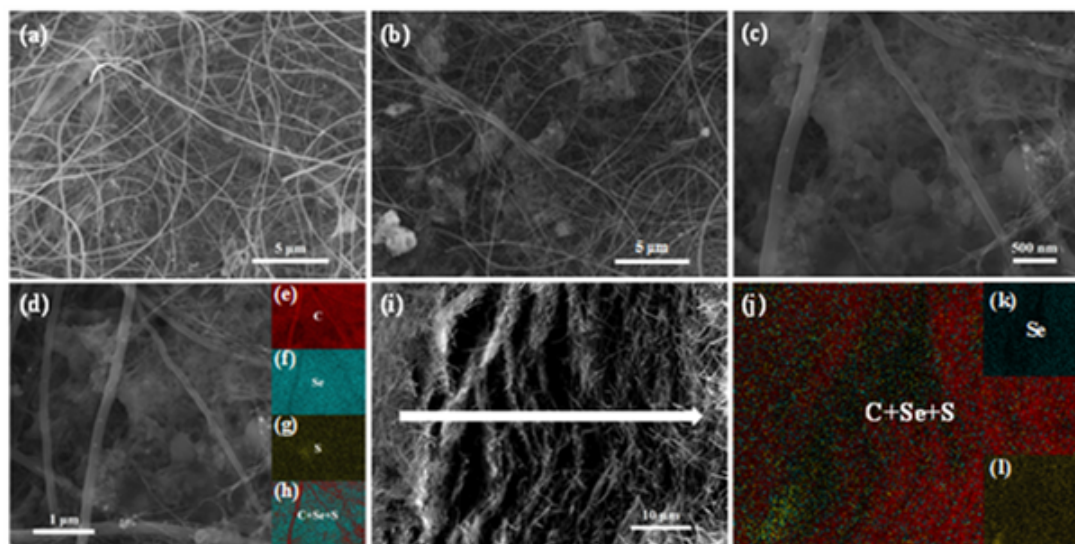


Figure 3.8. SEM image of (a) the pristine carbon paper, (b) moderate magnification, (c) high magnification of PDSe-S electrode, (d-h) EDS scan for carbon, selenium, sulfur and overlapping, (i) SEM image of cross-section of PDSe-S electrode, (j-l) EDS scan on cross-section for overlapping, selenium and sulfur.

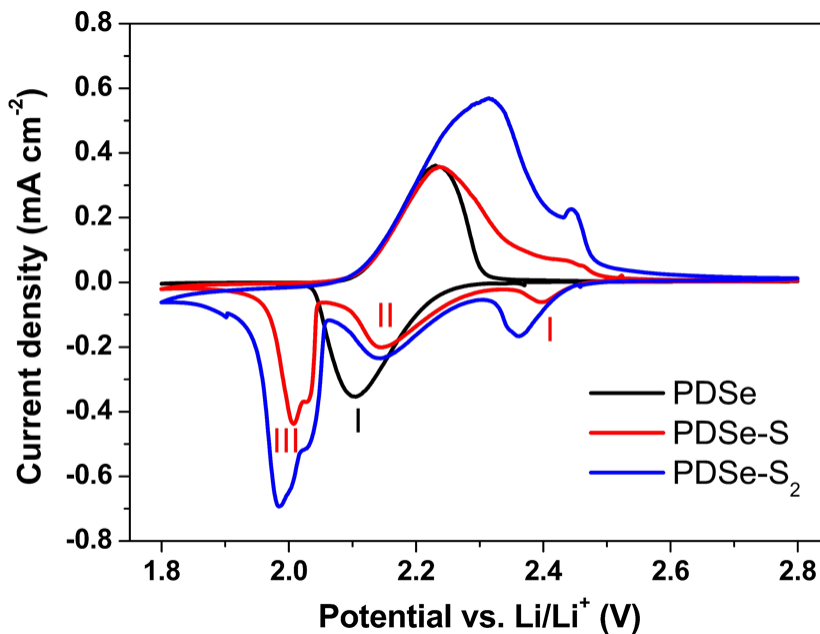


Figure 3.9. Cyclic voltammogram of PDSe, PDSe-S, and PDSe-S₂.

The electrochemical behavior of PDSe-S and PDSe-S₂ was evaluated by cyclic voltammetry (CV) in lithium half cells, as shown in **Figure 3.9**. In the cathodic scan from open circuit voltage (OCV) to 1.8 V, PDSe only shows one reduction peak (black I) at 2.1 V due to the formation of PhSeLi. In the following anodic scan, only the oxidation peak at 2.25 V is seen. In contrast, PDSe-S shows three reduction peaks in the cathodic scans. The first small reduction peak of PDSe-S (red I) is shown at 2.4 V, the second reduction peak (red II) occurs at 2.15 V, and the third reduction peak (red III) is shown at 2.0 V. Obviously, the peak III is an overlap of two peaks. PDSe-S₂ shows three similar reduction peaks, but different peak areas because of different sulfur content. Both PDSe-S and PDSe-S₂ show two overlapped anodic peaks. The small peak at 2.45 V should be related to the final formation of PDSe-S and PDSe-S₂. More sulfur atoms lead to more obvious peaks.

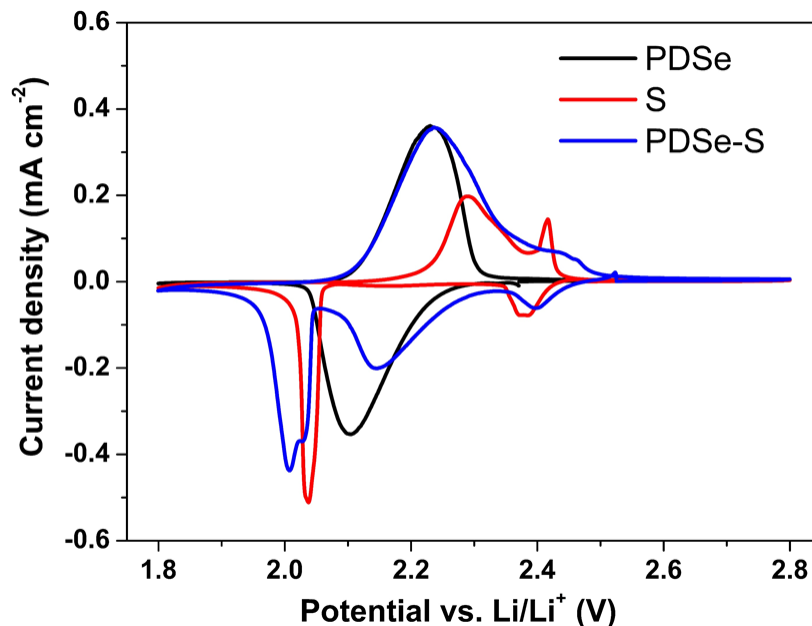


Figure 3.10. Cyclic voltammogram of PDSe, S, and PDSe-S.

To better investigate the redox peaks difference, **Figure 3.10** shows the CV plot by comparing PDSe-S with PDSe and elemental sulfur. Equivalent sulfur mass with the sulfur amount in PDSe-S are plotted in this CV comparison. This comparison provides a direct observation between synthesized compound and elemental sulfur. The CV of pure sulfur cathode has two reduction peaks corresponding to the formation from sulfur to low-order polysulfides and low-order polysulfides to Li_2S . The two oxidation peaks in the conversion reactions are corresponding to the formation from Li_2S to high-order polysulfides and high-order polysulfides to sulfur. It can be observed that the three reduction peaks of PDSe-S and PDSe-S₂ are not simple addition of peaks of PDSe and sulfur, but highly integrated. As a comparison sample, the first reduction peak of the PDSe-S is clearly from the sulfur reaction. The second peak is clearly from the PDSe reaction but also slightly shifted. The CV suggests that the first two reaction steps are related to the sulfur atom and the selenium atom. The area of the 2nd reduction peak of the PDSe-S is only about half of the PDSe, which suggests the related PhSe radical is only about 50% of the total PDSe. The last

reduction peak is clearly formed by two peaks from sulfur and PDSe. The oxidation peak of PDSe-S is highly integrated by PDSe and S but shows no 2nd peak of the sulfur reactions. This suggests the sulfur atoms are converted back to form the Se-S bonds instead of forming pure sulfur.

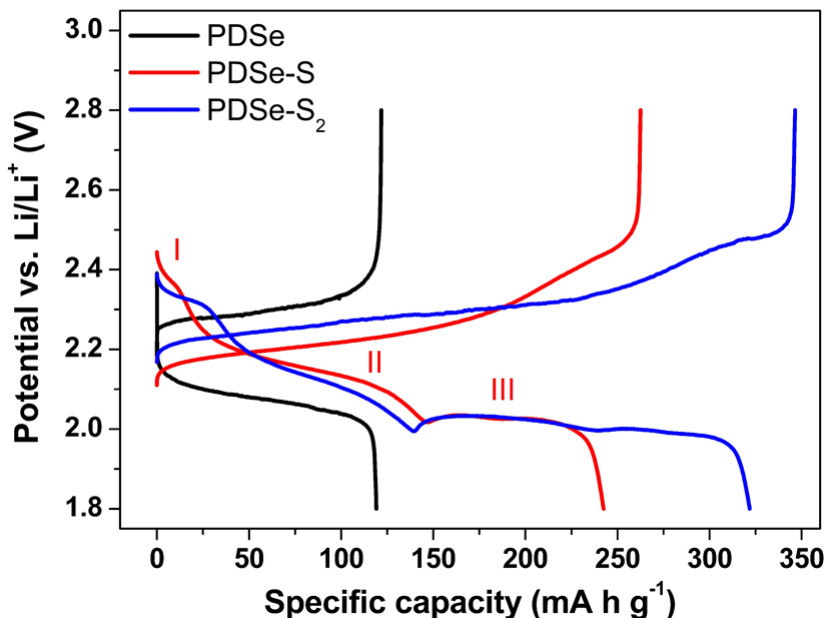


Figure 3.11. Voltage profile of PDSe, PDSe-S, and PDSe-S₂.

Figure 3.11 shows the typical voltage profiles of these compounds. PDSe only shows one voltage plateau at 2.0-2.15 V in the discharge and one voltage plateau at 2.25-2.35 V in the charge. Both PDSe-S and PDSe-S₂ have three visible plateaus in the discharge and two plateaus in the charge. All of these resemble the peaks in CV. In the discharge of PDSe-S, plateau I is very short starting at 2.4 V and ending at 2.32 V. Plateau II is mainly between 2.2-2.05 V, corresponding to the formation of discharge intermediates. Plateau III is under 2.05 V corresponding to the formation of end discharge products. The PDSe-S₂ also shows similar voltage profile during discharge, but with a much longer plateau below 2.05 V. The charge voltage profile consists of a long low-voltage plateau followed by a short high-voltage plateau. The

charge plateaus of PDSe-S and PDSe-S₂ are much lower than that of PDSe. Because the onset anodic potentials of these three cells shown in **Figure 3.9** are almost the same, the differences in the charge potential should be due to ohmic overpotential and kinetic effect.

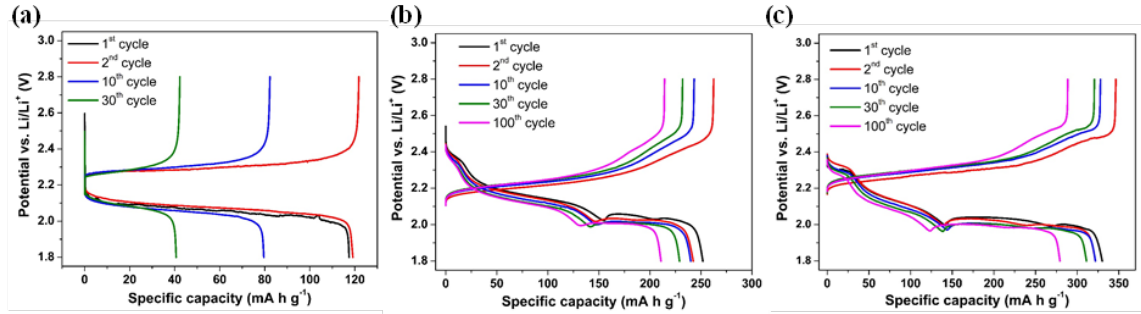


Figure 3.12. Voltage-capacity profile of (a) PDSe, (b) PDSe-S, and (c) PDSe-S₂ at C/5 rate in different cycles.

Selected voltage profile of PDSe, PDSe-S and PDSe-S₂ over 100 cycles are shown in **Figure 3.12**. PDSe only has one discharge plateau and one charge plateau indicating the one-step reaction during redox reactions. Both PDSe-S and PDSe-S₂ have three major discharge plateaus over 100 cycles, which consisted with the CV profiles and the reaction hypothesis. Their charge steps include a long low-voltage charge plateau and a short high-voltage plateau. The overpotential between the discharge plateaus and charge plateaus have no obvious changes, which indicates the well reversibility and promising charge and mass diffusions during prolonged cycling.

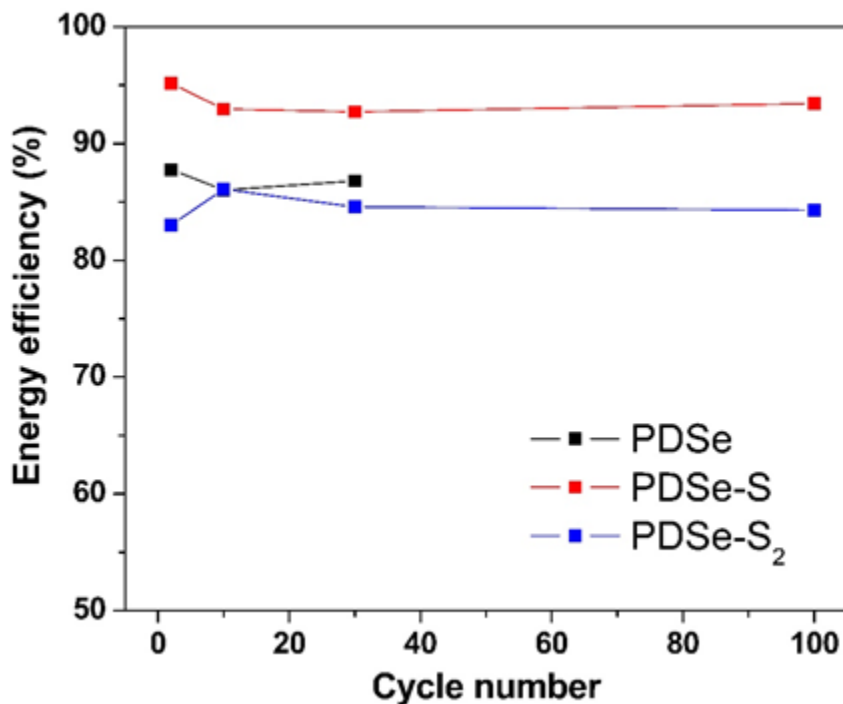


Figure 3.13. Calculated energy efficiencies of PDSe, PDSe-S, and PDSe-S₂.

The energy efficiencies are calculated from the charge/discharge profiles, which are in the order of PDSe-S (92.5%) > PDSe (87.8%) > PDSe-S₂ (83.1%), as shown in **Figure 3.13**. PDSe-S has the highest energy efficiency is believed that the tri-Se-S bonds are the most stable structure resulting in easy reversible formation and highest efficient reaction. The Se-Se bond of PDSe is weak which is spontaneously breaking. More energy and driving force are needed for the reversible formation, which results in the lower energy efficiency. The PDSe-S₂ provided close energy efficiency to PDSe, but a little lower than it. The reason could be due to the conversion reactions of forming S-S bonds and Se-S bonds. This order is believed to be a result of the complicated effects of the electrical conductivity, bond energy, and sulfur content of these compounds, as well as the different composition and morphology of electrodes containing mixtures of organic and inorganic species. On the other hand, the sulfur content could affect the formation process of these compounds. The difference in

bond energy and disorder in structure could also result in unexpected energy efficiency changes.

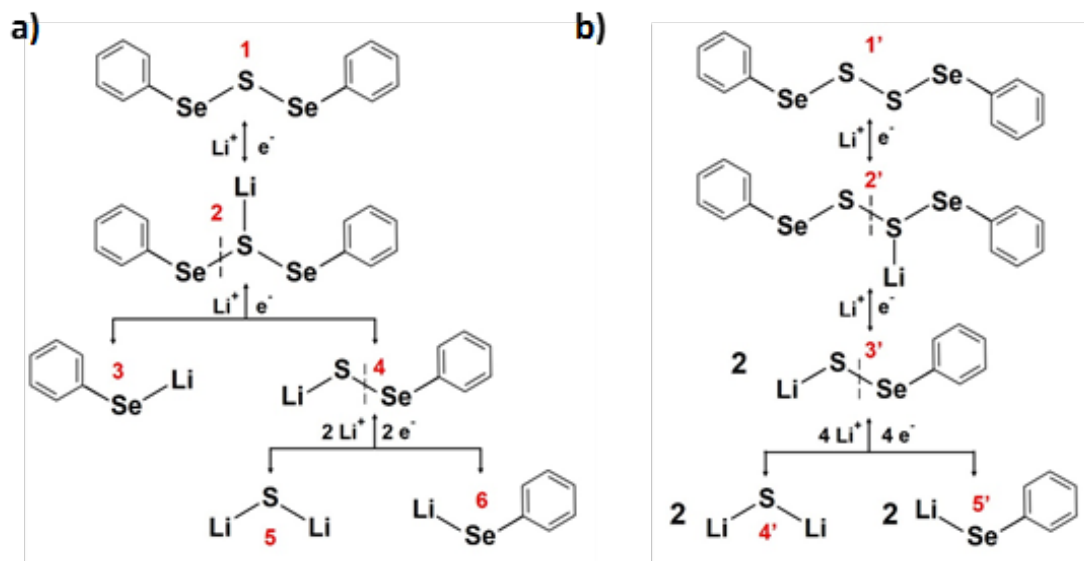


Figure 3.14. Redox reactions of (a) PDSe-S and (b) PDSe-S₂ in rechargeable lithium batteries.

To further understand the electrochemical behavior of PDSe-S and PDSe-S₂, DFT calculations were performed to understand the redox processes. The reaction voltage is determined based on the free energy difference between the reactants and products. The details of the computational method are provided in the experimental section. **Figure 3.14a** and **b** show calculated reaction sequences of PDSe-S and PDSe-S₂, respectively. When PDSe-S is discharged as the initial substance **1**, a Li⁺ and e⁻ are first attracted to the sulfur atom in PhSe-S-SePh to yield the intermediate **2** with an overall reaction energy of $\Delta E = -2.40$ eV, corresponding to a voltage of 2.4 V vs. Li/Li⁺. The calculated lithiation reaction of PDSe-S is shown in **Figure 3.15a**. However, the lithiated PDSe-S **2** is unstable due to the elongated S-Se bond, resulting in a short voltage plateau at 2.4 V. This calculation result explains the shown first short discharge plateau of PDSe-S in **Figure 3.11**. In other words, the intermediate **2** is quickly dissociated into PhSeLi **3** and PhSeSLi **4** by taking another Li⁺ and e⁻,

and the energy difference is calculated to be -2.23 eV, which is consistent with the discharge voltage of 2.2 V. The first and second steps yield a combined capacity of 156 mAh g⁻¹, in close agreement with the experimental observation. The final step is a two-electron reaction to yield Li₂S **5** and another PhSeLi **6**. Because of the formation of Li₂S that potentially blocks the Li diffusion pathway, the two-electron capacity is only partially recovered (100 mAh g⁻¹ out of 156 mAh g⁻¹), which is a phenomenon often observed in Li-S systems.

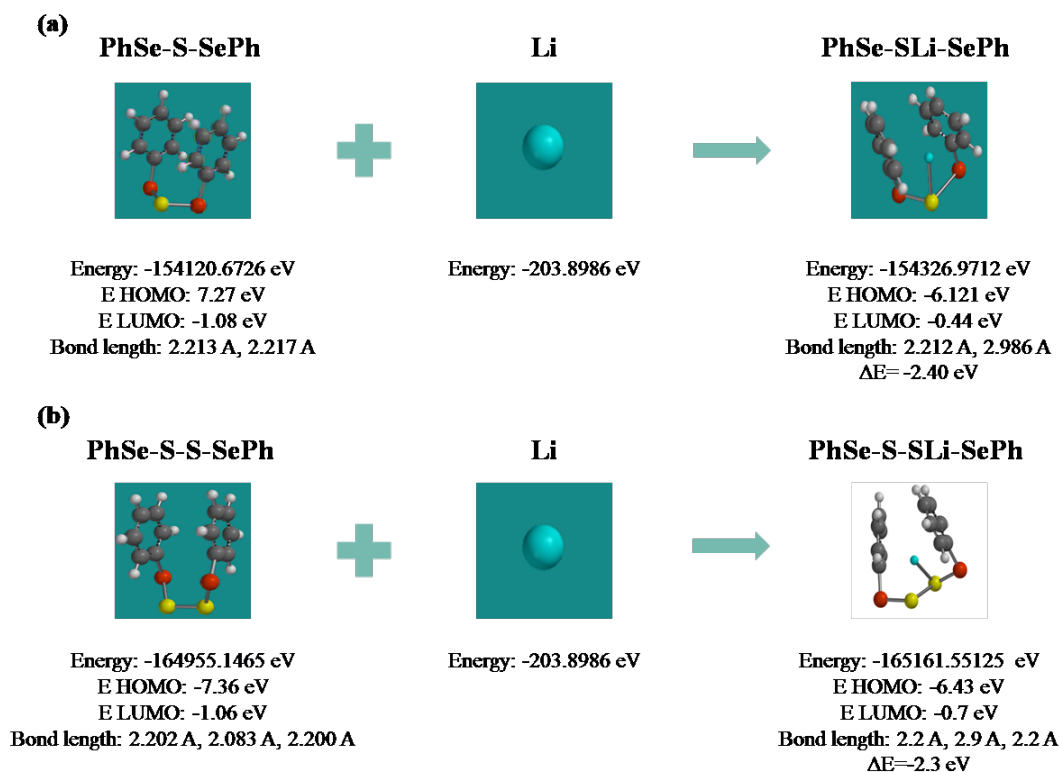


Figure 3.15. The lithiation reaction and energy difference of forming (a) PDSe-S-Li and (b) PDSe-S₂-Li.

The reaction sequence of PDSe-S₂, denoted as **1'**, is shown in **Figure 3.14b**. A Li⁺ and e⁻ are first attracted to a sulfur atom to form the intermediate product **2'**, corresponding to a voltage of 2.3 V vs. Li/Li⁺. The calculated lithiation reaction of PDSe-S₂ is shown in **Figure 3.15b**, which shows the overall reaction energy of

$\Delta E = -2.3$ eV for the lithiation reaction of the single Li^+ attacking to one sulfur atom. Since PDSe-S_2 has 2 sulfur atoms between the selenium atoms, and the first reaction step prefers to be attracted by only one Li^+ , it will form an unbalanced S-S-Li bond. In another word, the S-S bond is highly elongated. Again, the intermediate is not stable due to elongated S-S bond and is dissociated into two PhSeSLi **3'** by taking another Li^+ and e^- , corresponding to a voltage of 2.18 V. The two combined steps give a total capacity of 142 mAh g^{-1} , which is again consistent with the experimental observations. The final step is the reduction of PhSeSLi to form Li_2S **4'** and PhSeLi **5'**, which is the same as the last reaction step for PDSe-S . Because there are two PhSe-SLi molecules per $\text{PhSe-S}_2\text{-SePh}$, this final step gives a total of four-electron capacity of 284 mAh g^{-1} . Again, due to the formation of Li_2S , only around 200 mAh g^{-1} out of 284 mAh g^{-1} is observed. Thereupon the final products of PhSeLi and Li_2S are formed. The computational results are consistent with the experimental data in the voltage profiles. In the reverse process, PDSe-S and PDSe-S_2 could be formed and the formation of polysulfides is prohibited. This is because that in the reverse charging process, only 1 sulfur atom can be added per phenyl diselenide molecule in PDSe-S and at most 2 sulfur atoms can be added per phenyl diselenide molecule in PDSe-S_2 . The long-chain polysulfides (S_{6-8}) will be prohibited during charging.

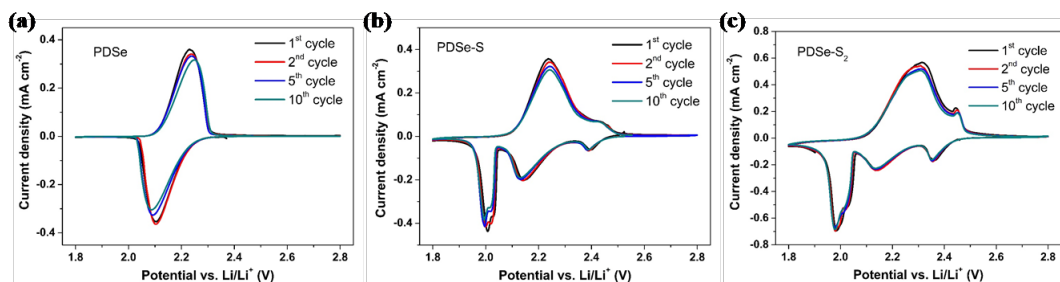


Figure 3.16. Cyclic voltammogram of the 1st, 2nd, 5th, and 10th cycles of (a) PDSe , (b) PDSe-S , and (c) PDSe-S_2 .

The CV plots are shown in **Figure 3.16** for PDSe , PDSe-S and PDSe-S_2 , respectively. In the 10 cycles of PDSe , the peaks shift to more overpotentials. The

single peak in cathodic scan and anodic scan reflects the single one-step reaction in reduction and oxidation reactions. The increased overpotential indicates the growing difficulty in charge diffusion and mass transfer. On the other hand, the CV plots of PDSe-S and PDSe-S₂ are highly overlapped, indicating good reversible reactions sequences. For the CV plot of PDSe-S, the 1st peak and 3rd peak in cathodic scan are highly overlapped with the 2nd peak being barely shifted. The oxidation peaks during 10 cycles show no shift, which indicates promising reversibility. In the CV plot of PDSe-S₂, all the peaks do not show much shifts. For both PDSe-S and PDSe-S₂, especially the major reduction and oxidation peaks without much shifts, indicate promising reversible abilities in the electrochemical field.

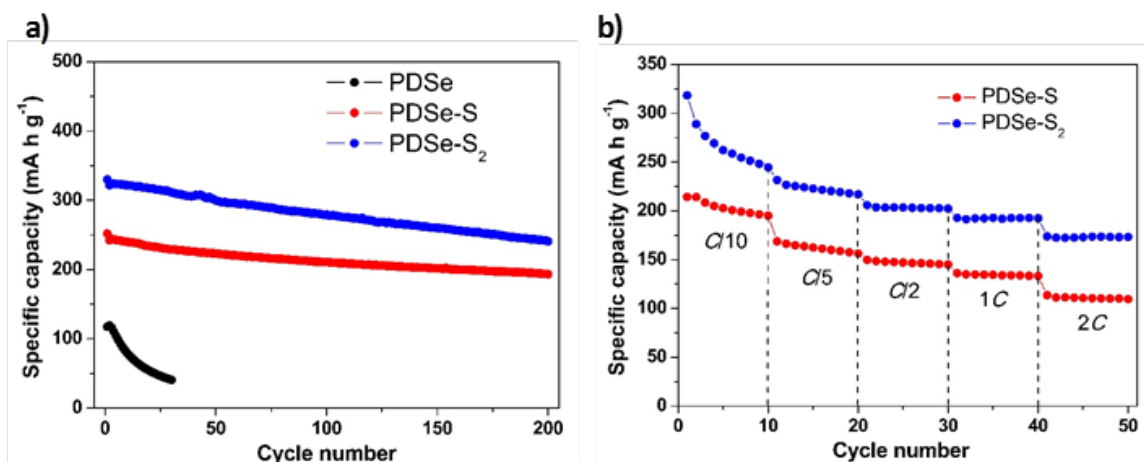


Figure 3.17. Cycling performance (a) of PDSe, PDSe-S, and PDSe-S₂ at C/5 rate, rate performance (b) of PDSe-S and PDSe-S₂ in rechargeable lithium batteries.

With the understanding of electrochemical behaviors and reactions sequences, the cycling performance of PDSe-S and PDSe-S₂ was studied, as shown in **Figure 3.17a**. PDSe is cycled at C/5 rate as the baseline. It shows an initial capacity of 118 mAh g⁻¹ and end capacity of 40 mAh g⁻¹ after 30 cycles. The Coulombic efficiency (CE) starts at 97.8% and drops to 96.1% over this period, as shown in **Figure 3.18**. In contrast, PDSe-S and PDSe-S₂ show much better cycling performance at the same C rate. The initial discharge capacities are 252 mAh g⁻¹ and 330 mAh g⁻¹ for PDSe-S

and PDSe-S₂, respectively. After 200 cycles, the discharge capacity of PDSe-S is 194 mAh g⁻¹ retaining 77% of the initial capacity and the discharge capacity of PDSe-S₂ is 241 mAh g⁻¹ retaining 73% of the initial capacity. The corresponding selected voltage profiles in different cycles are shown in **Figure 3.12**. CEs of PDSe-S and PDSe-S₂ are better than that of PDSe, as shown in **Figure 3.18**. It is believed that the insoluble Li₂S formed in the discharge of these new hybrid compounds helps anchor soluble PhSeLi, therefore improving cycling stability. PDSe-S and PDSe-S₂ are also tested under variable C-rates, as shown in **Figure 3.17b**. PDSe-S shows an initial capacity of 214 mAh g⁻¹ at C/10 and 169 mAh g⁻¹ at C/5. The cell exhibits stable cycling performance with a specific capacity of 150 mAh g⁻¹ at C/2, 136 mAh g⁻¹ at 1C, and 113 mAh g⁻¹ at 2C. PDSe-S₂ shows higher capacities than PDSe-S at the same C-rates, which are 318 mAh g⁻¹ at C/10, 232 mAh g⁻¹ at C/5, 205 mAh g⁻¹ at C/2, 193 mAh g⁻¹ at 1C, and 174 mAh g⁻¹ at 2C, respectively. Different C rates result in different degradation, particularly at C/10, which is because of different conductivity and sulfur contents in these two cells. These results show the promising cycling performance and rate capability of these compounds enabled by integrating sulfur atoms into phenyl diselenide molecules.

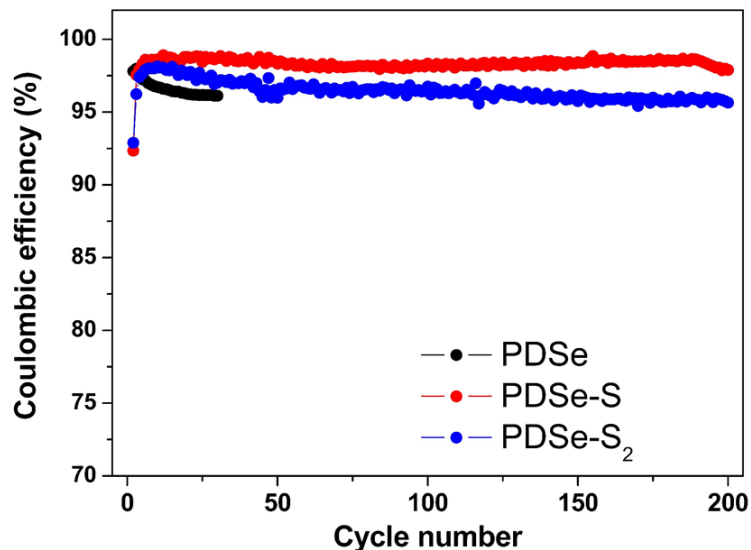


Figure 3.18. Coulombic efficiency (CE) of cells with PDSe, PDSe-S, and PDSe-S₂ electrodes at C/5 rate.

3.5 Conclusion

This study reports a strategy to add redox active sites in PDSe to increase its capacity as cathode materials for rechargeable lithium batteries. The Se-Se bond is easy to break and the addition of sulfur atoms becomes possible. Both computational and MS results confirm the formation of PDSe-S and PDSe-S₂ although some impurities are present in the synthesized samples. These hybrid compounds show interesting electrochemical behavior in lithium batteries with three reversible discharge voltage plateaus involving frequent Se-S and S-S bond break and formation. PDSe-S and PDSe-S₂ show much higher discharge capacities and CEs than PDSe, as well as better cycling stability which is believed to be related to the reduced solubility of discharge products (i.e., Li₂S). In addition, they show steady rate capabilities up to 2C. This strategy adds new members to the family of high-capacity cathode materials and provides a new way to explore Se/S containing hybrid compounds, which are valuable for rechargeable lithium batteries and beyond.

4. ELECTROCHEMICAL BEHAVIOR OF TIN FOIL ANODE IN HALF CELL AND FULL CELL WITH SULFUR CATHODE

4.1 Abstract

Tin-based (Sn) metal anode has been considered an attractive candidate for rechargeable lithium batteries due to its high specific capacity, safety and low cost. However, the large volume change of Sn during cycling leads to rapid capacity decay. To address this issue, Sn foil was used as a high capacity anode by controlling the degree of lithium uptake. We studied the electrochemical behavior of Sn foil anode in half cell and full cell with sulfur cathode, including phase transform, morphological change, discharge/charge profiles and cycling performance. Enhanced cycling performance has been achieved by limiting the lithiation capacity of the Sn foil electrode. A full cell consisting of a pre-lithiated Sn foil anode and a sulfur cathode was constructed and tested. The full cell exhibits an initial capacity of 1142 mAh g⁻¹ (based on the sulfur mass in the cathode), followed by stable cycling performance with a capacity retention of 550 mAh g⁻¹ after 100 cycles at C/2 rate. This study reports a potential prospect to utilize Sn and S as a combination in rechargeable lithium batteries.

4.2 Introduction

Tin-based (Sn) metal anode has attracted much attention as an alternative of graphite anode for the development of high energy density lithium ion batteries (LIBs) due to its high capacity, low cost, abundance and non-toxic property [100]. Sn has theoretical capacities of 993 mAh g⁻¹ and 2094 Ah L⁻¹ according to the forma-

tion of $\text{Li}_{4.4}\text{Sn}$, which are about 3 times of the capacities of graphite (372 mAh g^{-1} and 740 Ah L^{-1}) [101, 102]. However, the large volume change (260%) upon lithiation/delithiation processes leads to Sn particles fracture and electrodes delamination from the current collector, which result in rapid capacity decay [103]. Although much effort has been made to alleviate these issues for achieving high capacity and good cycle life, such as nano-structuring Sn [104] and developing Sn-based composite materials [105], the large volume change upon cycling is still a hurdle for the practical applications of Sn anodes. In addition to the Sn particle-based composite electrodes including binder, carbon additive and current collector, bulk Sn foil has also been used to study its crystallographic changes during lithiation/delithiation processes and understand the mechanisms of capacity fade. For instance, Rhodes et al. monitored the phase transformation behavior of sputtered Sn thin films throughout an entire lithiation/delithiation cycle using in-situ X-ray diffraction (XRD) [106]. The presence of four phases including white Sn, Li_2Sn_5 , $\beta\text{-LiSn}$, and $\text{Li}_{22}\text{Sn}_5$ were identified. Hassoun et al. reported the preparation and characterization of various samples of metallic Sn electroplated on a copper foil under different current and time regimes [107]. Tamura et al. investigated an electrodeposited Sn layer on copper foil [108]. They found that the poor cycle life was resulted from a lack of interface strength between the entire part of the active material and the current collector. Yang et al. studied the behavior of a bulk Sn foil electrode [109]. They concluded that the poor cycle life is related to an inability to completely remove all the inserted lithium. Recently, an interdigitated eutectic alloy including Sn and aluminum (Al) has been developed as a high capacity anode [110]. In this eutectic alloy, nanosized electrochemically active Sn domains are surrounded by an electrically conductive Al network, which enables stable cycling.

Bulk Sn foil electrode offers several advantages over the particle-based composite electrode, such as ease of fabrication, very high fraction of active materials and high volumetric capacity. In addition, bulk Sn foil can be easily pre-lithiated and used as the anode for LIBs, in which the cathode does not contain lithium at the charged state, such as lithium sulfur battery. There have been few studies on silicon-sulfur batteries

[111], lead-sulfur batteries [112], and especially the Sn-sulfur batteries. Hassoun and Scrosati developed a tin sulfur LIB using Sn/C composite as the anode and $\text{Li}_2\text{S}/\text{C}$ composite as the cathode [113]. They concluded that the use of a Sn/C composite anode eliminates the risk of shuttle effect, which is a major problem in lithium sulfur battery using a lithium metal anode. However, the Sn/C composite anode still cannot offer good cycle life due to the large volume change of Sn. It has been proposed that limiting the degree of lithium uptake in Sn could relieve the fracture problem to some extent. Due to the advantage of high capacity offered by bulk Sn electrode, we hypothesize that it is possible to develop a bulk Sn foil anode with both high capacity and good cycle life by limiting the degree of lithium uptake. In commercial LIBs, the realized capacity of graphite anode is $\sim 150 \text{ mAh g}^{-1}$ when the weights of the copper current collector, conductive carbon, and polymer binder are included. If the lithium uptake of bulk Sn foil electrode is limited to 20%, it still has a capacity of 198 mAh g^{-1} , which is higher than the realized capacity of graphite anode. If we consider half of the volume of the graphite electrode is occupied by graphite, the realized volumetric capacity is about 370 Ah L^{-1} . The capacity of bulk Sn foil electrode is 418 Ah L^{-1} , considering 20% lithium uptake.

Therefore, the objective of this paper is to investigate the electrochemical behavior of bulk Sn foil anode in both half-cell and full cell with sulfur cathode. In this work, we studied the phase transform of Sn foil anode by analyzing ex-situ XRD data at different state of charge during lithiation processes. A thin copper layer was sputtered on one side of the Sn foil as a protective layer to improve electrical connection between Sn anode and the coin cell case. By controlling the lithium concentration of the lithiation and phase transform, an enhanced cycle life of 90 cycles can be obtained. We also incorporated the Sn foil anode with a sulfur cathode in ether-based electrolyte as a full cell. The morphological changes at anode after cycling and the electrochemical phenomena were studied [114].

4.3 Experimental

4.3.1 Materials and Instruments

All materials were used as received and listed in table 4.1. All instruments used were listed in table 4.2.

Table 4.1. Materials

Chemical Name	Purity	Provider
Tin foil (Sn, 0.025mm thick)	99.9% (metals basis)	Alfa Aesar
Lithium bis(tri-fluoromethanesulfonimide) (LiTFSI, $\text{LiN}(\text{CF}_3\text{SO}_2)_2$)	99%	Acros Organics
Lithium nitrate (LiNO_3)	99.999%	Acros Organics
1,2-dimethoxyethane (DME)	99.5%	Sigma Aldrich
1,3-dioxolane (DOL)	99.8%	Sigma Aldrich
Sulfur (S)	99.5%	Alfa Aesar
Super C65 (conductive carbon black)	N/A	Timcal
Polyvinylidene fluoride (PVdF)	N/A	Kureha Battery Materials Japan Co., Ltd.
1-methyl-2-pyrrolidone (NMP)	99.5%	Sigma Aldrich
Carbon disulfide (CS_2)	Certified ACS	Fisher Scientific

Table 4.2. Instruments

Instrument	Provider
Battery cyclers	Arbin BT2000
VSP potentiostat	BioLogic
Copper sputtering source	AJA international
Vacuum Oven	Isotemp 281A
Glove box	MBraun
Scanning electron microscopy (SEM)	JEOL JSM-7800F
X-ray diffraction (XRD)	Bruker D8 Discover XRD Instrument

4.3.2 Electrolyte preparation

The blank electrolyte is composed of 1.0 M LiTFSI in mixture solvent of DME and DOL (1:1 v/v). The S-Sn full cell electrolyte is composed of 1.0 M LiTFSI and 0.1 M LiNO₃ in mixture solvent of DME and DOL (1:1 v/v).

4.3.3 Preparation of Sn anode and S cathode

Sn foils were polished by a piece of sandpaper (2500 grit) to remove the native oxide layer and then cleaned by Acetone for several times. One piece of the cleaned Sn foil was cut into 0.49 cm² discs ($D = 7.9$ mm, including 9.5 mg Sn each) as pristine Sn electrodes for XRD collection. Another piece of the cleaned Sn foil was covered with a copper (Cu) layer on one side of the Sn foil through magnetron sputtering deposition method. The sputtering was carried using a source target (AJA international) in a home-built high vacuum chamber. A base pressure of 10^{-6} Torr was maintained while during deposition and an inert argon atmosphere was introduced at a pressure of 10^{-3} Torr. Gas flow rate was regulated by a mass flow controller (MKS, model 250) to

create and maintain a localized, steady plasma above the biased Cu target. Deposition rate was calibrated to be 0.22 nm s^{-1} using a harmonic single crystal monitor attached to the deposition chamber. Thin Cu film of $\sim 500 \text{ nm}$ was deposited on the Sn foil sample. Then the sputtered Sn foil was cut into 0.49 cm^2 discs for Sn half-cell test, and 0.7 cm^2 discs ($D = 9.5 \text{ mm}$, including 13.5 mg Sn each) for pre-lithiation as the anode in S-Sn full cells. All the cut Sn foil electrodes were stored in an Ar-filled glove box.

Commercial binder-free carbon nanotube (CNT) paper called buckypaper (NanoTechLabs Composites, Inc) was used as the current collector for the sulfur electrode in this study. The CNT paper was cut into 0.49 cm^2 discs ($D = 7.9 \text{ mm}$, about 0.9 mg each) and dried at $100 \text{ }^\circ\text{C}$ for 24 h in a vacuum oven before use. 1.5 M sulfur solution was prepared by adding sulfur into CS_2 . The solution was stirred to be dissolved completely. Then $10 \text{ }\mu\text{L}$ solution was added into the CNT current collector in a petri dish. The CNT current collector with S was dried in a vacuum oven at room temperature for 24 h . The mass loading of sulfur on CNT current collector is approximately 1 mg cm^{-2} .

4.3.4 Preparation of carbon-coated separator

The carbon-coated separator was fabricated by surface coating commercial conductive carbon black (Super C65) on one side of a commercial polypropylene separator (Celgard 2400). The carbon slurry was prepared by mixing Super C65 carbon and PVdF in NMP solvent with the ratio of 8:2 (Super C65: PVdF) for 24 h . The carbon slurry was coated onto the Celgard 2400 using a doctor blade and then dried at $35 \text{ }^\circ\text{C}$ for 24 h in a vacuum oven. The carbon-coated separator was then cut into 1.77 cm^2 circular disks ($D = 15 \text{ mm}$, Celgard 2400 mass is about 2.5 mg each, carbon mass is about 0.8 mg (0.45 mg cm^{-2})).

4.3.5 Sn half-cell fabrication and electrochemical evaluation

CR2032 coin cells were used and cells were fabricated in an Ar-filled glove box. First, a stainless-steel plate was placed in coin cell case. A Sn foil electrode (0.49 cm^2) was placed on the plate and inserted into coin cell with the copper side facing down, followed by adding $10 \mu\text{L}$ blank electrolyte. Then a Celgard 2400 separator was placed on top of the Sn electrode followed by adding another $10 \mu\text{L}$ blank electrolyte on top of the separator. Then a piece of lithium metal was placed on the separator. Finally, a stainless-steel plate covered the lithium metal with a spring as the spacer. The cell was crimped and taken out of the glove box for electrochemical evaluation.

Cells were galvanostatically cycled between 0.35 and 1.2 V on an Arbin BT2000 battery cycler at 0.03 C rate ($1\text{C} = 993 \text{ mA g}^{-1}$, based on the mass of Sn in the cells). The lithiation capacity limited cells were galvanostatically cycled between 0.01 and 1.2 V at 0.03 C rate with 1 mAh lithiation capacity limitation (2.04 mAh cm^{-2}). The cell for low current analysis was galvanostatically cycled at $10 \mu\text{A cm}^{-2}$. Cyclic voltammetry (CV) was performed on a BioLogic VSP potentiostat. The potential was swept from open circuit voltage to 0.35 V and then swept back to 1.2 V at a scanning rate of 0.05 mV s^{-1} .

For XRD collection, cells were fabricated by using pristine Sn electrodes followed by the same procedure, which avoids the strong effect of copper under x-ray diffraction. These cells were galvanostatically cycled between 0.01 and 1.2 V at 0.03 C rate. Different lithiation status were collected by limiting the lithiation capacity.

4.3.6 S half-cell fabrication and electrochemical evaluation

CR2032 coin cells were used and cells were fabricated in an Ar-filled glove box. First, $15 \mu\text{L}$ full cell electrolyte was added into the prepared CNT paper electrode. Then a Celgard 2400 separator was placed on top of the electrode followed by adding another $15 \mu\text{L}$ electrolyte on the separator. Finally, a piece of lithium metal and nickel foam as a spacer were placed on the separator. The cell was crimped and taken out

of the glove box for electrochemical evaluation. Cells were galvanostatically cycled on an Arbin BT2000 battery cycler at 0.2 C rate ($1C = 1672 \text{ mA g}^{-1}$, based on the mass of sulfur in the cells). CV was performed on a BioLogic VSP potentiostat. The potential was swept from open circuit voltage to 1.7 V and then swept back to 2.8 V at a scanning rate of 0.02 mV s^{-1} .

4.3.7 Sulfur-tin full cell fabrication and electrochemical evaluation

To pre-lithiate the Sn anode, a Sn (0.7 cm^2) half-cell was fabricated by following the same Sn half-cell fabrication procedure shown in section 4.3.5. Then the cell was galvanostatically cycled between 0.35 and 1.2 V with 1.5 mAh (2.1 mAh cm^{-2}) lithiation capacity limitation for 4 cycles. Then the cell was opened to obtain the lithiated Sn anode. To fabricate a S-Sn full cell, a stainless-steel plate was placed in coin cell case. A sulfur cathode was placed on the plate followed by adding $15 \mu\text{L}$ full cell electrolyte. Then a carbon-coated separator was placed on top of the sulfur cathode and inserted into coin cells with the carbon side facing the cathode, followed by adding another $15 \mu\text{L}$ full cell electrolyte on top of the separator. Finally, the lithiated Sn anode was placed on the separator with a spring as the spacer. The cell was crimped and taken out of the glove box for testing.

Cells were galvanostatically cycled between 1.1 and 2.3 V on an Arbin BT2000 battery cycler at C/2 rates ($1C = 1672 \text{ mA g}^{-1}$, based on the mass of sulfur in the cells). CV was performed on a BioLogic VSP potentiostat. The potential was swept from open circuit voltage to 1.1 V and then swept back to 2.3 V at a scanning rate of 0.05 mV s^{-1} .

4.3.8 Characterization

The XRD data were collected on a Bruker D8 Discover XRD Instrument equipped with Cu K α radiation. The pristine Sn foil was placed on a glass slide and protected with Kapton film. The scanning rate was $0.5^\circ \text{ min}^{-1}$, and 2θ was set between 20° and

90°. The cycled Sn electrodes for XRD were obtained by opening the Sn half-cells in an Ar-filled glove box. The cycled electrodes were dried under vacuum in a chamber of the glovebox for 30 min. Then the XRD samples were prepared by following the same procedure. The XRD patterns were collected under the same conditions for comparison.

The cycled Sn electrodes for scanning electron microscopy (SEM) were obtained by opening the S-Sn full cells in an Ar-filled glove box, followed by the same drying procedure. The morphological characterization of the electrodes was conducted with a JEOL JSM-7800F field emission SEM. The elemental mapping was performed with energy-dispersive X-ray spectroscopy (EDS) attached to the SEM with 7 KV.

4.4 Results and discussion

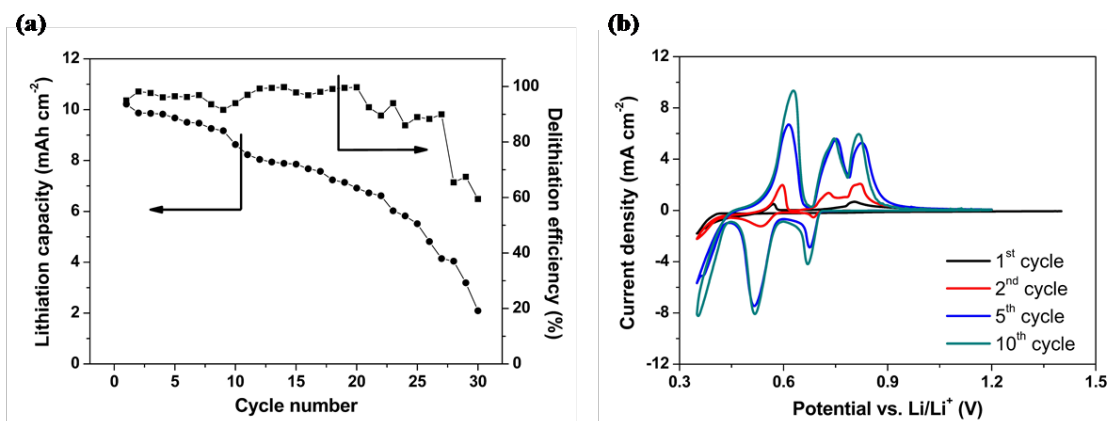


Figure 4.1. (a) Cycling performance of the Sn foil at 0.03 C rate, (b) cyclic voltammogram of the 1st, 2nd, 5th, and 10th cycles.

The Sn foil electrode was galvanostatically cycled between 0.35 and 1.2 V at 0.03 C rate. The cycling performance is shown in **Figure 4.1a**. The Sn foil electrode has an initial capacity of 10.2 mAh cm⁻² and the capacity decreases to 2.1 mAh cm⁻² after 30 cycles. The cell has an initial Coulombic efficiency (CE) of 95%, followed by an average efficiency of >90% over 20 cycles, then the efficiency fades to 60% after

30 cycles. This performance is not a well cycling performance for an anode material which can only maintain stable cycling less than 10 cycles. The electrochemical behavior was studied via CV, as shown in **Figure 4.1b**. In the cathodic scan from open circuit voltage (OCV) to 0.35 V, no obvious peaks are observed until 0.4 V, at which the lithiation occurs in the 1st cycle. In the 2nd cycle, the lithiation mainly occurs at 0.69 V, 0.56 V and 0.39 V. The delithiation process is reversed in the anodic scan presented by three separated peaks at 0.61 V, 0.73 V and 0.8 V, respectively.

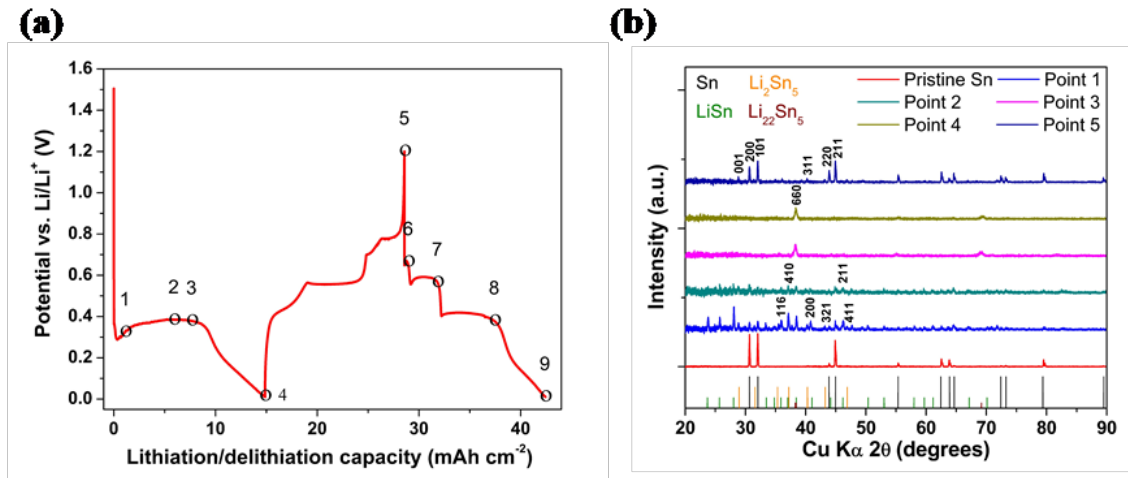


Figure 4.2. (a) Voltage-capacity profile showing collected XRD patterns points, (b) XRD patterns of the Sn foil in the 1st cycle.

The voltage profile of the Sn foil is shown in **Figure 4.2a**, which resembles the CV. There is only one discharge voltage plateau in the first lithiation process, and there are multiple plateaus in the following cycle. To understand the phase transformation during these processes, ex-situ XRD patterns were collected at different states of lithiation, which are shown in **Figure 4.2** and **Figure 4.3**, at which the chosen points are for the whole first cycle and the second lithiation process, respectively. The XRD pattern of the pristine Sn foil shows strong peaks of (200), (101) and (211) planes and weaker peak of (220) plane. A continuous diminution in the Sn peak intensity is firstly observed on the first lithiation plateau (point 1-3), followed by the

presence of the Li_2Sn_5 and LiSn phases. At the end of the single lithiation plateau (point **3**), the mainly present phase is detected to be $\text{Li}_{22}\text{Sn}_5$, mixing with small parts of Li_2Sn_5 and LiSn . At the end of lithiation (point **4**), the Sn peaks completely disappear and the XRD pattern only shows peaks of $\text{Li}_{22}\text{Sn}_5$. After the electrode was charged to 1.2 V (point **5**), the delithiated product is also scanned by XRD. It is observed that the Sn phase appears again, which is mixed with Li_2Sn_5 and LiSn meaning an incomplete delithiation process after the cell was charged to 1.2 V.

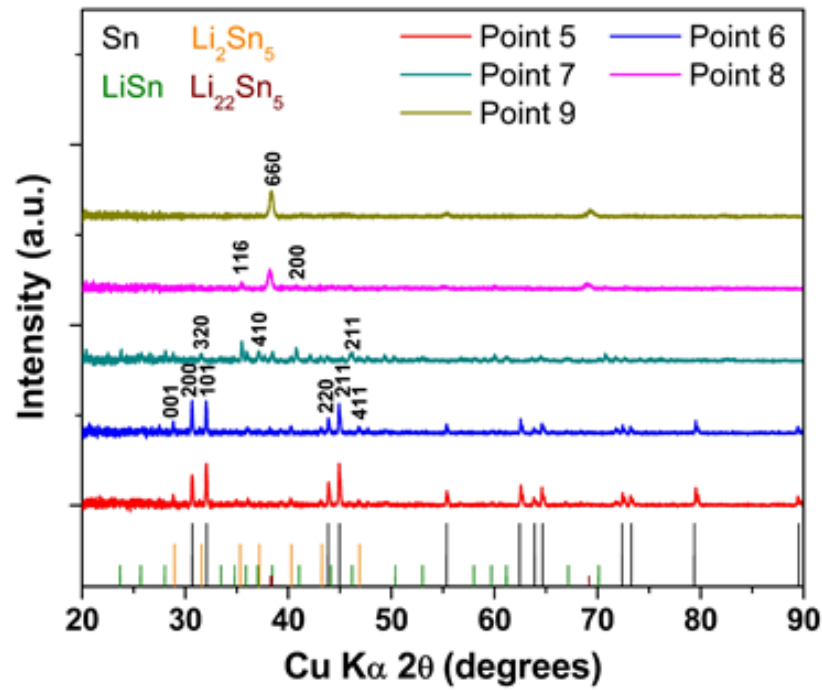


Figure 4.3. XRD patterns of the Sn foil in the 2nd cycle.

The XRD patterns of the 2nd lithiation process are shown in **Figure 4.3**. The voltage profile shows three typical plateaus, on which four scan points were collected to detect the phase changes. The four collected data are corresponding to the terminals of the three voltage plateaus and the completed lithiation stage, respectively. At the end of the 1st voltage plateau (point **6**), the decreased intensity of Sn peaks is due to depleting Sn upon lithiation. The transformed phases are mainly Li_2Sn_5 and LiSn .

phases. At the end of the 2nd plateau (point **7**), the XRD pattern shows that the Sn phase completely disappeared. Li_2Sn_5 is the mainly crystalline phase mixed with a small amount of LiSn. After the 3rd lithiation plateau (point **8**), $\text{Li}_{22}\text{Sn}_5$ phase with high intensities is shown accompanied with abridged presence of the LiSn phase. After discharging to 0.01 V (Point **9**), $\text{Li}_{22}\text{Sn}_5$ phase is the only detected crystalline lithiation phase.

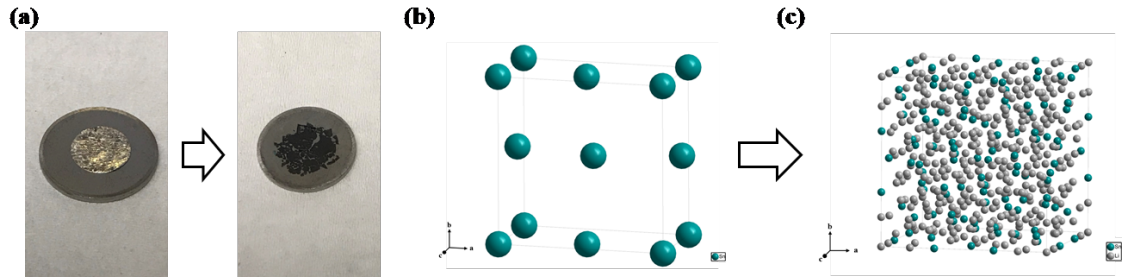


Figure 4.4. (a) Pictures showing the morphological changes from pristine Sn foil to lithiated product, the atomic structures of (b) Sn and (c) $\text{Li}_{22}\text{Sn}_5$. Tin and lithium atoms are represented in green and gray, respectively.

The mainly changed phases for Sn being lithiated are between Sn crystals and $\text{Li}_{22}\text{Sn}_5$. The morphological change from pristine Sn foil to lithiated Sn at 0.01 V is shown in **Figure 4.4a**. The pristine Sn foil has a polished surface with metallic luster. When it is fully lithiated to $\text{Li}_{22}\text{Sn}_5$, the foil becomes dark black and cracked into pieces. The large volume expansion results in the pulverization of the Sn foil, which is the main reason of the contact loss and fast capacity decay. **Figure 4.4b** and **c** show the crystal structure change from Sn to $\text{Li}_{22}\text{Sn}_5$. The Sn crystal initially has a cubic structure. The $\text{Li}_{22}\text{Sn}_5$ mainly adopts a Body-Centered Cubic structure [106]. The XRD results show Li_2Sn_5 and LiSn are the main transition crystalline structures. No other high degree phases of lithiation such as Li_7Sn_3 , $\text{Li}_{13}\text{Sn}_5$ and Li_7Sn_2 are detected. It does not mean that these crystals are not existing. Instead of it, many different crystal phases can be found from the material structures database, like Li_2Sn_5 , LiSn, Li_7Sn_3 , $\text{Li}_{13}\text{Sn}_5$ and Li_7Sn_2 and so on. However, different crystals have different

formation or detection conditions. The database can be used to predict the possible formed crystal phases, which needs to be fitted by the real experimental conditions and then further calculated by the detected parameters of the crystal lattice.

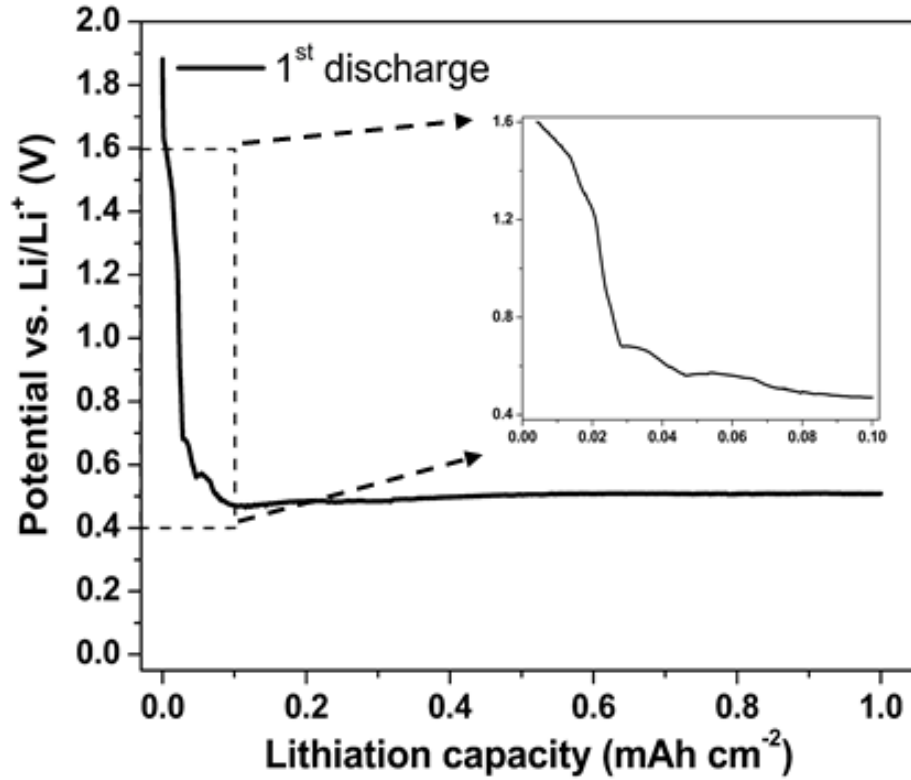


Figure 4.5. Voltage-capacity profile of the Sn foil at $10 \mu\text{A cm}^{-2}$ current density.

It is observed that the first lithiation process only has one plateau, which is different from the 2nd lithiation with three typical plateaus. The long plateau in the first lithiation has been considered as the result of disorder in the initially formed material [109]. We believe that this unique phenomenon could be due to the large difference in lithium diffusivities between lithium poor phases and lithium rich phases of the lithium tin alloys [115]. As shown in Ref. [116], the lithium diffusivity in lithium poor phases (before LiSn) is about one order lower than that in the lithium rich phases. We can assume the lithium transport in the Sn foil electrode is a 1-D transport. From

the surface of the Sn foil electrode (facing separator), the lithium concentration decreases gradually from high to 0. Due to the difference between the high diffusivity in lithium rich phases and the low diffusivity in lithium poor phases, it is favorable to form lithium rich phases on the surface. At very low rate, the lithium poor phases could be detected on the surface and the plateaus could be visible. As shown in **Figure 4.5**, the three plateaus appear at the beginning of lithiation when the current density is $10 \mu\text{A cm}^{-2}$. Since the XRD patterns in **Figure 4.2b** do not show the existence of $\text{Li}_{22}\text{Sn}_5$ in points **1** and **2**, other lithium rich phases are believed to exist before the appearance of $\text{Li}_{22}\text{Sn}_5$. These lithium rich phases cannot be detected by XRD. The possible reasons could be (1) they are amorphous; (2) they are too small or too transient to be detected [106]. As shown in **Figure 4.2a**, the typical plateaus can appear in the 2nd lithiation. We believe that it is due to two reasons. The first reason is the significant surface area increase due to the pulverization, which results in low current density. The second reason is the inhomogeneity of the pulverized Sn foil. The lithium transport can no longer be considered as a 1-D transport.

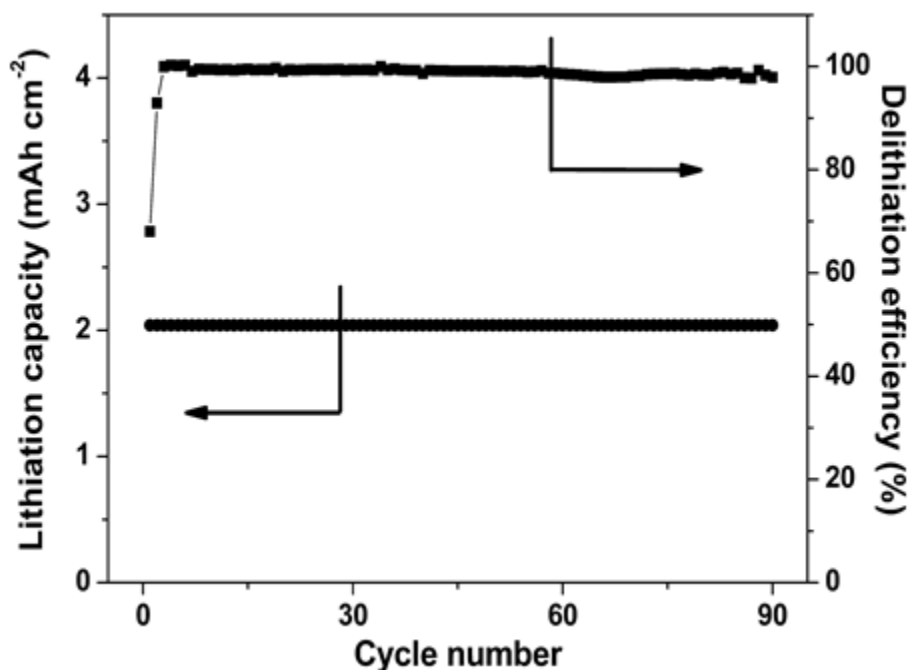


Figure 4.6. Cycling performance of the Sn foil at 0.03 C rate with lithiation capacity limit of 2.04 mAh cm⁻².

To avoid the large volume expansion of the Sn foil electrode, the state of lithiation was controlled. Enhanced cycling performance can be achieved for more than 90 cycles by limiting the lithiation capacity of the Sn foil electrode at 1 mAh (2.04 mAh cm⁻²), as shown in **Figure 4.6**. The CE starts at 68% in the initial cycle, and then increases to 96% in the second cycle. After that, it stays at a steady efficiency of >97% until the 90th cycle. By controlling the lithium uptake at 2.04 mAh cm⁻², the phase transitions to Li_xSn_y have been controlled to lithium poor phases (Li₂Sn₅ and LiSn). The lithium poor phases can only cause a small volume expansion for the Sn foil electrode. From the values reported in a literature, the relative volume V_r is 1.22 for Li₂Sn₅, and 1.51 for LiSn. But the lithium rich phase (Li₂₂Sn₅) has a relative volume of 3.58, which causes the cracking [117]. This lithiation control avoids the transition to lithium rich phase, herein maintains the structural stability and enhances the cycling performance. This controlled lithiation method has one major weakness

which is the loss of the achieved capacity, although the longer cycling performance can be obtained. On the other hand, it is one of the efficient ways to achieve a much longer and more stable cycling life by the compromise of the experimental conditions.

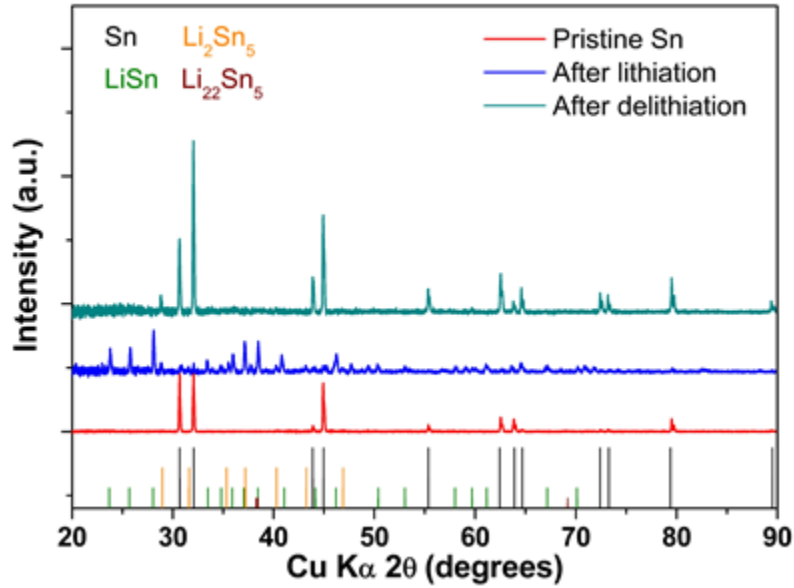


Figure 4.7. XRD patterns in the 1st cycle of the Sn foil at 0.03 C rate with lithiation capacity limit of 2.04 mAh cm⁻².

To confirm the working principle of this controlled lithiation method, XRD is used to detect the phase changes for the Sn foil electrode, as shown in **Figure 4.7**. The pristine Sn foil is the XRD pattern that we have discussed before. At the end of lithiation of the controlled 2.04 mAh cm⁻², the XRD pattern shows that the formed phases are Li₂Sn₅ and LiSn phases, but no Li₂₂Sn₅ phase. It could be either the Li₂₂Sn₅ phase is completely avoided, or the amount of formed Li₂₂Sn₅ is so rare that it cannot be detected. Overall, the lithium rich phase like Li₂₂Sn₅ is avoided to form by this controlled lithiation method at the end of lithiation. After the delithiation process, the Li₂Sn₅ and LiSn are converted to Sn, which indicates the good reversibility of the lithium poor phases. This promising reversibility provides a possibility to show good cycling performance.

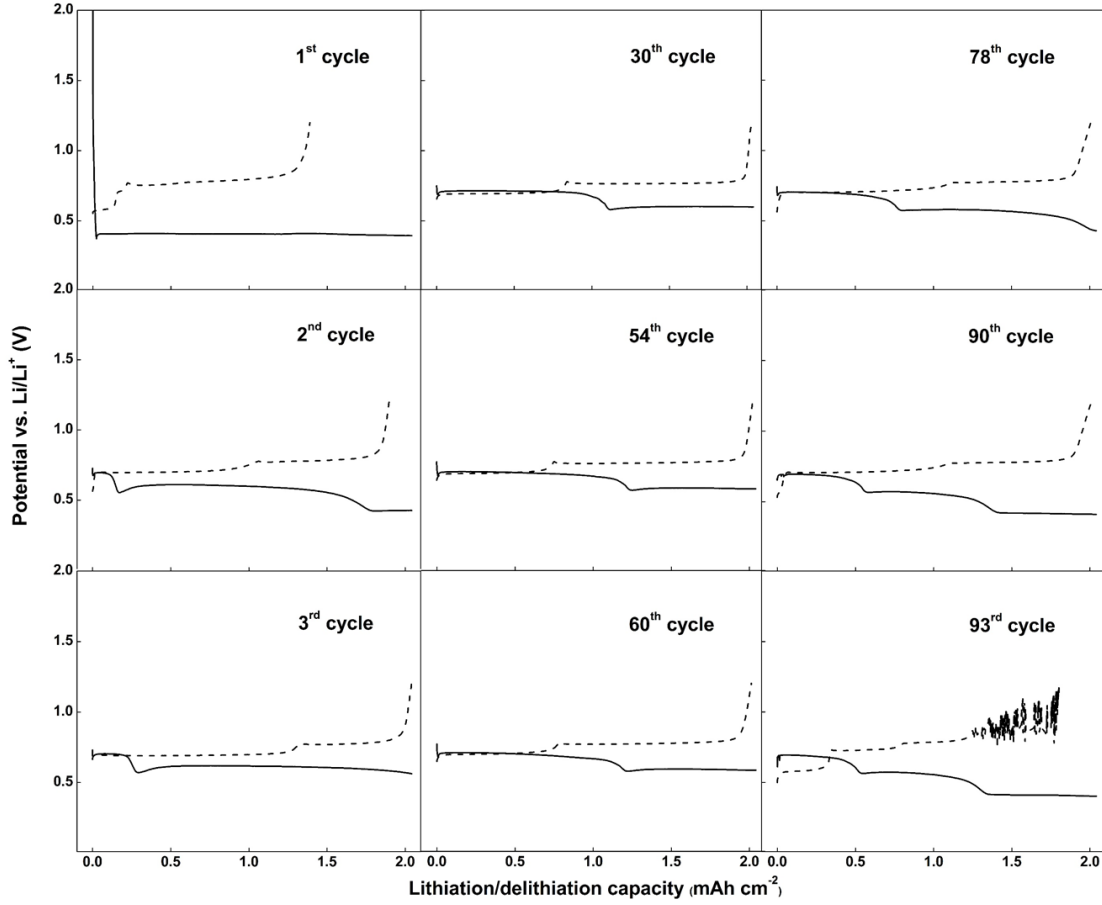


Figure 4.8. Selected voltage-capacity profiles of the Sn foil at 0.03 C rate with lithiation capacity limit of 2.04 mAh cm^{-2} .

Selected voltage profiles in different cycles are shown in **Figure 4.8**. The initial discharge process shows a single lithiation plateau at 0.4 V and the charge process shows two very short plateaus at 0.61 V and 0.73 V and a long plateau at 0.8 V. In literature, the charge plateau at 0.61 V is considered the transition from $\text{Li}_{22}\text{Sn}_5$ to LiSn . Our results show that this plateau could also be a transition from other lithium rich phases to LiSn . The plateau at 0.73 V is the transition from LiSn to Li_2Sn_5 and the plateau at 0.8 V is the transition from Li_2Sn_5 to Sn . The first charge profile can also be explained by the different diffusivities between lithium rich phases and lithium poor phases. Since the lithiation capacity was controlled, the major phases in the Sn

foil electrode are lithium poor phases (LiSn and Li_2Sn_5) after the first discharge. As indicated by the 0.4 V discharge plateau, there should be some lithium rich phases on the surface of the Sn foil electrode. At the beginning of the charge process, the lithium rich phases on the surface of Sn foil are transferred to LiSn and then Li_2Sn_5 very quickly. The XRD pattern at the end of the first charge shows the left Li_2Sn_5 and LiSn in the delithiation products, which explains the low CE of the first cycle. The discharge profile in the 2nd cycle shows three plateaus. The first and the third ones are short and the second one is long. The possible reason is the pulverization generated in the first cycle. The second charge profile shows two plateaus. The plateau at 0.61 V does not exist, which is in agreement with the short third plateau in the discharge profile, meaning the existence of very little lithium rich phases. From the third cycle to the 54th cycle, the voltage profiles have two lithiation plateaus and two delithiation plateaus, which means the phases are changed between Sn and lithium poor phases (Li_2Sn_5 and LiSn). However, the profiles also show that the length of the Sn/ Li_2Sn_5 plateau keeps increasing and the length of the $\text{Li}_2\text{Sn}_5/\text{LiSn}$ plateau keeps decreasing for both discharge and charge profiles. It means that minor cracks inside the Sn foil are generated and the surface area is increased continuously. The larger surface area promotes the formation of Li_2Sn_5 . After the 54th cycle, the length of the Sn/ Li_2Sn_5 plateau keeps decreasing and the length of the $\text{Li}_2\text{Sn}_5/\text{LiSn}$ plateau keeps increasing for both discharge and charge profiles. After the 78th cycle, the third plateau appears again, and its length continuously increases. After the 93rd cycle, the voltage profiles start to become unstable and have large voltage drop. We believe that it is because the pulverization become severe enough to generate isolated particles and the active surface area start to decrease after the 54th cycle. After the 93rd cycle, the Sn foil electrode is completely pulverized and most of the Sn materials are isolated. The cycling performance demonstrates the cycling performance of Sn foil can be improved by controlling the state of lithiation. However, fracture still happens due to the $\sim 50\%$ volume change between Sn and LiSn . Eventually, pulverization will cause the failure of the Sn foil electrode after 90 cycles.

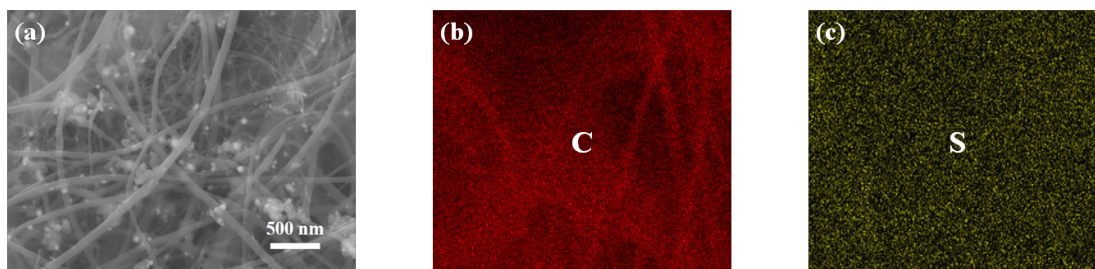


Figure 4.9. (a) SEM image and (b-c) EDS scan for carbon and sulfur in the sulfur cathode.

Sulfur has attracted much attention as a promising cathode material due to its high theoretical specific capacity (1672 mAh g^{-1}) [118]. In this study, the sulfur cathode was prepared by using a solvent evaporation method applied by our group before [41]. The sulfur solution was prepared in carbon disulfide (CS_2) and injected into a CNT paper. Sulfur particles are evenly distributed within the CNT paper once CS_2 solvent is vaporized. The sulfur loading is 1.0 mg cm^{-2} , which is about 56% of the capacity of 0.7 cm^2 prelithiated Sn foil. The higher capacity of the Sn anode is to ensure the excess lithium resource for the possible waste of lithium due to polysulfides shuttle effect and the SEI formation. SEM and EDS were performed to examine the morphology and elemental distribution in the prepared electrodes, as shown in **Figure 4.9a-c**, respectively. The SEM image in **Figure 4.9a** shows the structural morphology of the prepared sulfur/CNT electrode. It can be seen that a lot of regular sulfur particles were deposited in the voids of the CNT paper. Under the detection of SEM, the sulfur particles are in nanoscale. The EDS in **Figure 4.9b** and **c** reveal the carbon element in the CNT paper network structure and the uniform distribution of sulfur element in the electrode. The electrode prepared by this method promises reliable and controllable deposition of sulfur in CNT paper.

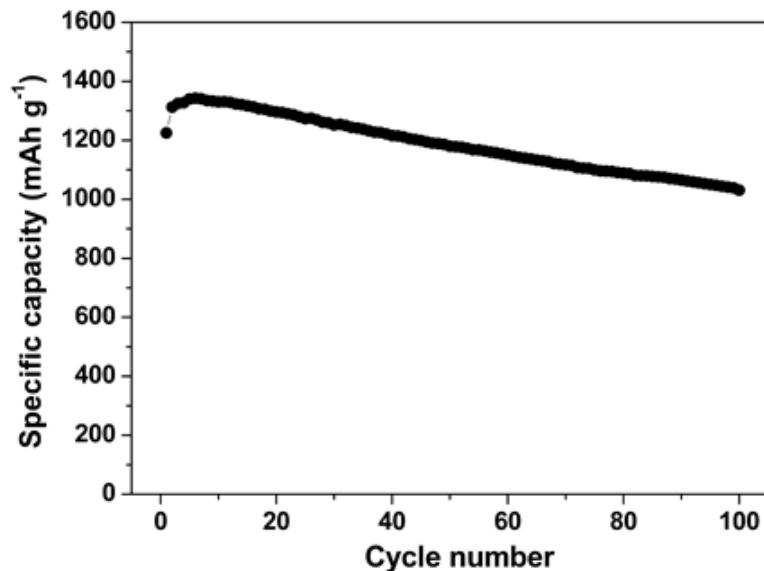


Figure 4.10. Cycling performance of the sulfur cathode.

The cycling performance of the S cathode at C/5 is shown in **Figure 4.10**. The sulfur cathode delivers 1225 mAh g^{-1} in the 1st cycle, and then the capacity increases to 1312 mAh g^{-1} in the 2nd cycle. After 100 cycles, the specific capacity is stabilized at 994 mAh g^{-1} . The result demonstrates that the sulfur cathode prepared by this method is robust in retaining active material thus offering stable cycling performance. Since this contribution is not for studying the sulfur cathode, so its performance will not be discussed in detail here. The cycling performance of sulfur is just to show that this prepared sulfur on CNT cathode can provide a stable cycling life, which is suitable for combination with the lithiated Sn anode.

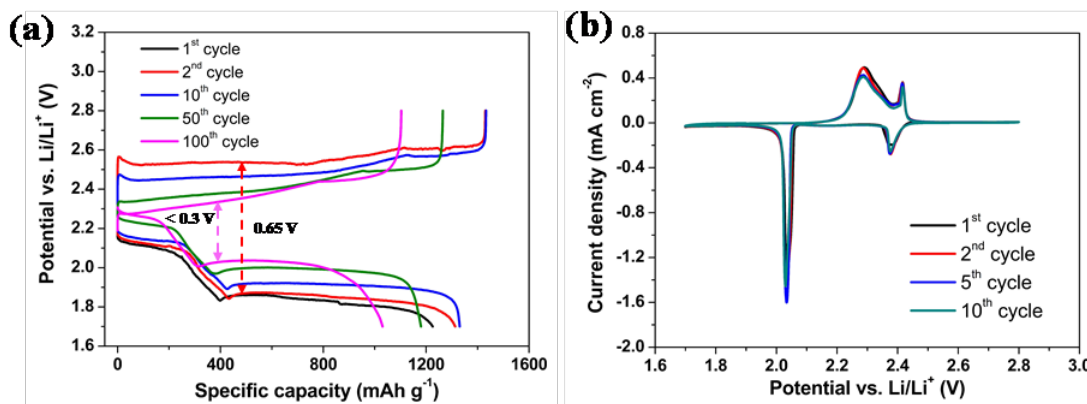


Figure 4.11. (a) Selected voltage-capacity profiles, and (b) cyclic voltammogram of the sulfur cathode.

Selected voltage profiles for the sulfur cathode are shown in **Figure 4.11a**. The cell is discharged to 1.7 V to avoid the LiNO₃ reduction reactions at low potential (≤ 1.65 V). The sulfur cathode has two visible plateaus in the discharge and two plateaus in the charge. It can be observed that the cell polarization (the voltage difference between the first charge voltage plateau and the second discharge voltage plateau) is 0.65 V in 2nd cycle. Then it continuously decreases to lower than 0.3 V during cycling. **Figure 4.11b** shows the CV of the Li-S cell. There are two cathodic peaks at 2.37 V and 2.05 V corresponding to the reduction reactions of sulfur to low-order polysulfides and low-order polysulfides to Li₂S, and two distinguishable anodic peaks at 2.28 V and 2.41 V, which indicate the transition of Li₂S to high-order polysulfides/sulfur. The cell exhibits a stable CV profile over 10 cycles without decay of peak intensity.

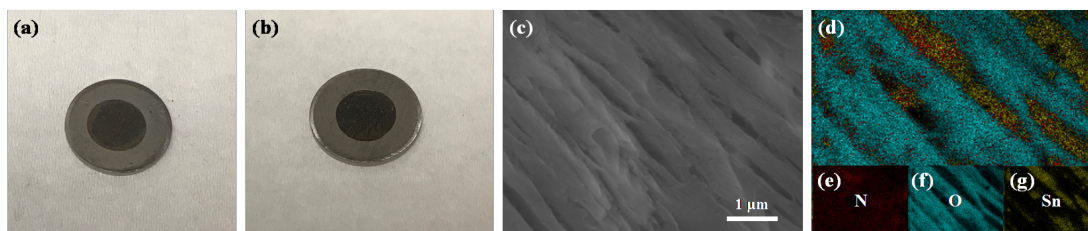


Figure 4.12. (a) Picture of the Sn foil after pre-lithiation, (b) picture of the Sn foil, (c) SEM image and (d-g) EDS scan for overlapping, nitrogen, oxygen and tin for the Sn foil anode at discharged state after 10 cycles in the S-Sn full cell.

The sulfur cathode and the controlled lithiation Sn anode are confirmed to provide stable cycling life in half-cells, therefore it is possible to combine them to work as a full cell. To set up a S-Sn full cell, the Sn foil electrode was cycled with 1.5 mAh capacity limitation (2.1 mAh cm^{-2}) for 4 cycles for prelithiation. As shown in **Figure 4.12a**, the foil still maintains its structural stability after pre-lithiation, due to the limited lithiation capacity, low cycling current (0.03 C), and homogenous lithiation process. The Sn foil anode from the cycled S-Sn full cell was also obtained at discharged state after 10 cycles, as shown in **Figure 4.12b**. Compared to the image shown in **Figure 4.12a**, it did not have significant changes after 10 cycles in the S-Sn full cell. SEM was performed to investigate the anode extracted from the full cell at discharged state, as shown in **Figure 4.12c**. In this high magnification, it can be observed that the anode surface has formed porous structures. It means that fracturing still happens even the lithium uptake is limited. The EDS map of overlapping, nitrogen species, oxygen species and tin species is shown in **Figure 4.12d-g**. The nitrogen and oxygen elements could be from the passivation layer from LiNO_3 and the SEI layer. They could also be from the residual lithium salts. The EDS mapping result shows that some of the electrode areas are not covered by the passivation layer. We believe that it is due to the volume change of Sn electrode during lithiation/delithiation processes.

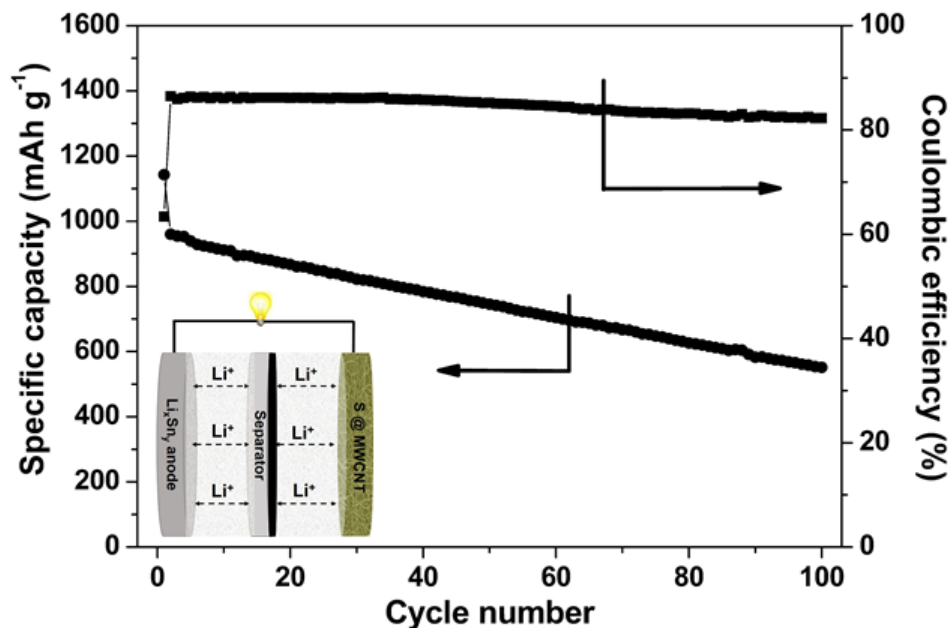


Figure 4.13. Cycling performance with an inset schematic of construction of the S-Sn full cell.

When sulfur cathode is coupled with the lithiated Sn anode and cycled at $C/2$, the cycling performance in **Figure 4.13** is observed, with an inset picture showing the schematic construction of the S-Sn full cell. The full cell has an initial capacity of 1143 mAh g^{-1} in the 1st cycle, and then yield the capacity of 960 mAh g^{-1} in the 2nd cycle. The full cell exhibits stable cycling performance with remaining reversible capacity of 552 mAh g^{-1} after 100 cycles. The full cell has an initial CE of 64% and retaining efficiency of >82%. Although the volume change of Sn keeps exposing fresh Sn surfaces and leads to new SEI formation, the CE shown in **Figure 4.6** is higher than 96%. The low CE shown in the S-Sn full cell means that LiNO_3 is not as effective as in the Li-S cell to prevent the shuttle effect. The Sn surface is not completely covered by the passivation layer as shown in **Figure 4.12**.

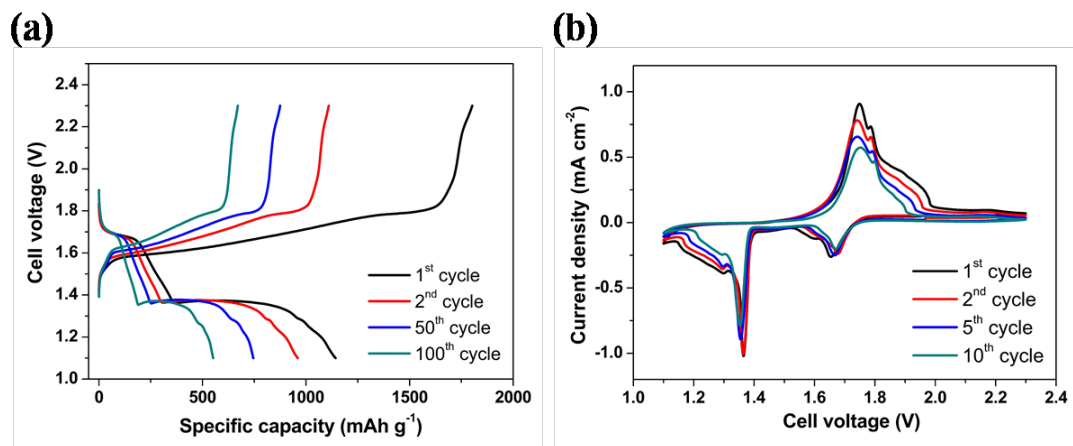


Figure 4.14. (a) Selected voltage-capacity profiles and (b) cyclic voltammogram of the S-Sn full cell.

The full cell operating voltage profile is shown in **Figure 4.14a**. During discharge, two plateaus are shown. The first reduction plateau is at 1.7 V which is corresponding to the combination of formation from sulfur to low-order polysulfides and lithium extraction from lithiated Sn anode. The second discharge plateau is at 1.36 V, which is attributed to the formation of Li₂S and low-order lithiated Sn. The charge process is a highly reversible process with two charge plateaus around 1.6 V and 1.8 V, respectively. The first cycle has a long charge process, which results in a low CE. The capacity fade during conversion process is due to the consumption of lithium upon prolonged cycling and shuttle effect of high order polysulfides. The CV for the S-Sn full cell is shown in **Figure 4.14b**. There are two cathodic peaks at 1.65 and 1.37 V corresponding to the reduction reactions of sulfur to low-order polysulfides and low-order polysulfides to Li₂S. The second cathodic peak is obviously the overlap of two peaks with a miniature peak at 1.3 V. The peak could be attributed to the phase transform of Sn anode leading the voltage change. In the anodic scan, two distinguishable peaks are observed at 1.74 and 1.79 V, which indicate the transition from Li₂S to high-order polysulfides/S as a conversion process. The cell exhibits a stable CV profile over 10 cycles without large decay of peak intensity. The cycling result

of S-Sn full cell demonstrates that shuttle effect of polysulfides is still a major issue. Polysulfides can react with lithium in the lithium tin alloy and LiNO_3 cannot form a seamless passivation layer to protect lithium tin alloy surface. The performance of such a system could be further improved by applying high loading carbon interlayers, modification of polysulfide carbon host, and other functionalized materials such as graphene and polymers to contain lithium polysulfides in the cathode.

4.5 Conclusion

In this work, Sn foil has been studied as a high capacity anode for lithium batteries. By controlling the degree of lithium uptake, a stable long cycling life can be obtained for Sn foil anode. Ex-situ XRD results and lithiation/delithiation profiles show that the different lithium diffusivity between lithium poor phases and lithium rich phases have significant impact on the electrochemical performance of Sn foil. A S-Sn full cell has been developed by using pre-lithiated Sn foil anode and S/CNT cathode and it shows high specific capacity. However, the CE is lower than 90% mainly due to the shuttle effect of polysulfides. LiNO_3 is not effective in forming passivation layer on the lithiated Sn anode as it is in the lithium sulfur batteries. New approach needs to be developed to prevent the shuttle effect. Although the shuttle effect is not evaded from the full cell system, it provides a concept and potential for further studying the S-Sn full cell system.

5. SELENIUM NANOCOMPOSITE CATHODE WITH LONG CYCLE LIFE FOR RECHARGEABLE LI-SE BATTERIES

5.1 Abstract

Selenium (Se) is a potential cathode material for high-energy density rechargeable lithium batteries. In this study, a binder-free Se-carbon nanotubes (CNTs) composite electrode has been prepared by a facile chemical method. At initial state, Se is in the form of branched nanowires with a diameter of <150 nm and length of $1\text{--}2\text{ }\mu\text{m}$, interweaving with CNTs. After discharge and re-charge, they are converted to nanoparticles embedded in the CNT network. This synthesis method provides a path for fabricating the Se cathodes with controllable mass loading and thickness. By studying the composite electrodes with different Se loadings and thicknesses, we found that the electrode thickness has a critical impact on the distribution of Se during repeated cycling. Promising cycling performance was achieved in thin electrodes with high Se loading. The composite electrode with $23\text{ }\mu\text{m}$ thickness and 60% Se loading shows a high initial capacity of 537 mAh g^{-1} , followed by stable cycling performance with a capacity of 401 mAh g^{-1} after 500 cycles at 1C rate. This study reports a synthesis strategy to obtain Se/CNT composite cathode with long cycle life for rechargeable Li-Se batteries.

5.2 Introduction

In the past two decades, lithium-ion batteries (LIBs) have been extensively utilized in portable electronic devices as well as electric vehicles (EVs). However, conventional LIBs depending on the lithium intercalation reactions of anode and transitional metal

oxide cathode materials have limited capacities and low energy densities, which prevent their broader deployment as power sources for prolonged usage. High energy density and durable electrical energy storage devices are the key factors to meet the crucial demands for high-performance portable electronic devices and EVs. Lithium-sulfur (Li-S) batteries have attracted particular interest and been proposed as the next-generation rechargeable systems, due to the high theoretical specific capacity (1672 mAh g^{-1}) and high theoretical energy density (2600 Wh kg^{-1}) of sulfur. In addition, the characteristics of sulfur such as low cost, abundance, and environmental benignity make it attractive to be an electrode material. Despite these advantages, Li-S batteries are facing challenges toward practical applications, including the insulating nature of sulfur ($5 \times 10^{-28} \text{ S m}^{-1}$), large volume change (up to 80%) upon cycling, so-called shuttle effect and active materials loss over repeated cycling. Various strategies have been developed to address these challenges, including using carbon matrix hosts, utilizing optimized electrolyte, constructing carbon layers, and adjusting functional polymers. However, the intrinsic weaknesses of Li-S batteries have not been completely solved.

Selenium (Se), as a congener of sulfur in the periodic table, has been proposed as an alternative cathode material for rechargeable lithium batteries. Although Se has lower theoretical capacity (678 mAh g^{-1}) than sulfur, it can provide a high volumetric capacity of 3253 mAh cm^{-3} because of its high mass density (4.8 g cm^{-3}) [18]. In addition, selenium has a much higher electronic conductivity ($1 \times 10^{-3} \text{ S m}^{-1}$), which implies that Se could provide better electrochemical activity [119]. However, Se cathode is still facing similar challenges as sulfur such as poor cycling life and low Coulombic efficiency, which are attributed to the dissolution and shuttle effect of the formed high-order polyselenides as redox intermediates in the ether-based electrolyte. In addition, the significant volume change increases the difficulty for Li-Se batteries to be used in practical applications [80]. During the last decade, lots of effort have been put into developing approaches to address these problems, thereby increasing energy density and cycle life of Li-Se batteries. For instance, Zhang et al. sealed

Se nanowires by polyaniline to form core-shell structure and then encapsulated the composite material using graphene to improve the cycling performance [120]. Zeng et al. confined Se in 3-dimensional interconnected mesoporous carbon nanofibers as a flexible and binder-free electrode [82]. He et al. added carbon nanotubes/Se between graphene layers to form high performance binder-free Se cathodes [121].

In this contribution, we synthesized Se nanowires in the presence of carbon nanotubes (CNTs) by a facile method. Se nanowires are weaved with CNTs to form a uniform binder-free composite electrode, which has superior electrical conductivity. This synthesis method provides a path for fabricating the Se cathodes with controllable mass loadings and thicknesses. By studying the composites electrodes with different mass loadings of active materials and different thicknesses, it is found that the electrode thickness has influence on the accumulation of redox products upon repeated cycling. The structural and morphological changes are analyzed by scanning electron microscope (SEM). Finally, the electrochemical phenomena are revealed experimentally, and enhanced cycling performance is achieved [122].

5.3 Experimental

5.3.1 Materials and Instruments

All materials were used as received and listed in table 5.1. All instruments used were listed in table 5.2.

Table 5.1. Materials

Chemical Name	Purity	Provider
Lithium bis(tri-fluoromethanesulfonimide) (LiTFSI, $\text{LiN}(\text{CF}_3\text{SO}_2)_2$)	99%	Acros Organics
Lithium nitrate (LiNO_3)	99.999%	Acros Organics
1,2-dimethoxyethane (DME)	99.5%	Sigma Aldrich
1,3-dioxolane (DOL)	99.8%	Sigma Aldrich
Ethanol	Anhydrous	Fisher Scientific
Selenium oxide (SeO_2)	99.8% trace metal basis	Acros Organics
Beta-cyclodextrin (β -cyclodextrin)	98%	Acros Organics
Ascorbic acid ($\text{C}_6\text{H}_8\text{O}_6$)	N/A	LabChem
Long multiwalled carbon nanotubes(CNTs, length: 30-100 μm)	95+%	Nanostructured Amor Materials, Inc.
Medium multiwalled carbon nanotubes(CNTs, length: 10-50 μm)	95%	Nanostructured Amor Materials, Inc.

Table 5.2. Instruments

Instrument	Provider
Battery cycler	Arbin BT2000
VSP potentiostat	BioLogic
Differential scanning calorimetry (DSC)	TA 2000 instruments SDT Q600 analyzer
Vacuum Oven	Isotemp 281A
Glove box	MBraun
Transmission electron microscope (TEM)	JEOL 2100
Scanning electron microscopy (SEM)	JEOL JSM-7800F
X-ray diffraction (XRD)	Bruker D8 Discover XRD Instrument

5.3.2 Preparation of electrolyte

The electrolyte is composed of 1.0 M LiTFSI and 0.2 M LiNO₃ in a mixture solvent of DME and DOL (1:1 v/v).

5.3.3 Preparation of selenium nanowires/CNTs composite cathode

Selenium nanowires/CNTs composite cathode was synthesized according to the literature with some modifications. In this study, two set of the selenium nanowires with CNTs composite electrodes were prepared. Firstly, ascorbic acid was dissolved in de-ionized water to render a 0.03 M solution. The first set of composite electrodes with different selenium nanowires loadings were synthesized in this study by adjusting the reactant amounts. SeO₂ (0.25 g and 0.35 g) and β -cyclodextrin (0.25 g and 0.35 g), respectively, were added into a glass beaker with adjunction of 50 mL de-ionized water. The mixture was magnetically stirred to fully dissolve. Then 60 mg CNTs (30 mg long CNTs/ 30 mg medium CNTs) was added into the clear solution,

followed by adding 500 mL anhydrous ethanol. The mixture was vigorously stirred for about 10 min, and then it was ultrasonicated by using a Sonics vibracell VC505 sonicator for 5 min for dispersion. The prepared ascorbic acid solution (48 mL and 68 mL, respectively) was added into this mixture under continuous stirring. After reacting for 24 h, the mixture was ultrasonicated for 10 min causing the selenium nanowires and CNTs to interweave. The products were vacuum filtered onto a 7-cm-diameter filter paper and washed repeatedly with de-ionized water and anhydrous ethanol for several times. The formed cathode was a free-standing and flexible film. The cathode was dried under vacuum at 40-45 °C for 24 h to yield the selenium nanowires/CNTs composite film. The film was cut into $\sim 0.97 \text{ cm}^2$ discs ($D = 11 \text{ mm}$) and transferred into an Ar-filled glovebox for further handling and testing. The synthesized composite electrodes are named SeCE-1 and SeCE-2 corresponding to the reactant amounts of SeO_2 of 0.25 g and 0.35 g, respectively. The other set of the thin composite electrode was prepared by using SeO_2 and β -cyclodextrin (0.35 g/0.35 g) as reactants, and ascorbic acid solution (68 mL) with CNTs (30 mg/30 mg) following the same procedure. While doing the vacuum filtration, only 33.3% of the prepared product ($\sim 200 \text{ mL}$ prepared selenium/CNTs in water/ethanol mixture solution) was filtered to form a thin composite electrode. It was named as TSeCE corresponding to the reactant amounts of SeO_2 of 0.35 g. The TSeCE was also cut into $\sim 0.97 \text{ cm}^2$ discs ($D = 11 \text{ mm}$) and transferred into an Ar-filled glovebox for further handling and testing.

5.3.4 Cell fabrication and electrochemical evaluation

When assembling cells using the thick composite electrodes (SeCE-1 and SeCE-2), CR2032 Coin cells were used and cells were fabricated in an Ar-filled glove box. First, 15 μL electrolyte was added into the prepared composite electrode. Then a Celgard 2400 separator was placed on the top of the electrode followed by adding 15 μL electrolyte on the separator. Finally, a piece of lithium metal and nickel foam as a

spacer was placed on the separator. The cell was crimped and taken out of the glove box for electrochemical evaluation. While assembling cells using the thin composite electrodes (TSeCE), they were followed by the same procedure except for changing the added electrolyte to 10 μL on both sides.

Cells were galvanostatically cycled on an Arbin BT2000 battery cycler at different C rates ($1\text{C} = 678 \text{ mA g}^{-1}$, based on the mass of material in the cells) and in voltage ranges (C/10 and C/5: 1.8-2.8 V, C/2: 1.75-2.8 V, 1C and 2C: 1.7-2.8 V, 3C, 4C and 5C: 1.65-2.8 V). Cyclic voltammetry (CV) was performed on a BioLogic VSP potentiostat. The potential was swept from open circuit voltage to 1.8 V and then swept back to 2.8 V at a scanning rate of 0.02 mV s^{-1} .

5.3.5 Characterizations

Thermogravimetric analysis (TGA) and differential scanning calorimetry (DSC) was performed on a TA 2000 instruments SDT Q600 analyzer. All the samples are between 5-7 mg and tested under Air flow at 50 mL min^{-1} while heating from 80 to $600 \text{ }^{\circ}\text{C}$ with temperature ramping rate of $5 \text{ }^{\circ}\text{C min}^{-1}$.

The morphological characterization of the selenium nanowires/CNT composite cathode was conducted with a JEOL JSM-7800F field emission scanning electron microscopy (SEM). The elemental mapping was performed with energy-dispersive X-ray spectroscopy (EDS) attached to the SEM at 7 kV to confirm the presence of selenium and carbon in the electrodes. The transmission electron microscope (TEM) images were taken by a JEOL 2100 field emission TEM at 200 kV.

The X-ray diffraction (XRD) data of the pristine electrode, discharged electrode, and charged electrode were collected on a Bruker D8 Discover XRD Instrument equipped with $\text{Cu K}\alpha$ radiation. The scanning rate was 1.2 min^{-1} , for 2θ between 20° and 70° . The cycled electrode samples were obtained by opening the cells and rinsed by pure DME in the glovebox. Then the electrodes were dried in the chamber under vacuum and protected with Kapton tape.

5.4 Results and Discussion

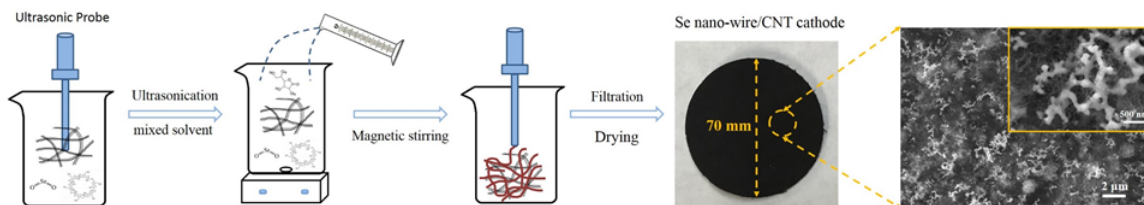


Figure 5.1. Schematic of the experimental procedure synthesizing the selenium nanowire and CNT composite electrode, with the SEM image showing the morphology of the composite electrode.

The experimental process for preparing the Se/CNT composite is schematically illustrated in **Figure 5.1**. The process consists of dissolving selenium oxide (SeO_2) and beta-cyclodextrin (β -cyclodextrin) and dispersing the CNT bundles in an ethanolic mixture with de-ionized water. The vigorously stirring and ultrasonication procedure in the initial mixture cause fine dispersion of CNTs. On the other hand, the ultrasonication initially before reactions happening also ensures the reactants captured by CNTs. In addition, the ethanol extenuates the hydrophobic activity of CNTs, and hence accelerates the dispersion-weave process by ultrasonication. The addition of ascorbic acid solution ensures the product of selenium nanowires. Selenium is not soluble in water or ethanol. The synthesized selenium nanowires are effectively confined and encapsulated by the interwoven CNTs as precipitations out of the solution. Upon another ultrasonication for selenium nanowires and CNTs to be perfectly woven, and then filtered and dried, the Se/CNT composite electrode was obtained. The filter paper has a diameter of 7 cm, which decides the overall size of the composite electrode. SEM was performed to examine the morphology of the composite, as shown in **Figure 5.1**. The SEM image shows that the synthesized selenium nanowires are completely encapsulated by CNTs, leading to a uniformly distributed composite. The inset magnified SEM image reveals that the selenium products are long nanometer-sized wires with uniform diameters, interweaving with CNTs.

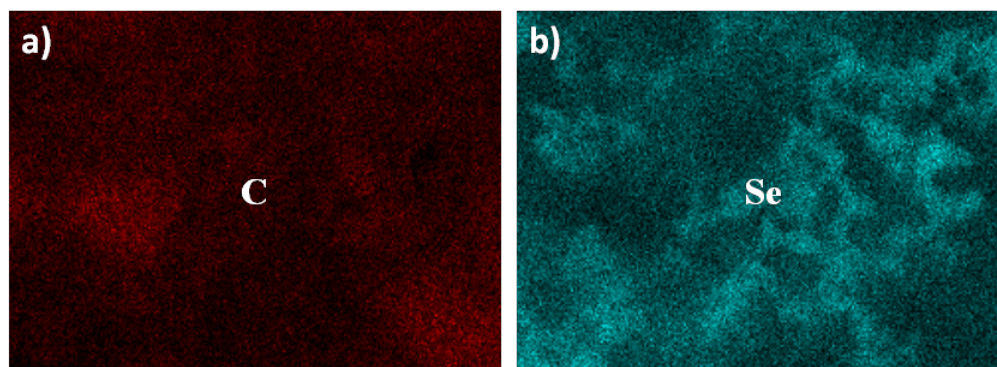


Figure 5.2. EDS scan for (a) carbon and (b) selenium of the selenium nanowire/CNT composite electrode.

Electron dispersive spectroscopy (EDS) was also performed to investigate the elemental distribution, as shown in **Figure 5.2**. The EDS reveals the distribution of carbon and selenium elements in the composite cathode. The distributed carbon in the elemental mapping is from the CNTs. Since the interwoven CNTs current collector is even and uniform, therefore the intensity is almost the same everywhere for carbon. The difference between high intensity and low intensity positions are mainly due to the non-flat scanning. On the other hand, the intensity of selenium is in huge difference at different places. The elemental mapping of selenium matches with shape of the synthesized selenium nanowires. The low intensity positions could be from the covered selenium at deep places.

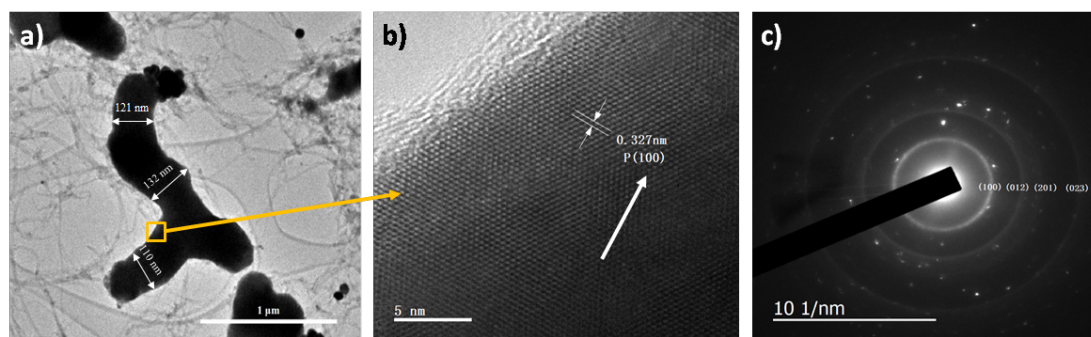


Figure 5.3. (a) TEM image, (b) HRTEM image and (c) SAED pattern of the synthesized selenium nanowires.

The structural estimation of the synthesized selenium nanowires is taken from the transmission electron microscopy (TEM) image in **Figure 5.3a**. The synthesized selenium was firstly ultrasonicated in a solvent for obtaining single and detached nanowires. In the TEM image, the nearly transparent nanowires are the carbon nanotubes, and the light dark nanowires are the synthesized selenium nanowires. It can be observed that the size of the selenium nanowires is approximately 120 nm in diameter. **Figure 5.3b** shows a high resolution TEM (HRTEM) image of the marginal region of a selenium nanowire, which is highlighted by the yellow square and arrow. In the crystalline part, the observed fringe spacing is 0.327 nm, which agrees well with the lattice spacing of the (100) planes of selenium, confirming that the as-selected region is single crystal in the cylindrical margin. The corresponding selected area electron diffraction (SAED) of the as-prepared selenium nanowires is shown in **Figure 5.3c**. The SAED image exhibits diffraction rings corresponding to the (100), (012), (201) and (023) planes of the cylindrical phase, which confirms that polycrystallinity of the as-prepared selenium nanowires.

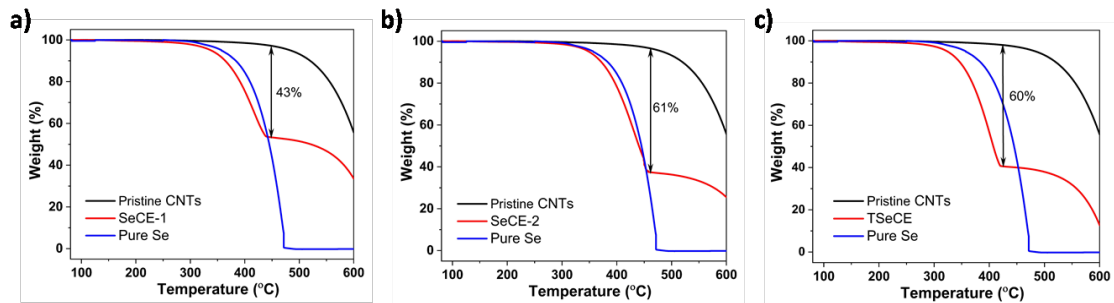


Figure 5.4. TGA plots of the initial (a) SeCE-1, (b) SeCE-2 and (c) TSeCE.

To further characterize the Se/CNT composite, thermogravimetric analysis (TGA) and differential scanning calorimetry (DSC) were performed. Two sets of the composites were prepared by adjusting the reactant amounts and regulating the vacuum filtration, the first set of composite electrodes are named as SeCE-1 and SeCE-2, and the second set of the thin composite electrode is named as TSeCE. Based on the

experimental design, the first set of the composite electrode is much thicker than the second set of the composite electrode. Among them the SeCE-2 and TSeCE should have similar selenium percentage. The TGA was firstly performed to confirm the selenium nanowires loading in each set of the composite cathodes, as shown in **Figure 5.4**. The TGA plots for SeCE-1 and SeCE-2 reveal that the selenium nanowires constitute approximately 43 wt.% and 61 wt.% in the composite, respectively. The TGA plot for TSeCE reveals that the mass component of selenium nanowires is approximately 60 wt.% in the composite electrode. SeCE-1 and SeCE-2 have similar thickness due to the mass of the used CNTs are the same for them, but with different selenium mass loadings. This set of the composite electrode can be used to study the effects of the mass loading percentage on cycling performance. SeCE-2 and TSeCE are chosen as the primary samples in this study because they have similar high selenium loading percentage and much discrepancy in thickness. This is an important comparison to understand the effects of thickness of the composite electrodes on electrochemical behaviors. According to the TGA results, the mass loadings of the selenium nanowires in the composite cathodes are 1.3 mg cm^{-2} in SeCE-1, 2.3 mg cm^{-2} in SeCE-2, and 0.88 mg cm^{-2} in TSeCE, respectively.

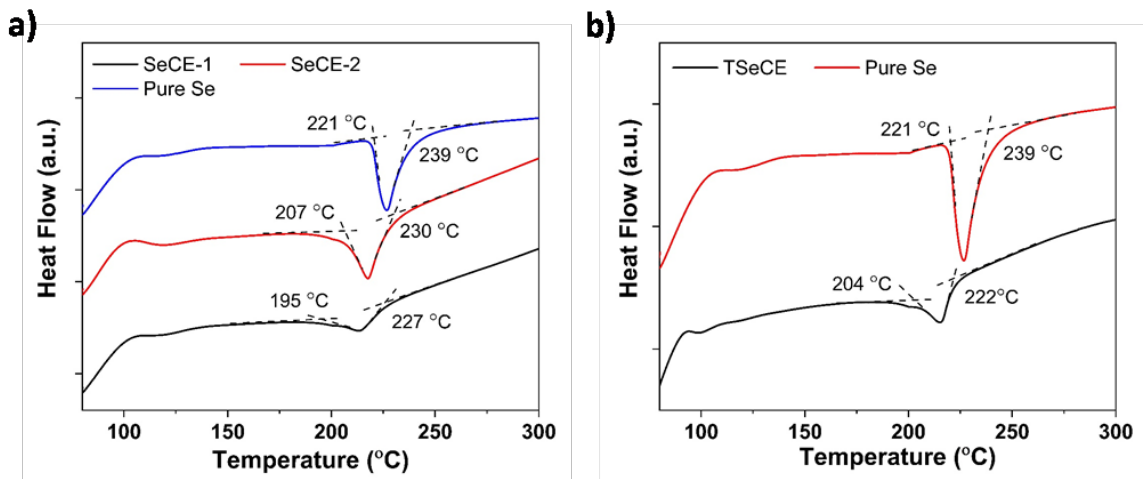


Figure 5.5. DSC plots for (a) SeCE-1, SeCE-2 and pure Se comparisons and (b) TSeCE and pure Se comparisons, respectively.

In addition, the DSC spectra in **Figure 5.5** show that the pure selenium nanowires exhibit a narrow endothermic peak at 221-239 °C. The Se has a melting point at 221 °C, which highly matches the endothermal area in the DSC plot. The endothermic peak is attributed to the melting process. The DSC spectra for the first set of the composite electrodes shows that the melting points decrease with decreasing selenium loadings. It has to be noted that pure carbon nanotubes start losing weight at around 450 °C in the TGA plot of **Figure 5.4**. Therefore, the carbon nanotubes have a much higher melting point than selenium. However, with more content of carbon nanotubes and less selenium, the endothermic peaks shift to lower melting points. The reason could be the captured and interwoven selenium nanowires by carbon nanotubes matrix leading to well contact with air. Instead of the pure selenium, the air flow covers the selenium bulks surface resulting in equilibrium reactions. The carbon matrix provides pores and spaces for air flow to increase the reaction speed, which results in decreased melting points. The TSeCE also shows a lower melting point than pure selenium. Overall, the melting points of the composite cathodes are in the order of SeCE-1 (195 °C) < TSeCE (204 °C) < SeCE-2 (207 °C) < selenium nanowires (221 °C). TSeCE has a similar melting point to SeCE-2 due to that they have the similar selenium mass loading percentage. The SeCE-1 has the lowest loading, in which the carbon matrix provides that most efficient pores for selenium being burned.

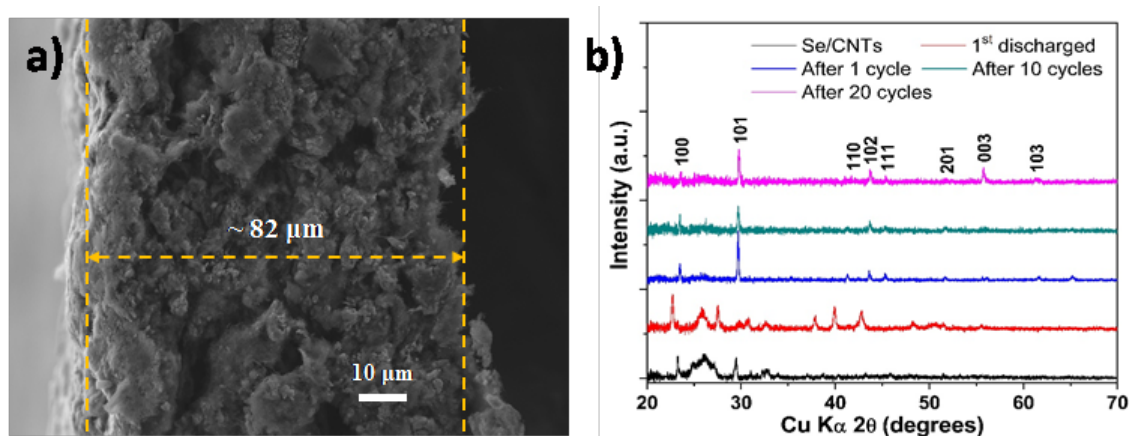


Figure 5.6. (a) Cross-section SEM image of the initial SeCE-2, (b) XRD patterns of the composite electrode at different states of cycling.

The cross-section morphology of the initial SeCE-2 cathode is shown in the SEM image in **Figure 5.6a**. The thickness of the SeCE-2 cathode is approximately 82 μm . The selenium nanowires are well covered and stored by interweaving with CNTs. Chemical transformations are tracked using XRD patterns, as shown in **Figure 5.6b**. The synthesized composite cathode shows two major peaks of the (100) and (101) planes and peaks of the (102) and (201) planes with low intensities. Upon discharge, new peaks at 2θ of 23° , 28° and between $37\text{--}43^\circ$ reveal the formation of Li_2Se . Upon charging, the selenium peaks reappear having higher intensities, especially the peaks of the (101) and (102) planes, which indicates a change in particles size and crystallinity upon cycling. After repeated cycling, major crystalline peaks of the (101), (102) and (003) planes of selenium appear. The repeated formed selenium shows good reversibility of the selenium during cycling.

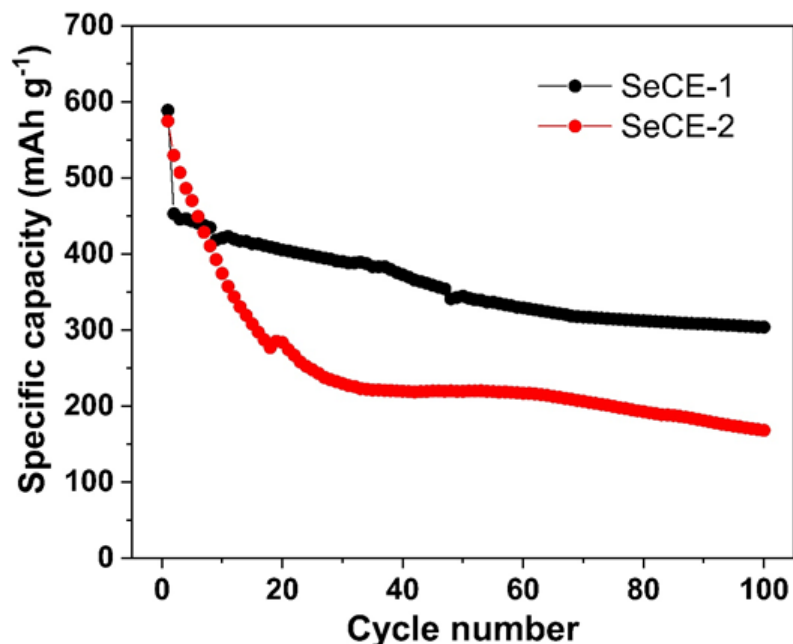


Figure 5.7. Cycling performance of SeCE-1 and SeCE-2 at 1C rate.

The cycling performance of SeCE-1 and SeCE-2 at 1C rate is shown in **Figure 5.7**. SeCE-1 has an initial discharge capacity of 589 mAh g⁻¹, capacity retention of 390 mAh g⁻¹ after 30 cycles and end capacity of 304 mAh g⁻¹ after 100 cycles. On the other hand, SeCE-2 has an initial discharge capacity of 575 mAh g⁻¹, capacity retention of 229 mAh g⁻¹ after 30 cycles and end capacity of 168 mAh g⁻¹ after 100 cycles. Both SeCE-1 and SeCE-2 have continuous capacity fading in the first 30 cycles. Especially, SeCE-2 has a more gross capacity fading in the first 30 cycles. This is due to the up to 61% high selenium loading in the composite electrode. The SeCE-1 has a relatively stable cycling performance for over 100 cycles and higher capacity retention than SeCE-2 due to its low selenium loading. Overall, both SeCE-1 and SeCE-2 do not show promising stable and long cycling performance over prolonged cycling.

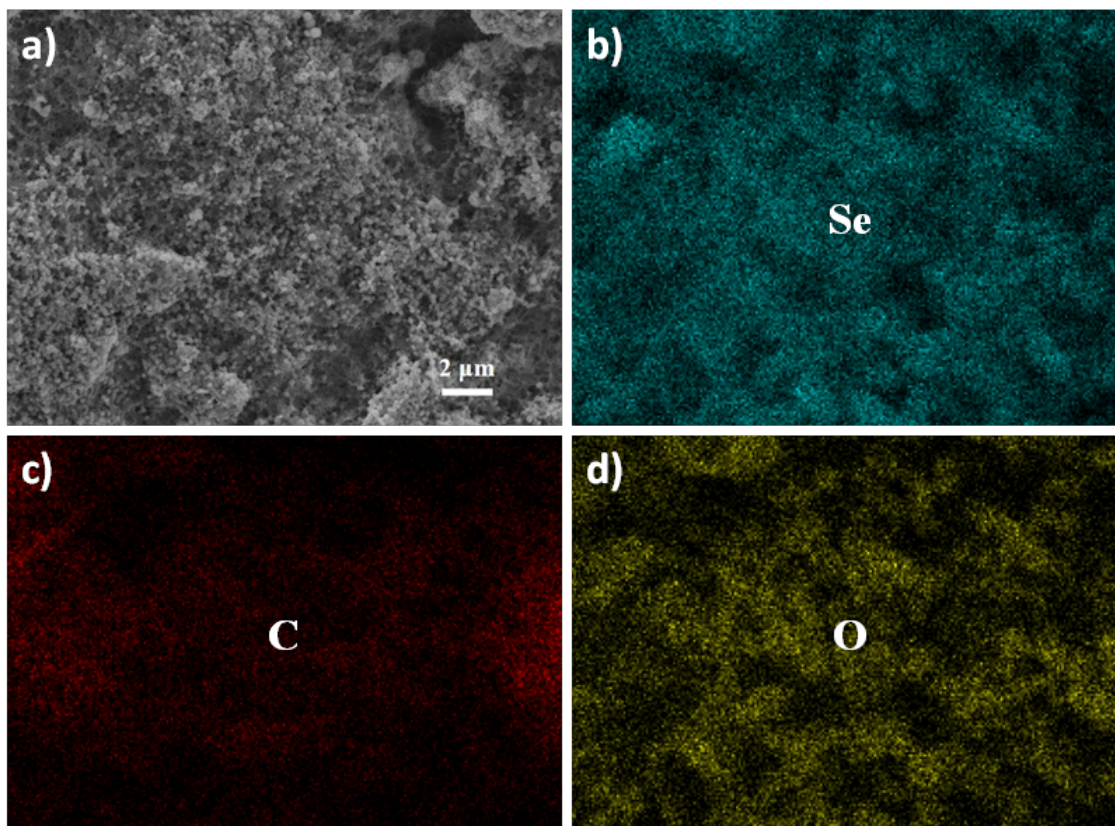


Figure 5.8. (a) Surface SEM image of SeCE-2 at discharged state, (b-d) EDS scan for selenium, carbon and oxygen, respectively.

To evaluate the reasons causing the capacity fade, SEM was used to characterize the morphological changes after discharge and charge. The low magnified SEM image and elemental mappings of selenium, carbon and oxygen at electrode surface are shown in **Figure 5.8**, which reveal the distribution of Li_2Se as nanometer-sized particles in the CNT network structure. The selenium element is from the Li_2Se , carbon is from the CNTs and the lithium salt. And the oxygen is obtained from the lithium salt only. It can be seen in both selenium mapping and oxygen mapping that the selenium is well covered with the lithium salt being held by the CNTs. Numerous nano-sized particles can be observed on the surface of the discharged composite electrode. In addition, it can be seen that the density of the formed Li_2Se is much higher than the initial selenium density in the composite electrode. The hypothesis is the

migration of the polyselenides during discharge deciding the final formation position of the discharge products, which needs to be further confirmed.

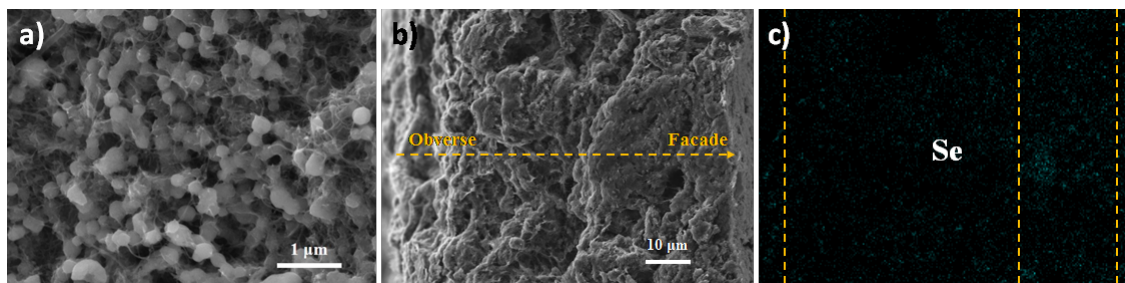


Figure 5.9. (a) Surface SEM image, (b) cross-section SEM image and (c) EDS showing selenium of the SeCE-2 at the discharged state.

The SEM image of the discharged electrode in **Figure 5.9a** shows the magnified surface morphology, at which the discharge product of Li_2Se is not in nanowire structure. Instead, the selenium nanowires break into parts upon discharge, and the formed Li_2Se are nanometer-sized particles stored in the porous CNT network. This is due to the selenium nanowires will form soluble polyselenides as intermediates during discharge. Upon discharge, the selenium nanowires undergo a solid-liquid phase transformation to form lithium polyselenides, which are soluble in the electrolyte. The continuous reduction leads a liquid-solid phase transformation to form insoluble Li_2Se which are in the particle format. **Figure 5.9b** shows the cross-section of the discharged electrode, at which the Li_2Se is uniformly stored in the CNTs pores. The elemental mapping of selenium at the cross-section in **Figure 5.9c** shows that Li_2Se mainly precipitates on the facade side of the electrode in contact with the separator upon discharge. The selenium density within approximate 30% thickness of the facial side is visually higher than the density in the deep electrode, which means most CNTs are no longer able to store active material. If we consider the high loading area has 2 times selenium of that in the low loading area, the estimated mass loading of the selenium at the facade side can be up to 78%. The suddenly increased loading would result in difficulty in the conversion reactions between solid phase (Li_2Se) and

liquid phase (polyselenides). The possible reason for the non-uniform distribution of Li_2Se in the composite electrode upon discharge could be the migration of anions of polyselenides to the separator side. During discharge, a lithium ion concentration gradient from lithium foil electrode (high) to the selenium electrode (low) is generated. To maintain charge neutrality, the anions of polyselenides tends to diffuse to the separator side, thereby generating a concentration gradient of polyselenides. The higher concentration of polyselenides on the separator side will result in more Li_2Se precipitation.

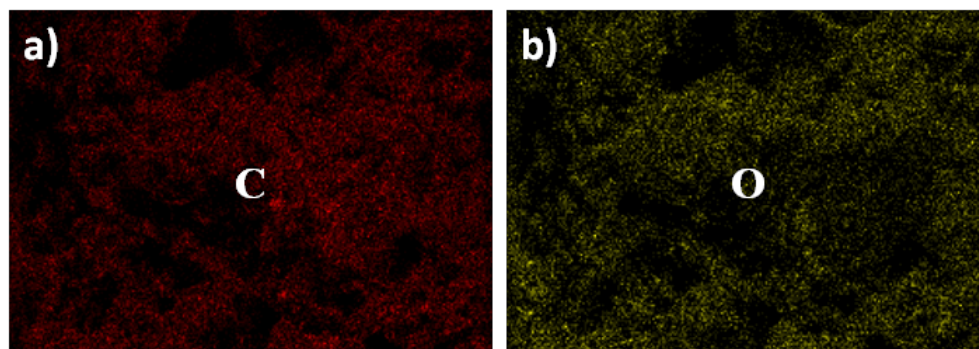


Figure 5.10. EDS scan for (a) carbon and (b) oxygen at cross-section of the SeCE-2 at the discharged state.

The carbon mapping and the oxygen mapping of the cross section are shown in **Figure 5.10**, which are mainly captured from CNTs and lithium salt. The oxygen mapping shows the uniform distribution of the lithium salt, as well as the carbon mapping. The uniform distribution of oxygen indicate that the lithium salt will not immigrate during discharge reactions, which only provides that lithium cations transport instead of immigrating with the polyselenides. Carbon is mainly from the CNTs, which provides the whole structure of the electrode and the maintains the stable structural distribution.

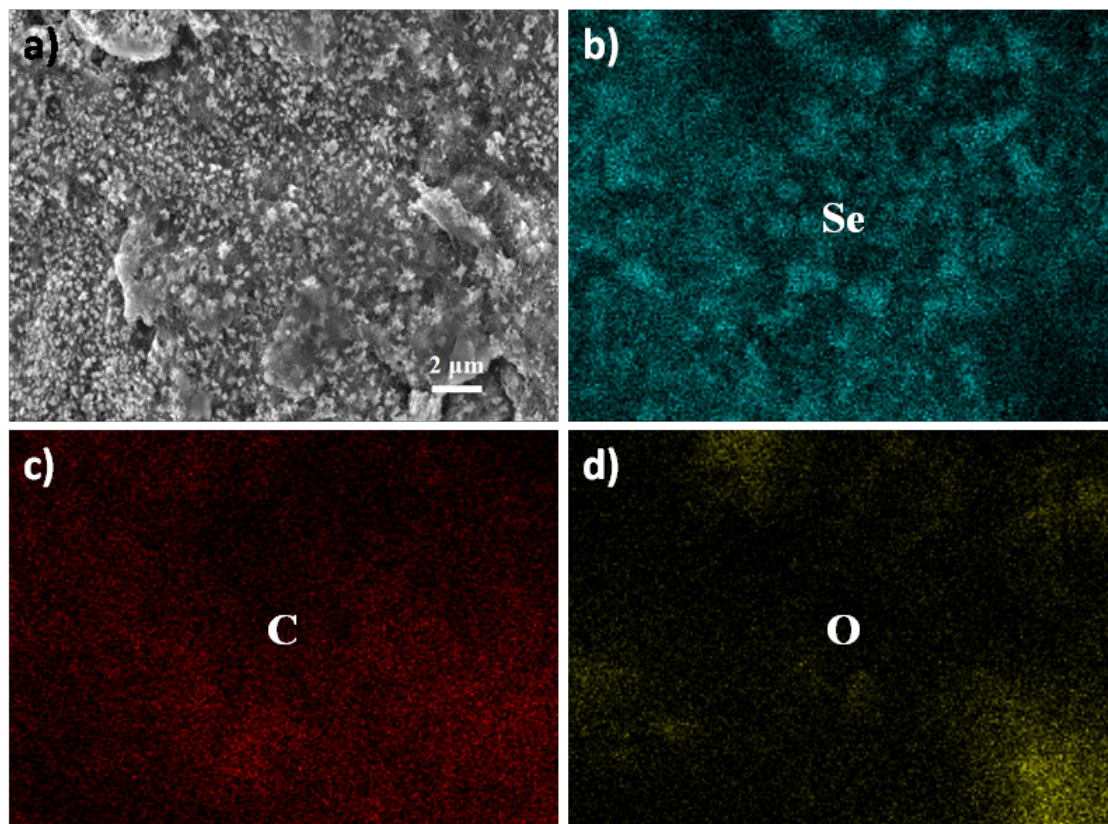


Figure 5.11. (a) Surface SEM image of SeCE-2 at charged state, (b-d) EDS scan for selenium, carbon and oxygen, respectively.

The recharged composite electrode was also reviewed by SEM and EDS. **Figure 5.11** shows the low magnified SEM image and elemental mappings of selenium, carbon and oxygen, in which the distributions of selenium and lithium salt are demonstrated. The reversible selenium is formed in particle format instead of converting to nanowires. The selenium mapping also shows clear particle format.

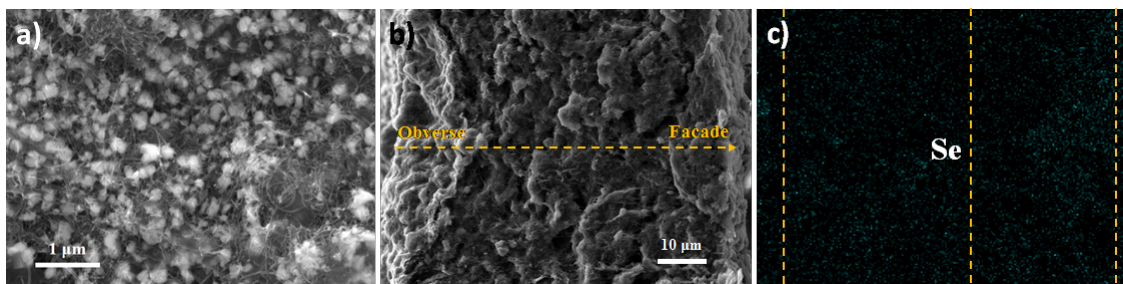


Figure 5.12. (a) Surface SEM image, (b) cross-section SEM image and (c) EDS showing selenium of the SeCE-2 at the charged state.

In the charged state, the selenium nanowires are not regenerated, but also in nanometer-sized particle format, as shown in the magnified SEM images in **Figure 5.12a**. The reversible solid-liquid-solid transformation happens during charging, which results in the formation of nanometer-sized selenium particles after the 1st cycle. As shown in the SEM image and selenium mapping in **Figure 5.11b** and **c**, much selenium is restored back to the obverse side of the CNT paper, but the selenium concentration gradient still slightly exists. Unlike the discharge product of Li_2Se , the converted selenium is not in high gradient different in the CNTs. This means the polyselenides intermediates immigrate towards the obverse side and are restored by the CNTs matrix. By carefully measure the density gradient at the cross-section, approximately half of the composite electrode has a higher selenium distribution.

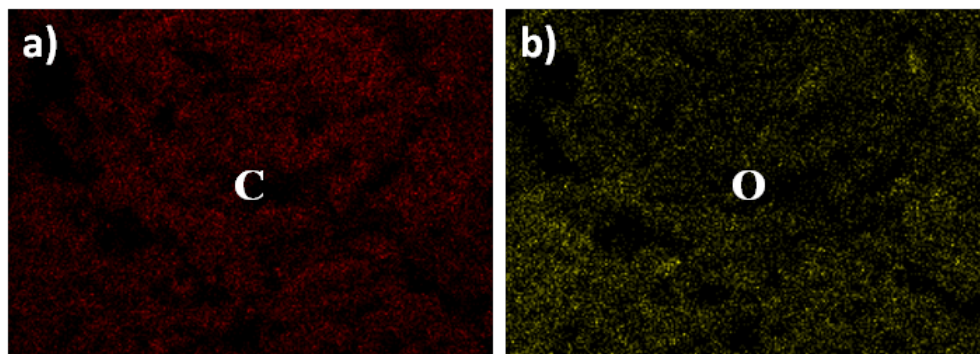


Figure 5.13. EDS scan for (a) carbon and (b) oxygen at cross-section of the SeCE-2 at charged state.

The carbon mapping and the oxygen mapping captured from CNTs and lithium salt at the cross-section are shown in **Figure 5.13**. This phenomenon can also be explained by charge neutrality. During charge, a lithium ion concentration gradient from the selenium electrode (high) to lithium foil electrode (low) is generated, which is opposite to the discharge process. To maintain charge neutrality, the anions of polyselenides tends to diffuse to the selenium electrode, thereby decreasing the concentration gradient of polyselenides. Therefore, the converted selenium is in more uniform distribution than Li_2Se due to the preferred migration back to the carbon matrix. However, the converted selenium distribution is not perfectly uniform, which could be due to the high gradient difference in Li_2Se distribution. The highly increased surface loading causes the difficulty for Li_2Se being recharged and reduce the utilization of the active materials, herein causing continuous capacity fades during prolonged cycling.

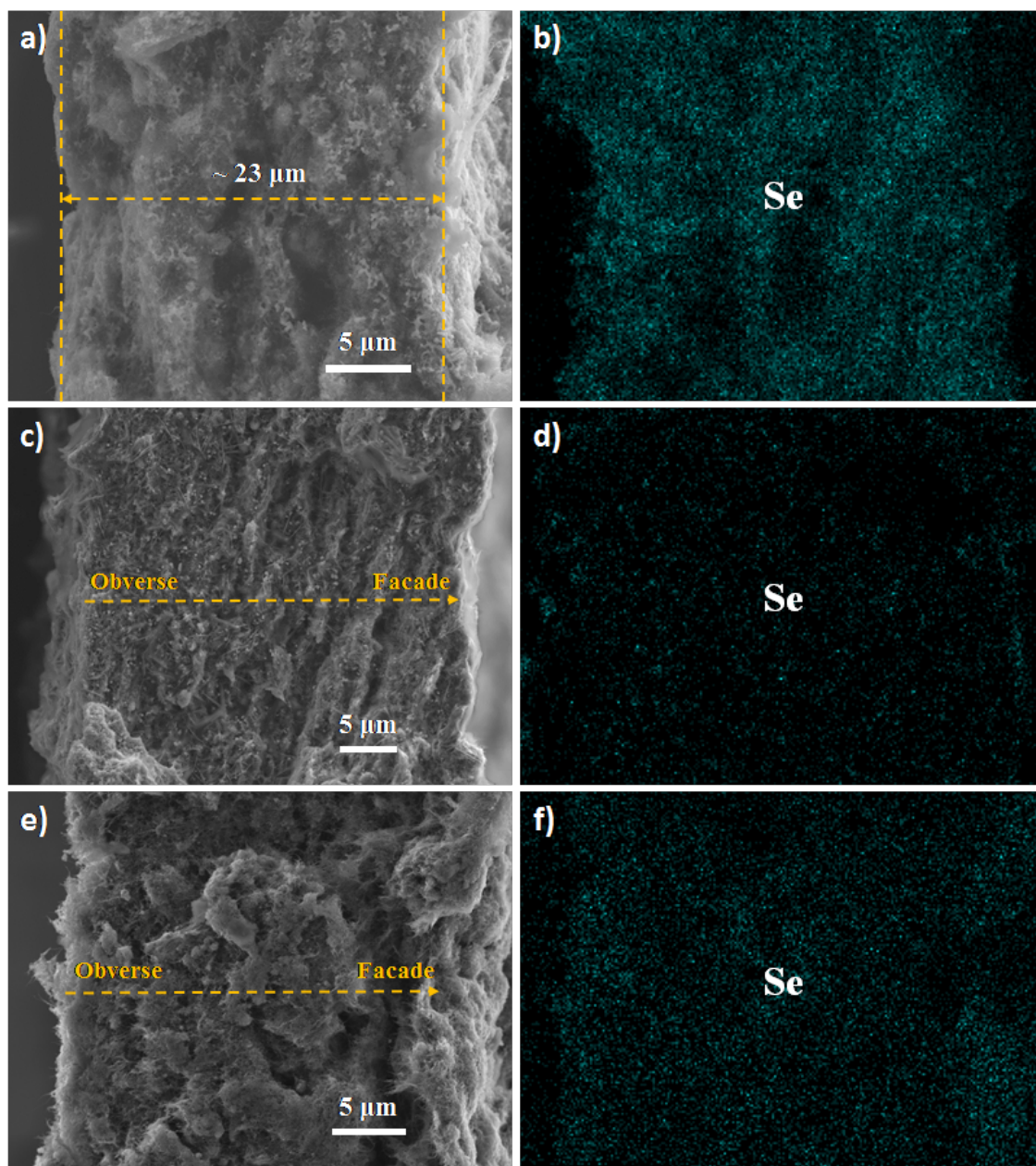


Figure 5.14. (a) Cross-section SEM image, (b) EDS showing selenium of the initial TSeCE, (c) cross-section SEM image, (d) EDS showing selenium of the TSeCE at the discharged state, (e) cross-section SEM image and (f) EDS showing selenium of the TSeCE at the charged state.

To avoid this uneven distribution of selenium during redox process, the thickness of the composite electrode is highly decreased for TSeCE, while the same material loading in the composite electrode is maintained. We hypothesize that the concentration gradient of polyselenides can be decreased in the thinner selenium electrode and the issue of uneven distribution of selenium can be addressed. The loading result of TSeCE is shown in the TGA plot of **Figure 5.4c**. The SEM image of the cross section of TSeCE is shown in **Figure 5.14a**. The thickness is approximately 23 μm measured by SEM. This thickness has been already about 1/4 of the original thickness, which is a huge decrease in electrode thickness. In addition, selenium nanowires are clearly observed in the CNTs in this cross-section SEM image. From the TGA plots, we can confirm that the mass percentages of selenium for TSeCE and SeCE-2 are almost the same. The initial selenium nanowires are uniformly distributed in the CNTs, which is also demonstrated by the selenium mapping in **Figure 5.14b**. The selenium mapping shows a well uniform distribution of the selenium in the composite electrode. For easy comparisons, the cross section of the composite electrode after discharge and charge are shown in the same figure. The discharged electrode is firstly investigated to understand the morphological changes. The SEM image of the cross section after discharge in **Figure 5.14c** shows that the formed Li_2Se particles are uniformly distributed in the CNTs network. The Li_2Se particles are well stored in the CNTs pores and spaces. The elemental distributions were scanned by EDS, in which the selenium mapping shows uniform distribution of selenium in the CNT network (**Figure 5.14d**).

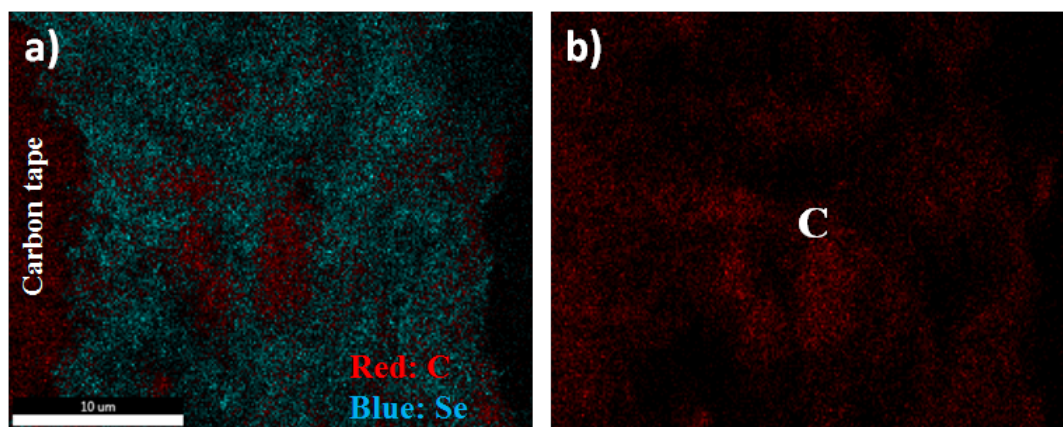


Figure 5.15. EDS scan for (a) overlapping and (b) carbon at cross-section of the TSeCE before cycling.

The overlap mapping and carbon mapping are shown in **Figure 5.15**. The carbon is obtained from the CNTs and lithium salts. The selenium distribution shows that the Li_2Se is well stored by the CNTs network. Unlike the SeCE-2, it does not show a great gradient distribution of selenium. In the selenium mapping in **Figure 5.14d** and overall mapping in **Figure 5.15a**, it can be seen that the selenium densities are the same at both observe and faade. This evidence supports that the migration of polyselenides can be minimized during discharge when decreasing the electrode to very thin thickness. Although the charge neutrality trends to lead the polyselenides anions diffusing towards the separator side, the highly decreased thickness helps increasing the contact of the selenium at deep positions with liquid electrolyte, herein makes the diffusion in electrolyte much easier without having a heavy anions migration.

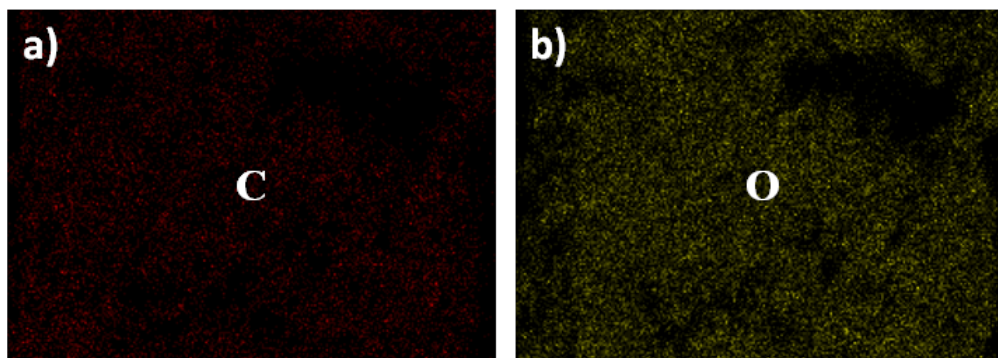


Figure 5.16. EDS scan for (a) carbon and (b) oxygen at cross-section of the TSeCE at discharged state.

Upon charging, both the SEM image and the selenium mapping in **Figure 5.14e** and **f** show a uniform distribution of the reversed selenium in the composite electrode. After charge, the reversed selenium is well stored back to the CNTs network shown in the SEM image. The selenium mapping shows no visible gradient for the selenium distribution. As expected, the highly reduced thickness helps the formed Li_2Se particles to be oxidized and converted to selenium and restored. The carbon mapping and oxygen mapping for discharged state and charged state are shown in **Figure 5.16** and **Figure 5.17**, respectively. The carbon element is scanned from CNTs and lithium salts, and the oxygen element is obtained from the lithium salts only. Overall, in both discharged and charged states, no obvious selenium concentration gradient is observed for this thinner electrode. After redox reactions, the products are still uniformly distributed in the composite electrode. The maintained contacts between selenium and CNTs provide a possibility for better performance during the repeated conversion reactions.

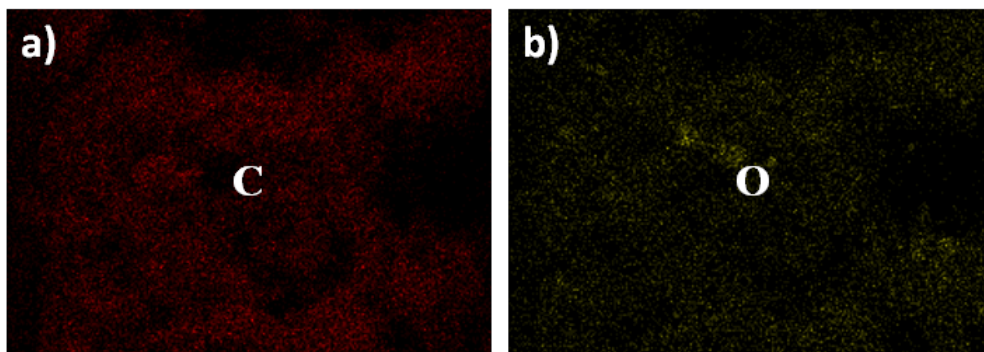


Figure 5.17. EDS scan for (a) carbon and (b) oxygen at cross-section of the TSeCE at charged state.

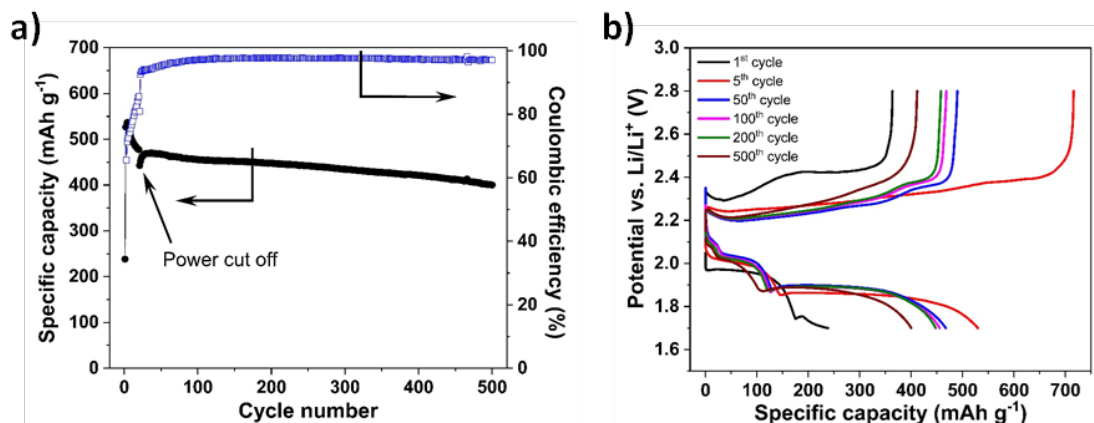


Figure 5.18. (a) Cycling performance and (b) voltage profile of the TSeCE at 1C rate in rechargeable lithium batteries.

The TSeCE electrode was cycled at 1C to test its cycling performance. As shown in **Figure 5.18a**, although the initial discharge specific capacity is 238 mAh g⁻¹, it increases to a specific capacity of 537 mAh g⁻¹ in the second cycle, which is corresponding to about 79% of the theoretical capacity. After that, the specific capacity continuously fades to 477 mAh g⁻¹ in the first 20 cycles and retains 401 mAh g⁻¹ over 500 cycles, which is corresponding to 0.03% capacity fading per cycle. The capacity fading in the first several cycles could be due to the shuttle effect of the polyselenides.

It takes few cycles for LiNO_3 to be reduced and form a stable passivation layer on the lithium metal electrode. The Coulombic efficiency (CE) is 65% initially, then keeps increasing to 93% in the following cycle. With the stable cycling, the CE consistently remains over 98% throughout 500 cycles. This indicates the active material loss is minimal during the stable cycling. The voltage profile for the cell is shown in **Figure 5.18b**. Starting from the open-circuit voltage (OCV), the 1st discharge does not show two clear plateaus due to the incomplete discharge, and the charging plateaus are longer because of the polyselenides shuttle effect resulting in low CEs and longer charging process. In the following cycles, the first discharge plateau occurs at 2.04 V followed by further reduction plateau at 1.9 V. The charging step has two oxidation plateaus at 2.2 V and 2.37 V.

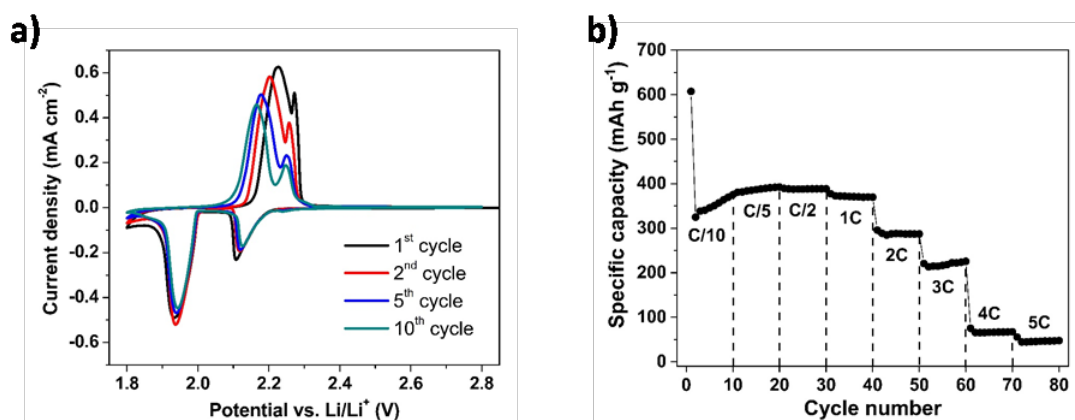


Figure 5.19. (a) Cyclic voltammogram and (b) rate performance of the TSeCE in rechargeable lithium batteries.

Figure 5.19a shows the cyclic voltammetry (CV) profiles of the composite cathode in the voltage range of 1.8-2.8 V with a sweep rate of 0.02 mV s⁻¹. In the initial cycle, the reduction peaks are shown at 2.11 and 1.94 V, corresponding to the reduction from Se to polyselenides and the reduction from polyselenides to Li_2Se . The subsequent anodic scan exhibited two sharp anodic peaks at 2.22 and 2.27 V, corresponding to the reversible conversion from Li_2Se to polyselenides, and then to

elemental selenium, respectively. The cathodic scan of the CV profiles remained unchanged after the first cycle. The anodic peaks after the 1st cycle move to slightly lower potential, in which the over potential is also decreased. The CV profiles indicate an excellent reversibility of the selenium nanowires in the composite cathode. The composite electrode is also tested under variable C-rates, as shown in **Figure 5.19b**. The composite electrode shows an initial specific capacity of 608 mAh g⁻¹ at C/10 and 380 mAh g⁻¹ at C/5. The cell exhibits stable cycling performance with a specific capacity of 392 mAh g⁻¹ at C/2, 377 mAh g⁻¹ at 1C, 295 mAh g⁻¹ at 2C and 220 mAh g⁻¹ at 3C, not having much capacity fades. When the cycling is further raised to higher C-rates, the cell retains the capacity of 75 mAh g⁻¹ at 4C and 55 mAh g⁻¹ at 5C.

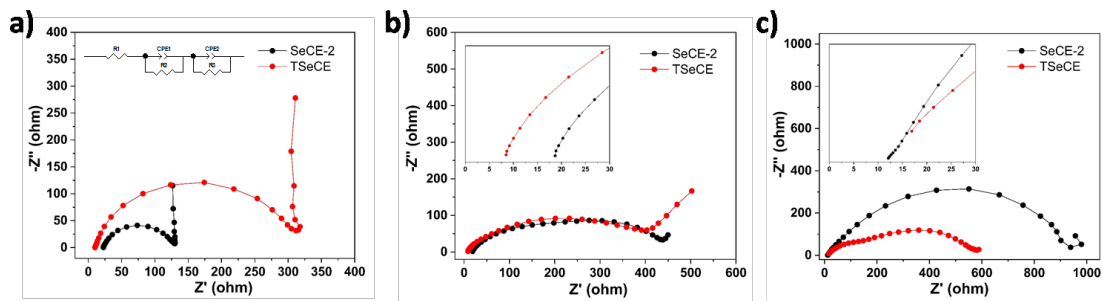


Figure 5.20. Nyquist plots of the SeCE-2 and TSeCE (a) before cycling, (b) after discharge and (c) after charge with inset pictures showing the intercepts in the high-frequency regions.

Figure 5.20 compares the Nyquist plots of SeCE-2 and TSeCE initially, after the first discharge, and after the first charge, respectively. The intercepts of Nyquist plots in the high-frequency regions are 22.6 ohms for SeCE-2 and 10.2 ohms for TSeCE, which attribute to the bulk resistance of the liquid electrolyte. Both plots display one semicircle which are assigned to the charge transfer resistance (R_{ct}). The semicircle of the TSeCE is initially larger than that of SeCE-2 in the high-medium frequency regions, for which the TSeCE initially has a higher charge transfer resistance than that of SeCE-2. The inset picture shows the equivalent circuit. In the Nyquist plots after

discharge (**Figure 5.20b**), the intercepts of Nyquist plots are 18.7 ohms for SeCE-2 and 8.5 ohms for TSeCE. In addition, the charge transfer resistance of SeCE-2 is increased almost 3 times to approximately 460 ohms, while the charge transfer resistance of TSeCE is increased only 40% to about 460 ohms. As shown in **Figure 5.20c**, the intercepts are nearly the same after charging. But the charge transfer resistance of SeCE-2 is further increased to 940 ohms, while the charge transfer resistance of TSeCE is about 570 ohms. The impedance results show that the thinner electrode has relatively stable charge transfer resistance while the charge transfer resistance of thicker electrode keeps increasing. The unstable charge transfer resistance could be caused by the local high selenium loading due to the non-uniform distribution of selenium during repeated cycles.

5.5 Conclusion

In this study, a binder-free selenium nanowires/CNT composite electrode was synthesized by using a facile chemical method. The selenium loading and thickness of the composite electrode are adjustable by regulating the amounts of reactants. The SEM and EDS results show that the thickness of the composite electrode has a critical impact on distribution of selenium in the electrode during repeated cycles, and then affect the electrochemical performance of the electrode. By decreasing the thickness to 23 μm , at selenium content of 60% in the entire electrode, the binder-free Se/CNT electrode exhibits high discharge capacity of 537 mAh g^{-1} (79% of the theoretical capacity) at 1C and long cycling stability with a small capacity fading of 0.03% per cycle over 500 cycles at 1C. This study reveals that the uniformity of the distribution of selenium in the electrode not only in the original state but also during the repeated cycles is critical to the cycling performance. Thin electrodes result in uniform distribution of selenium in both discharged and charged states, leading to the promising cycle life of the binder-free Se/CNT electrode.

6. SUPPRESSION OF SHUTTLING IN LI-S BATTERIES USING POLYSULFIDE-SELECTIVE MOLECULAR RECEPTORS

6.1 Abstract

Sulfur (S) is considered a promising cathode material for the next generation high energy density rechargeable lithium batteries. However, several obstacles still exist for the practical application of lithium-sulfur batteries, such as the shuttling of soluble polysulfides during charging leading to severe capacity fading and low Coulombic efficiency. To suppress the shuttle effect, we converted standard battery separators into chemically-selective membranes by coating a layer of anion-binding receptors called cyanostar macrocycles. Compared to previous approaches using the surface absorption of polysulfides, cyanostar provides an absorption mechanism on molecule-to-molecule level and has the potential for more effective polysulfides traps and higher energy density. Integration of cyanostar into the separator is shown to improve Coulombic efficiency over test cells from 54 to 85%. In comparison with the control cells, cyanostar-enhanced batteries are also capable of fully charging and reducing the capacity fading from 0.51 to 0.36%. These results demonstrate the utility of this novel and adaptable method as its ability to improve the performance of sulfur-based battery chemistries.

6.2 Introduction

In the past two decades, lithium-ion batteries (LIBs) have been extensively applied in portable electronic devices as well as in electric vehicles (EVs) on account of their high energy density compared to other battery chemistries. However, the tran-

sition metal oxide cathode materials used in conventional LIBs that rely depending on lithium intercalation reactions have reached their maximum capacity and energy density limits. This situation makes them an unsatisfactory long term solution for power storage. The unmet need for batteries with high energy densities has inspired exploration of new types of high-capacity cathode materials. One solution is sulfur cathodes, which have a high theoretical specific capacity of 1672 mAh g^{-1} . In addition, sulfur has several secondary benefits, such as low cost, high abundance and being environmentally benign. However, these capacity benefits cannot currently be utilized on account of several technical difficulties involving sulfur cathodes. The primary challenge is an ensemble of effects resulting from the so called “shuttle effect”. Therein, soluble polysulfides Li_2S_x ($4 \leq x \leq 8$) that are generated in the battery during discharge and charging readily migrate between the sulfur cathode and lithium anode resulting in parasitic reactions during the subsequent charging process [123, 124]. The consequences of this shuttling include low Coulombic efficiency (CE), continuous loss of sulfur, and production of insoluble agglomerates over repeated cycling [125].

To alleviate the shuttle effects, several strategies have been developed, such as use of carbon interlayers as physical barriers and development of advanced microporous carbon hosts for improved electrochemical performance. Alternatively, surface chemisorption of the polysulfide species is also a promising path to alleviate the shuttle effect. Managing the movement of ions underlies the performance enhancements of all next-generation lithium battery chemistries, particularly lithium-sulfur batteries [126]. Previous successes have pursued materials strategies with the design of superior cathodes composed of metal oxides or metal-organic framework materials [127]. For instance, Yang et al. applied nanoscopic inorganic hosts, like hierarchical titanium dioxide spheres with strong polysulfide binding to achieve improved electrochemical performance [128]. Al Salem et al. used nanoscopic transition metal carbides for adsorbing polysulfide species to enhance polysulfide cycling processes [129]. In such systems, the adsorption of polysulfides is restricted to the surface of the particles,

leading to the anion trapping efficiency being a function of surface area. These metal oxide-based materials noticeably increase the systems total mass, further decreasing the maximum energy density. Therefore, strategies that circumvent the dependence on adsorption mechanisms have the potential to boost battery performance.

Herein, we leverage an advanced macrocyclic receptor called cyanostar (CS) [130] to bind polysulfide species (**Figure 6.1**) to minimize the shuttling effect. Use of anion receptors provides a molecule-to-molecule adsorption mechanism for more effective polysulfide trapping. Mass spectrometry and UV-Vis titration experiments were used to confirm host-guest binding of polysulfide species inside cyanostar receptors. The cyanostar was then applied as a coating on a commercial separator to act as a receptor layer. The electrochemical behavior of the resulting batteries was studied and then correlated to changes in separators morphology to demonstrate the effectiveness of the cyanostar in improving battery performance. The electrochemical results verify substantial suppression of the polysulfide shuttling leading to enhancements in cycling stability and battery capacity. This finding lays the groundwork for a new mechanism to improve the performance of Li-S batteries using supramolecular design principles.

6.3 Experimental

6.3.1 Materials and Instruments

All materials were used as received and listed in table 6.1. All instruments used were listed in table 6.2.

Table 6.1. Materials

Chemical Name	Purity	Provider
Cyanostar (CS)	Synthesized	N/A
Lithium bis(tri-fluoromethanesulfonimide) (LiTFSI, LiN(CF ₃ SO ₂) ₂)	99%	Acros Organics
1,2-dimethoxyethane (DME)	99.5%	Sigma Aldrich
1,3-dioxolane (DOL)	99.8%	Sigma Aldrich
Sulfur (S)	99.5%	Alfa Aesar
Lithium sulfide (Li ₂ S)	99.98%, trace metals basis	Sigma Aldrich
Carbon disulfide (CS ₂)	Certified ACS	Fisher Scientific
Polyvinylidene fluoride (PVdF)	N/A	Kureha Battery Materials Japan Co., Ltd.
1-methyl-2-pyrrolidone (NMP)	99.5%	Sigma Aldrich

Table 6.2. Instruments

Instrument	Provider
Mass Spectrometry	Thermo MAT-95XL magnetic sector instrument
Battery cyler	Arbin BT2000
VSP potentiostat	BioLogic
Vacuum Oven	Isotemp 281A
Glove box	MBraun
Scanning electron microscopy (SEM)	JEOL JSM-7800F

6.3.2 Preparation of electrolyte and polysulfide catholyte

The electrolyte is composed of 1.0 M LiTFSI in a mixture solvent of DME and DOL (1:1 v/v). The lithium polysulfide (Li_2S_6) catholyte was prepared by adding stoichiometric amounts of S and Li_2S in the prepared electrolyte by magnetic stirring over 48 hours at room temperature to render 0.25 M Li_2S_6 catholyte.

6.3.3 Preparation of S electrodes

The elemental sulfur solution was prepared by dissolving sulfur in CS_2 to form 3.125 M solution. Commercial binder-free carbon nanotube paper called buckypaper (NanoTechLabs Composites, Inc) was used as the current collector in this study. The carbon paper was cut into 0.97 cm^2 discs ($D = 11 \text{ mm}$, about 1.9 mg each) and dried at 100°C for 24 hours in a vacuum oven before use. Then $10 \mu\text{L}$ prepared sulfur solution was added into the dried carbon paper in a petri dish. Then the carbon paper electrode was dried in a vacuum oven at room temperature for 12 hours. The mass of sulfur on carbon paper is 1.0 mg corresponding to a weight percent of 34%. Another three sulfur solutions were prepared by dissolving elemental sulfur in CS_2 to render 1.5625 M, 4.6875 M and 6.25 M sulfur solutions, respectively. Another three sets of sulfur cathodes with different sulfur mass loadings were prepared following the same procedure. The yielded mass of sulfur on carbon paper are 0.5 mg, 1.5 mg and 2.0 mg, which are corresponding to a weight percent of 21%, 44% and 51%, respectively.

6.3.4 Preparation of CS-coated separator and control compound-coated separators

The CS-coated separator was fabricated by surface coating the cyanostar on one side of a commercial polypropylene separator (Celgard 2400). The cyanostar slurry was prepared by mixing the cyanostar and PVdF in NMP solvent with the ratio

of 8:2 (CS: PVdF) in a mortar for fully mixing. The cyanostar slurry was coated onto the Celgard 2400 using a doctor blade and then dried at 40 °C for 24 h in a vacuum oven. The CS-coated separator was then cut into 2.83 cm² circular disks (D = 19 mm, Celgard 2400 mass is 4.0 mg each, cyanostar mass is about 5.0-6.0 mg (1.77-2.12 mg cm⁻²). The control compounds (pure PVdF, curcubit[6]uril and β -cyclodextrin) coated separators were fabricated following the same casting procedure. For pure PVdF-coated separator, 12 wt.% PVdF in NMP solution was used. The PVdF on separator is about 4.0-4.6 mg (1.41-1.63 mg cm⁻²) each after dryness. The curcubit[6]uril and β -cyclodextrin on separator are approximately 5.0 mg each after dryness.

6.3.5 Linear voltage sweep measurement

The linear voltage sweep (LVS) measurement was tested in the same method reported by our group before. The experimental cell was sealed in a custom Swagelok cell in an Ar-filled glove box. The cell consists of a piece of lithium metal as the reference and counter electrode, a piece of the prepared carbon paper which was used as a reservoir for holding 40 μ L of polysulfide catholyte added to it, and a stainless steel current collector as the working electrode. A Celgard 2400 separator was placed in between the polysulfide-filled carbon paper and stainless steel current collector. The cell was connected to a BioLogic VSP potentiostat and the LVS was carried out from open circuit voltage (OCV) of the cell to 4.5 V at a scan rate of 1 mV s⁻¹. The PVdF- and CS-coated separator were test following the same procedure by placing the PVdF- and CS-coated separator in between the polysulfide-filled carbon paper and the stainless steel current collector.

6.3.6 Cell fabrication and electrochemical evaluation

CR2032 Coin cells were used and cells were fabricated in an Ar-filled glove box. First, 15 μ L electrolyte was added into the prepared carbon paper electrode. Then

a piece of Celgard 2400 separator was placed on the top of the electrode followed by adding 15 μL electrolyte on the separator. Finally, a piece of lithium metal and nickel foam as a spacer was placed on the separator. The cell was crimped and taken out of the glove box for electrochemical evaluation. While assembling cells using the PVdF-coated separator and CS-coated separator, they were followed by the same procedure.

Cells were galvanostatically cycled on an Arbin BT2000 battery cycler at C/10 rate ($1\text{C} = 1672 \text{ mA g}^{-1}$, based on the mass of material in the cells) and in voltage ranges of 1.5-2.8 V. To observe the shuttle effect in the control experiments and prevent the unlimited charge process, one more charge ending condition beyond voltage condition is set on the Arbin cycler, which is the charge capacity (charge process ends when the charge capacity reaches the theoretical capacity of the sulfur cathode in the cells, $1.0 \text{ mg S} = 1.672 \text{ mAh}$ theoretical charge capacity, based on the mass of material).

6.3.7 Characterizations

The morphological characterization of the CS-coated separators was conducted with a JEOL JSM-7800F field emission scanning electron microscopy (SEM). The cycled CS-coated separator samples were obtained by opening the cells in the glovebox. Then the separators were sealed in a sealed jar filled by Argon gas, and then transported to the SEM. The elemental mapping was performed with energy-dispersive X-ray spectroscopy (EDS) attached to the SEM at 7 kV to confirm the presence of sulfur and carbon in the separators.

6.4 Results and Discussion

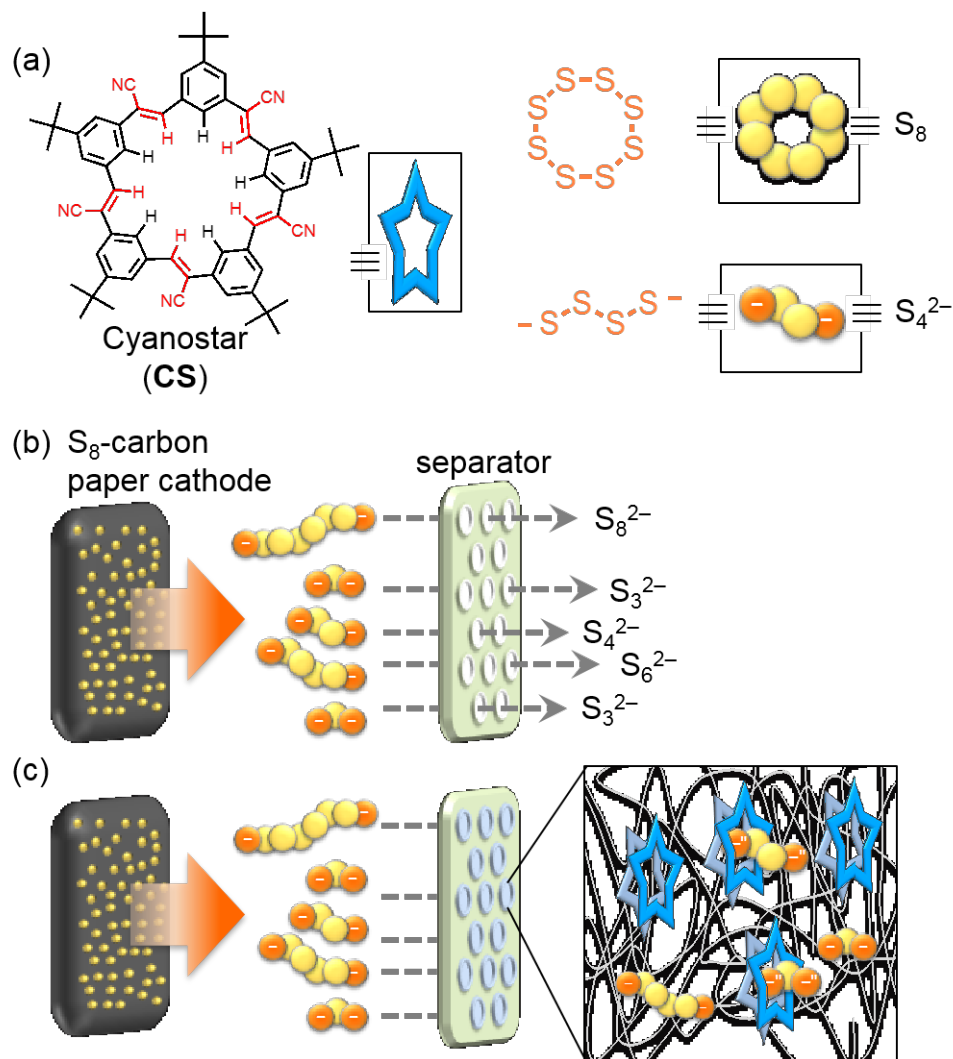


Figure 6.1. (a) Chemical structures of cyanostar, sulfur (S_8) and tetrasulfide dianion (S_4^{2-}). (b) scheme showing the diffusion of various polysulfides out of sulfur cathodes and through standard separators. (c) scheme showing the introduction of cyanostar into separator pores and its role in binding polysulfides to stop their shuttling over to the anode.

Our experimental strategy utilized a two-step approach to establish the mechanism and performance enhancements when using molecular receptors in Li-S batteries. We

first explore the host-guest chemistry of polysulfides and cyanostar, and then measure the performance improvements when cyanostar is used as a selective ionophoric layer on the separator, as shown in in **Figure 6.1**. The cyanostar has a fivefold symmetric macrocyclic structure, that forms π -stacked dimers in which the central pore defines an electropositive binding pocket for anions. Given the strong binding of the cyanostar dimer to bromide, ($\Delta G = -54 \text{ kJ mol}^{-2}$, 40% MeOH/ CH_2Cl_2) [130] which is of comparable size to the terminal sulfide in a polysulfide chain, we anticipated formation of polysulfide-cyanostar complexes in solution. We hypothesized that this solution-phase behavior could translate to performance improvements in the battery upon formation of an ionophoric layer. We expect soluble polysulfides generated during battery cycling would be captured by the membrane-bound layer of cyanostars to alleviate the migration of polysulfide species.

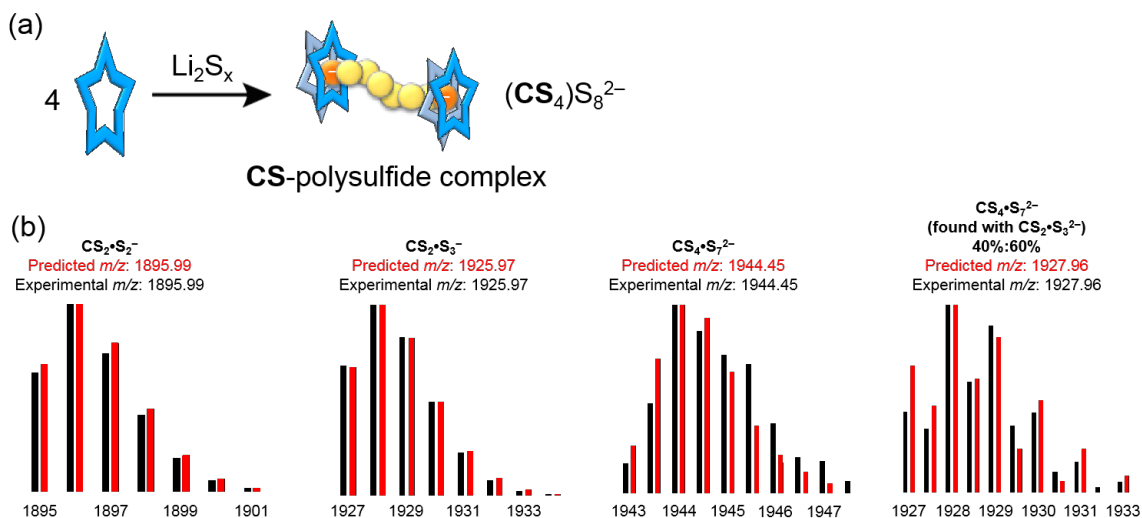


Figure 6.2. (a) Cartoon representation showing the host-guest association of polysulfides with cyanostar; only one possible inclusion complex is shown for simplicity, (b) isotopic splitting patterns observed in the ESI-MS titration compared with the predicted distribution.

Investigating the supramolecular chemistry of polysulfides was a first necessary step as no prior studies have examined their host-guest chemistry with anion recep-

tors. Cyanostar macrocycles typically form π -stacked sandwich complexes around monoanions but can also form triple stacks around dianions and tetramer stacks around higher-order polyanionic phosphate oligomers [131]. Based on these characteristic behaviors and the fact that polysulfides can partition into various polyatomic congeners, e.g., S_8^{2-} , S_7^{2-} , S_6^{2-} , S_4^{2-} , and S_2^{2-} (**Figure 6.1b**), we expected complexes could easily involve more than two macrocycles. In that case, the binding mechanisms for cyanostar-polysulfides are expected to involve π -stacked cyanostar dimers on each anionic end of the linear polysulfide species (**Figure 6.2a**).

Cyanostar-polysulfide association was characterized by the electrospray ionization mass spectrometry (ESI-MS) following methods used elsewhere for cyanostar complexes. Solutions of lithium polysulfide in tetrahydrofuran (THF) were prepared using standard procedures [132] yielding a yellow-brown solution populated by the dianionic octasulfide (S_8^{2-}) and heptasulfide (S_7^{2-}) salts as determined by ESI-MS (Supporting Information). The ~ 1 mM solutions of polysulfide were based on the concentration of the S_8 precursor at ~ 1 mM. Cyanostar (dissolved in THF) was added to the polysulfide at 0, 2, 4, and 8 equivalents. Presumably, 4 equivalents is stoichiometrically balanced to form π -stacked dimers with the two anionic ends of an octasulfur dianionic species, i.e., $S^- - (S_6) - S^-$. Each of these solutions had a distinctive color with the last 8:1 cyanostar-polysulfide sample notably having an intense blue color (*vide infra*, Supporting Information).

The host-guest complexes present in solution were analyzed by direct injection ESI-MS with the resulting spectra closely matching predicted mass to charge ratios for various assemblies (**Figure 6.2b**). Heptasulfides were observed in all solutions. A heptasulfide bound with four cyanostars, $(CS_4)S_7^{2-}$ was both the most commonly observed species, and the dominant species in all samples. A minor species, described as a complex involving five cyanostar macrocycles with heptasulfide, was also observed $(CS_5)S_7^{2-}$. Other species observed included hexasulfides bound to four cyanostars $(CS_4)S_6^{2-}$, a trisulfide radical bound to two cyanostars $(CS_2)S_3^{\bullet-}$ and disulfide bound

to two cyanostars $(\text{CS}_2)\text{S}_2^-$. Observation of the minor species was dependent upon instrument settings (e.g., cone voltage), rather than cyanostar concentration.

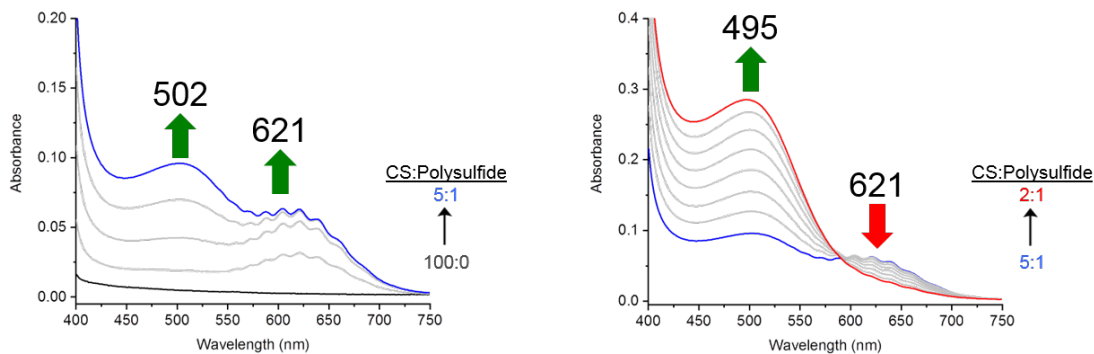


Figure 6.3. Spectra of the UV-Vis titration following the addition of polysulfide to a solution of cyanostar.

The different polysulfide-cyanostar solutions resulted in pronounced color changes. One of those changes involves the growth in an intense blue color that is characteristic of the trisulfur anion radical, $\text{S}_3^{\bullet-}$ [133]. A titration experiment was conducted to characterize these changes. We started with a solution of cyanostar (4 mM) to which was added increasing amounts of lithium polysulfide. Up to a CS:polysulfide ratio of 5:1 (**Figure 6.3**) we see the growth of a highly structured absorption band at 621 nm, consistent with the trisulfur radical anion [133]. Surprisingly, this band showed vibrational fine structure that had not previously been observed in studies of the trisulfur radical. Another component of the color change is associated with a growth in a 500 nm band associated with polysulfides. Addition of further equivalents of polysulfide up to a 2:1 CS:polysulfide ratio results in the loss of the trisulfur peak and the continued growth in the absorption band around 500 nm consistent with the dominance of higher-order polysulfides. While an extensive examination of the distribution of the polysulfide species and their complexes is beyond the scope of this study, this behavior confirms the association of cyanostar with polysulfides while also

showing that cyanostar can moderate the well-known disproportionation reactions of polysulfide.

The UV-Vis data provide some insights on the complexes formed. Complexes of the trisulfur radical appear to form spontaneously and to persist until the ratio of cyanostar:polysulfide is lowered (e.g., 2:1). We propose that with the cyanostar present in excess, e.g., 10:1, dianionic polysulfide species like the heptasulfide will disproportionate to form two trisulfur monoanions in order to maximize the total number of cyanostar-anion interactions. At the higher relative concentrations of polysulfide i.e., 2:1, the speciation shifts from cyanostar-bound complexes of lower-order polysulfides like $(\text{CS}_2)\text{S}_3^{\bullet-}$ to higher-order polysulfides being bound, e.g., $(\text{CS}_4)\text{S}_8^{2-}$. Given the disappearance of the $\text{S}_3^{\bullet-}$ peak in the titrations, the shift in speciation would take place by a comproportionation reaction. This speciation process must be governed by an equilibrium process on account of the fact that similar results were obtained using a reverse titration.

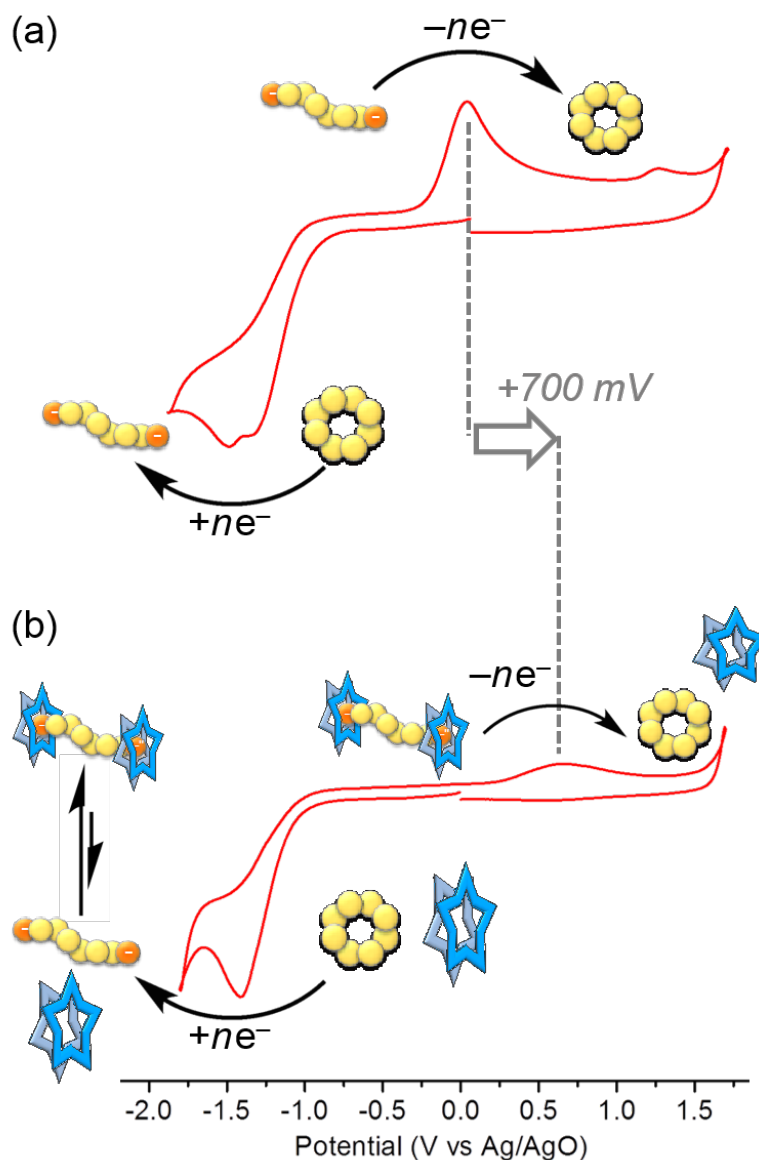


Figure 6.4. Cyclic voltammetry (CV) experiments as a model for sulfur cathodes.

(a) CV sweep of a solution of S_8 . (b) CV sweep of a solution of S_8 with 6 equivalents of cyanostar added. Conditions: 1 mM sulfur (S_8), 0.1 M TBA(TFSI) electrolyte solution (CH_2Cl_2), 1 mm glassy carbon working electrode, platinum wire counter electrode, polished silver wire pseudoreference.

Cyclic voltammetry (CV) experiments were conducted in a three-electrode cell to provide additional insight into the cyanostar-polysulfide association, as shown in

Figure 6.4. In these experiments, the polysulfide anions generated electrochemically by reduction of sulfur (S_8) represent a model of the lithium-sulfur behavior occurring inside the battery during operation. Based upon our previous work [134], the cyanostar was expected to associate with the electrogenerated polysulfide anions. The resulting complexes would then stabilize the polysulfides and produce an anodic shift in the polysulfides re-oxidation potential as well as a characteristic broadening of the peak [135]. In the CV experiments, tetrabutylammonium bistriflimide (TBATFSI) was chosen as the electrolyte in order to match the use of $TFSI^-$ as the anion in battery experiments. The binding of $TFSI^-$ to cyanostar is weak (approximately 10 kJ mol^{-1}) and thus insufficient to compete with polysulfide binding.

Addition of cyanostar alters the polysulfide voltammetry profile in a way that matches our expectations for anion binding. The simplest demonstration of association is shown in methylene chloride (CH_2Cl_2) solutions. CV scans of sulfur (S_8 , 1 mM) alone show the onset of an irreversible multi-electron process from -1.0 V (vs silver wire pseudoreference electrode) with peaks at -1.4 V and -1.6 V, as shown in **Figure 6.4b**. These features are consistent with a multistep reduction of S_8 to S_8^{2-} and then from S_8^{2-} to smaller polysulfides (e.g., S_4^{2-}). A corresponding multielectron process is observed in the anodic sweep at 0.0 V, attributed to the oxidation of polysulfides anions back to sulfur (S_8). Addition of cyanostar results in two distinct changes: Loss in the wave at 0.0 V, and its replacement by a new wave at +0.70 V. Six equivalents of cyanostar (relative to S_8) is sufficient to completely eliminate the oxidation at 0.0 V with the peak at +0.70 V being the only remaining feature in the anodic sweep. Similar results were achieved when the solvent was switched to THF.

This voltammetry data has several important implications. First, it provides corroborating evidence for the binding of polysulfides by cyanostar that was observed in the mass spectrometry and UV-Vis titration experiments. The anodic shift in the re-oxidation potential and the change in peak shape are consistent with the modification of the redox properties of the polysulfide guest upon insertion of the polysulfides into the cavity of the cyanostar macrocycles. These solutions can also be repeatedly

cycled with or without cyanostar, showing that the association and dissociation reactions are fully reversible, controllable by applied voltage, and that the cyanostar is not degraded by the polysulfides. In addition, the magnitude of the anodic shift ($\Delta E = 700$ mV) allows us to estimate the strength of the association between cyanostar and the polysulfides. The stabilization energy of -67.5 kJ mol $^{-1}$ is comparable to the strength of binding to the bromide anion. This similarity correlates with the similar sizes of the anionic terminal sulfide on a polysulfide chain and bromide, and is consistent with the size-selective binding displayed by cyanostar. On account of the strength of association, the cyanostar macrocycle shows a strong preference for polysulfide anions over the more abundant bistriflimide anion (TFSI $^{-}$): Under the experimental conditions used in the CV (100 mM TFSI $^{-}$ and 1 mM S $_x^{2-}$) and the relative binding constants, 97% of cyanostar macrocycles are bound to polysulfides, and only 3% are bound to TFSI $^{-}$. Consequently, cyanostar macrocycles are expected to be chemically selective for polysulfides within a battery, allowing maximum control over the state of complexation of polysulfides, and thus, the extent of their shuttling.

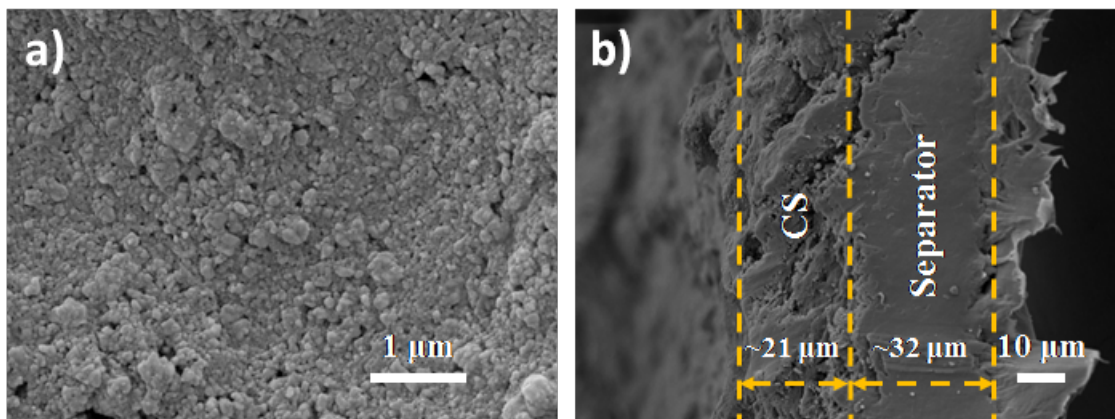


Figure 6.5. SEM image of (a) surface morphology and (b) cross-section.

Transposing the observed solution-phase polysulfide binding into a chemically-selective membrane required the creation of a hybrid separator material. Polypropylene membranes were coated by casting a slurry of cyanostar and polyvinylidene

fluoride (PVdF) as a binder (CS: PVdF = 8: 2). The resulting CS-enhanced membranes were characterized by scanning electron microscopy (SEM) image as shown in **Figure 6.5**. The CS is mixed with the PVdF polymer forming multiple polymer covered particles and a uniform coating layer on the separator. The low magnified SEM image of the CS-coated separator is in **Figure 6.6** showing the uniform contribution of the coating layer. Cross-section of the separator shows a uniform coating of approximately $\sim 21 \mu\text{m}$ on top of the $\sim 32 \mu\text{m}$ separator. This layer of PVdF fully covers the microporous structure of the separator, providing a uniform barrier with CS distributed evenly throughout.

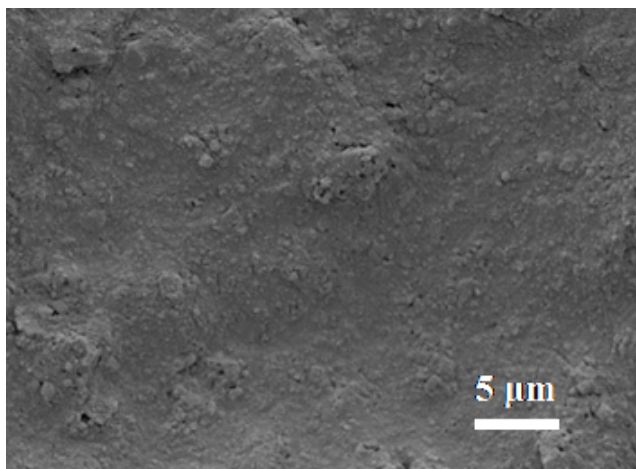


Figure 6.6. Low magnified SEM image of the CS-coated separator.

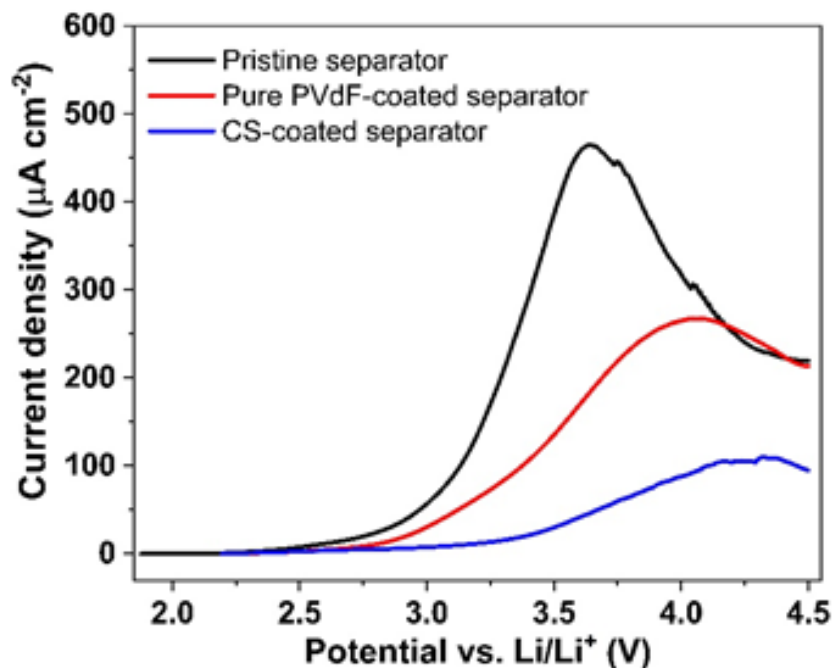


Figure 6.7. Current density-voltage profile of cells with 0.25 M polysulfide solution and pristine Celgard 2400, pure PVdF-coated separator and CS-coated separator at voltage sweeping rate of 1.0 mV s^{-1} .

Suppression of the polysulfide shuttle with CS-enhanced membranes was evaluated by a linear voltage sweep method [136]. Transport of a lithium hexasulfide (Li_2S_6) catholyte across the CS-coated separator is compared with pristine and pure PVdF-coated separator in a custom Swagelok cell in **Figure 6.7**. The obtained anodic current is because of oxidation of lithium polysulfides. A potential is applied to the cell and the voltage swept anodically with the current response attributed to oxidation of lithium polysulfides. When using pristine separators and scanning from the open circuit voltage, the current begins to increase at 2.6 V , indicating the transport of the polysulfide species through the separator with a peak current density $464.6 \mu\text{A cm}^{-2}$ achieved at approximately 3.64 V . The current levels off upon reaching a steady state. When the CS-enhanced separator is present in the cell, the onset of anodic current similarly begins at $\sim 2.6 \text{ V}$, but with a highly reduced peak current density of

$109.5 \mu\text{A cm}^{-2}$, which is reduced by approximately 76.4%. The highly reduced peak current density reflects that the polysulfides species transport is evidently prevented by the CS-coated separator. To exclude the possible shuttle suppression by PVdF polymer, we also evaluate the pure PVdF-coated separator as a comparison. The mass of PVdF on pure PVdF-coated separator is approximately 4.0-4.6 mg, which is almost the sum of masses of CS and PVdF on CS-coated separator. The onset of anodic current begins at ~ 2.7 V with a peak current density of $267.9 \mu\text{A cm}^{-2}$. With a high loading of PVdF, the peak current density is reduced by approximately 42.3%. It can be concluded that with much lower amount of PVdF (1.0-1.2 mg) in CS-coated separator, the polysulfides suppression is major contributed by the CS.

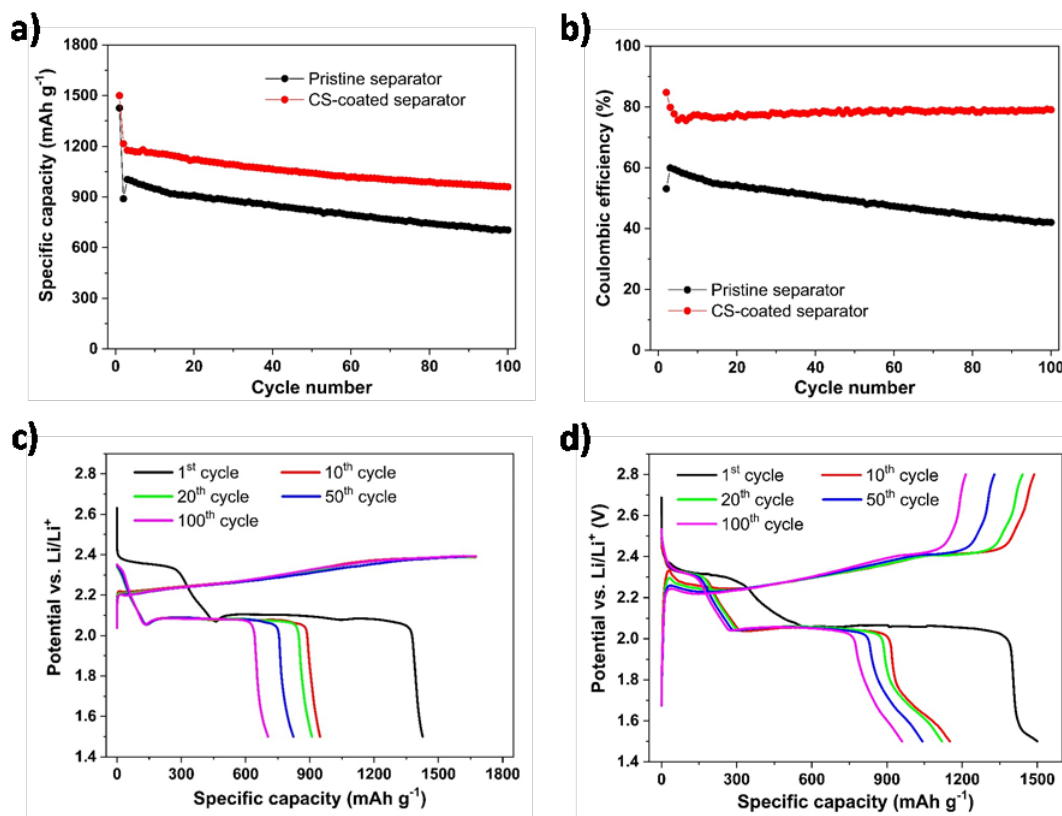


Figure 6.8. (a) Cycling performance and (b) Coulombic efficiency (CE) of cells with pristine separator and CS-coated separator at C/10 rate, selected voltage profile for (c) pristine separator and (b) CS-coated separator in rechargeable lithium batteries.

Cycling performance and electrochemical behaviors are applied to highlight the effectiveness of the CS, as shown in **Figure 6.8**. A control cell with a pristine Celgard 2400 separator is first cycled at C/10 rate with a 1.5 V discharge cut off voltage. Then the charging process was terminated either by a 2.8 V cut off voltage or by a capacity equaling to the theoretical charge capacity, which ever came first ($1.0 \text{ mg S} = 1.672 \text{ mAh}$ theoretical charge capacity, based on the mass of material). This dual-setting limit help us to make sure that the charging process can be terminated even occurring a heavy shuttle effect. The control cell shows an initial capacity of 1426 mAh g^{-1} . After 100 cycles, the capacity drops to 704 mAh g^{-1} with the capacity fading approximately 0.51% per cycle. The Coulombic efficiency (CE) is also poor, starting at 53% and dropping to 42%, demonstrating a severe polysulfide shuttle effect. It has to be noted that a dual-charging limit of reaching either theoretical charge capacity or charge voltage of 2.8 V has been set for the control cells. Without the charge capacity limit, the control cells are not able to be charged even for one cycle. By contrast, cells with CS-coated separators cycled under the same conditions show a smaller capacity fading rate of 0.36% in each cycle, with an initial capacity of 1499 mAh g^{-1} and end capacity of 960 mAh g^{-1} . These cells show improved CEs, which start at 85% and slightly drop to 76% in the first 10 cycles, then stay steady at 79% over the 100 cycles period.

Enhanced separators also facilitate superior charge/discharge properties as well, as shown in selected voltage profiles in **Figure 6.8c** and **d**. The cell with pristine separator is first discharged to 1.5 V, then cycled between 1.5-2.8 V at C/10 rate with a dual-setting limit of the theoretical charge capacity of 1.672 mAh. During the first discharge, the control cell shows two discharge plateaus at 2.36 V and 2.1 V, which correspond to the reduction reactions of sulfur to low-order polysulfides, and then low-order polysulfides to Li_2S . In the following charge process, the cell was kept at the 2.38 V voltage plateau until the theoretical charge capacity was reached. The resulting discharge process has one plateau at 2.08 V, indicating that the discharge product (Li_2S) cannot be fully converted to sulfur, which is attributed

to the polysulfide shuttle. Without the dual-setting limit, the charge process would continue indefinitely without proceeding to next cycle, as it is incapable of recharging. The voltage profile of the cell with the CS-coated separator has discharge plateaus at 2.33 V and 2.06 V in the first cycle. In the following charge process, it has two plateaus at 2.26 V and 2.4 V, with successful conversion back to sulfur and a suppressed shuttle effect.

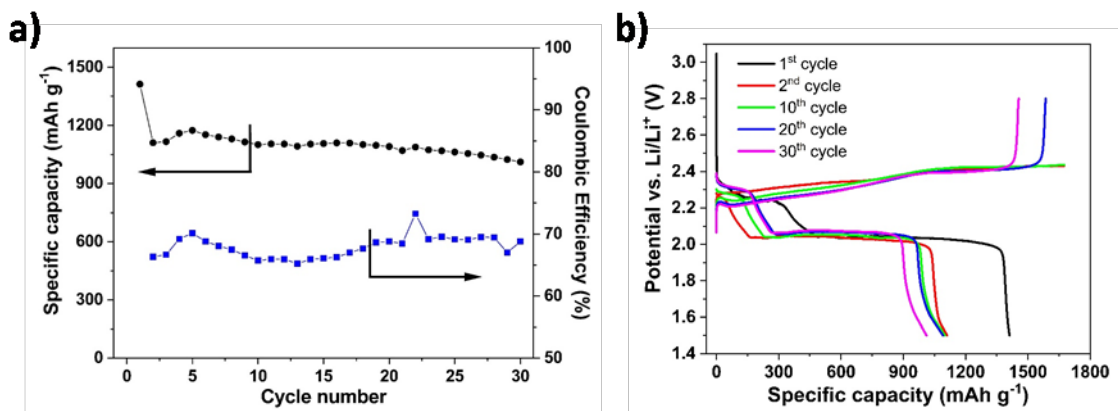


Figure 6.9. (a) Cycling performance and (b) selected voltage profile of cells with pure PVdF-coated separator at C/10 rate.

Other selected control compounds are also tested as comparisons to CS. Pure PVdF is first used to coat the separator, which demonstrates the suppression effect of the polysulfides shuttle by PVdF polymer. Control studies of separators prepared without CS do not show similar improvements in performance. Cells prepared with pure PVdF-coated separators show evidence of a severe shuttle effect with poor average CE of 68%, as shown in **Figure 6.9**. It has to be noted that the cells with pure PVdF-coated separator can finish charging from the 20th cycle. However, the CE is still lower than 70%, which indicates the existing severe shuttle effect. The incomplete charging process is clearly due to the polysulfides shuttle effect. The cell showing complete charging process but still poor value in Coulombic efficiency could be due to the reduced pore size of the separator by the dead sulfur or Li₂S deposited in the separator tunnels. The insulating lost materials slightly alleviate

the shuttle effect. In addition, the PVdF has weak affinity with Li_2S and lithium bis(trifluoromethanesulfonimide) salt, which could provide a weak suppression for the polysulfides species. However, although the charge process can be finished, the CE is extremely low, indicating it as an inefficient method to alleviate shuttle effect.

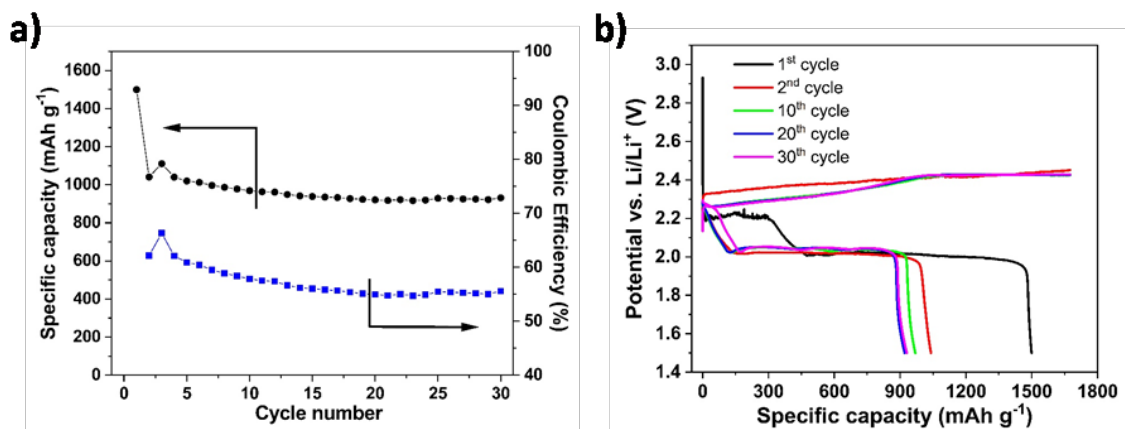


Figure 6.10. (a) Cycling performance and (b) selected voltage profile of cells with curcurbit[6]uril-coated separator at C/10 rate.

A recent report used curcurbit[6]uril as a means to block the shuttle [137], but it showed poor CE of 56% and an infinite high-voltage charging plateau, as shown in **Figure 6.10**. The curcurbit[6]uril does not show any efficient shuttle block mechanisms in this study, which indicates a non-restricted molecule to molecule formation with polysulfides species. On the other hand, the curcurbit[6]uril might work as a physical barrier to alleviate shuttle effect, which is a different study direction from this contribution.

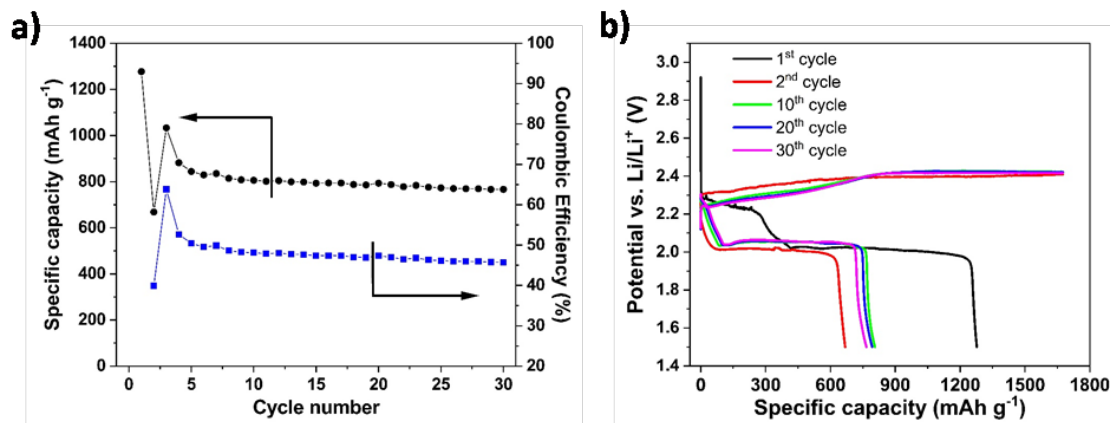


Figure 6.11. (a) Cycling performance and (b) selected voltage profile of cells with β -cyclodextrin-coated separator at C/10 rate.

Another control chemical called β -cyclodextrin is also used as a coating layer on the separator. Similarly, a separator with β -cyclodextrin also shows no improvement, with poor cyclic CE of 47% in incomplete charging in **Figure 6.11**. In comparison to the previous two control experiments, the cell with coated β -cyclodextrin on separator has the lowest CE and worst shuttle block mechanism. Both curcubit[6]uril and β -cyclodextrin are chemicals with similar macrocyclic structure to CS, in which the inner side groups are much different. Our results show that they do not have strong ability to absorb polysulfides, herein to stop the shuttle effect.

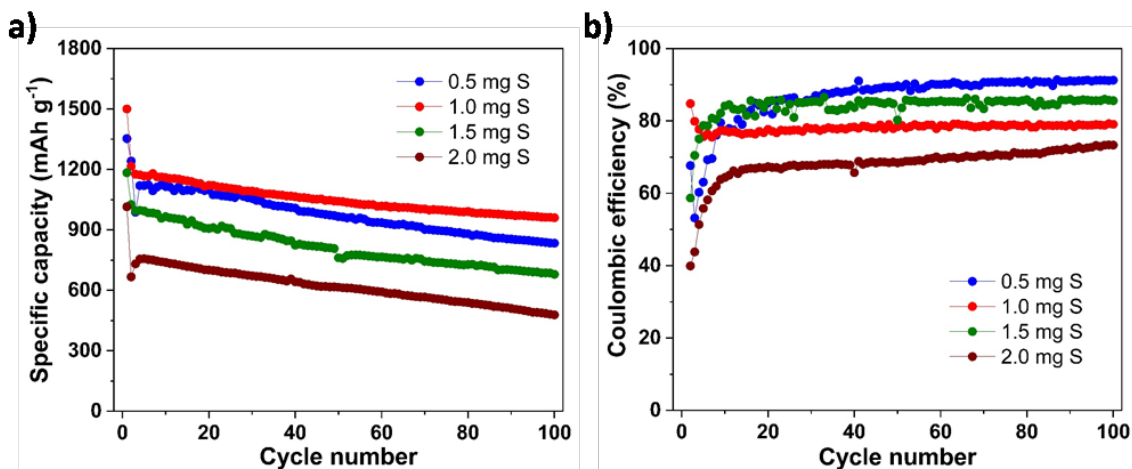


Figure 6.12. (a) Cycling performance and (b) Coulombic efficiencies of cells with variable sulfur loading cathodes and CS-coated separator at C/10 rate.

Cathodes with variable sulfur loadings and same loading of CS on the CS-coated separator are also tested to compare the effect of sulfur amount on shuttle suppression, provided in **Figure 6.12**. Our standard test cells were composed of 5.0-6.0 mg of cyanostar on the separator and 1 mg of sulfur in the cathode. The cathode with S loading of 0.5 mg cm⁻² has the similar performance with that with loading of 1.0 mg cm⁻², which has an initial capacity of 1353 mAh g⁻¹ and an end capacity of 834 mAh g⁻¹. With the increased amount of sulfur to 1.5 mg cm⁻², the delivered capacity is reduced to an initial capacity of 1184 mAh g⁻¹ and end capacity of 680 mAh g⁻¹. When the sulfur loading is further increased to 2.0 mg cm⁻², the initial capacity is only 1014 mAh g⁻¹, with 478 mAh g⁻¹ capacity retaining after 100 cycles. The CEs plots clearly indicate the highest average efficiency of 89% when the sulfur loading is 0.5 mg cm⁻². At the same time, the sulfur cathode with mass loading of 1.5 mg cm⁻² has a CE of 84%, which is close to that with sulfur loading of 1.0 mg cm⁻². The sulfur cathode with mass loading of 2.0 mg cm⁻² has the lowest CE of ~69%. The difference between various sulfur loadings has to be considered by converting and comparing the amounts of sulfur and CS into molecular ratios. The various loadings can be converted into the total number of sulfur atoms (1 mg of Sulfur

$= 1.88 \times 10^{19}$ atoms of sulfur) and then compared to the approximate number of cyanostar molecules (5.0 mg of cyanostar $= 3.29 \times 10^{18}$ macrocycles). The cyanostar-to-sulfur ratios for the various cell compositions are approximately 1:2.9, 1:5.7, 1:8.6, and 1:11.5. The various sulfur amounts could be converted into a specific polysulfide species (e.g. S_6^{2-}) with incorporation of the CS on each separator (5.0-6.0 mg). The approximate molecular ratios of cyanostar-to-sulfur are approximately 2.6:1, 1.3:1, 0.9:1 and 0.6:1 corresponding to sulfur loading of 0.5, 1.0, 1.5 and 2.0 mg cm^{-2} , respectively. Therefore, the cycling performance of sulfur cathode with mass loading of 0.5 mg cm^{-2} has the highest CE, and similar cycling performance to that with sulfur loading of 1.0 mg cm^{-2} . Low amount of sulfur will be absorbed by excess amount of CS with showing alleviated shuttle effect. Since the close molecular ratios, the sulfur cathode with mass loading of 1.5 mg cm^{-2} has similar CE to that with sulfur loading of 1.0 mg cm^{-2} , indicating the shuttle suppression by CS. The sulfur cathode with mass loading of 2.0 mg cm^{-2} has the lowest CE due to the insufficient CS absorption to polysulfides. Both cathodes with loading of 1.5 mg cm^{-2} and 2.0 mg cm^{-2} have lower sulfur utilization than that with loading of 0.5 mg cm^{-2} and 1.0 mg cm^{-2} due to the high S loadings. The results indicate the loading of CS has to be above a polysulfide-saturation threshold to absorb all the polysulfides species. When the sulfur is highly excess the CS amount, the shuttle could be severe.

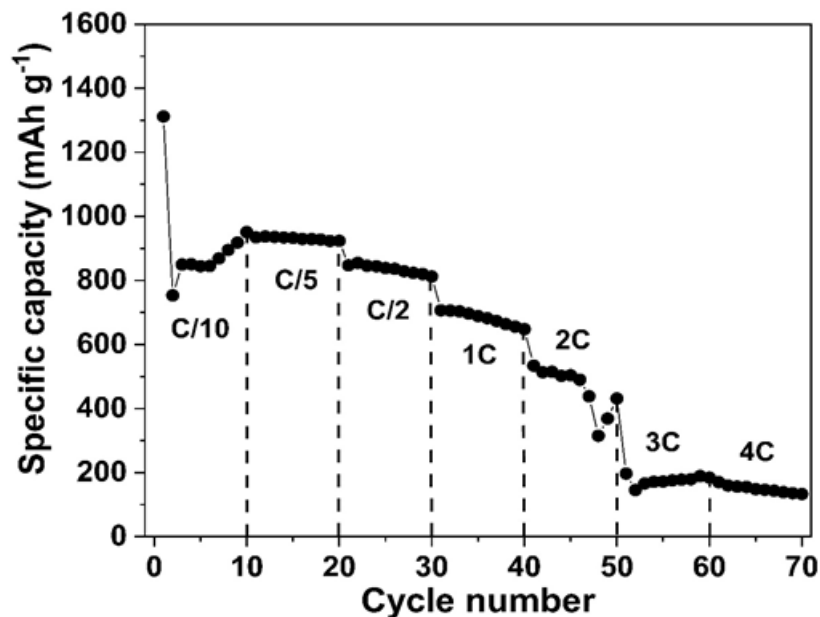


Figure 6.13. Rate performance of cells with 1.0 mg sulfur cathode and CS-coated separator.

The sulfur cathodes (1.0 mg sulfur loading) with CS-coated separator are also tested under variable C-rates, as shown in **Figure 6.13**. It shows an initial capacity of 1312 mAh g⁻¹ at C/10 and 950 mAh g⁻¹ at C/5. The cell exhibits a stable cycling performance with a specific capacity of 847 mAh g⁻¹ at C/2 and 707 mAh g⁻¹ at 1C. With further increase the C-rates, the cell delivers a specific capacity of 534 mAh g⁻¹ at 2C, 197 mAh g⁻¹ at 3C and 170 mAh g⁻¹ at 4C. It can be seen here that the sulfur cathode exhibits stable cycling performance at as low as C/10 rate, and at as high as 1C rate. When the C-rates are further increased, the sulfur utilization is highly decreased, especially at 3C and 4C rates. This is due to the heavy volume changes of sulfur particles during cycling, and the incomplete suppressed dissolved polysulfides. The cycling rate can be further improved by incorporating advanced carbon hosts.

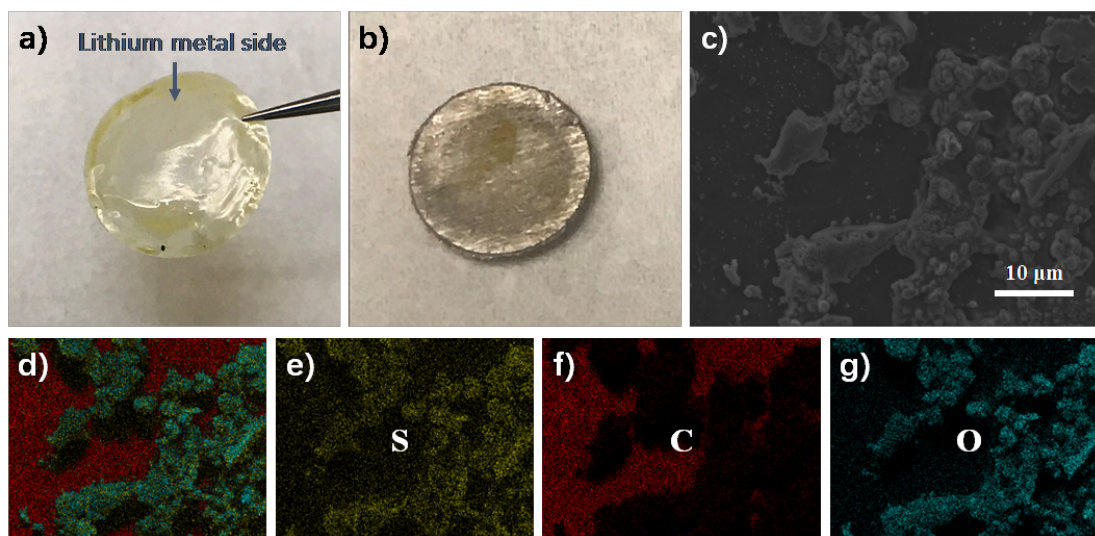


Figure 6.14. (a) Picture of the lithium anode side of the separator, (b) picture of the lithium metal surface, (c) SEM image of the separator of the lithium anode side, EDS showing (d) overlap elemental mapping, (e) sulfur, (f) carbon and (g) oxygen of the cells with pristine separator at discharge state.

To better understand the mechanism of cycling, a study of the morphological changes of the separators after cycling was undertaken by SEM and EDS. When pristine separator was taken from a discharged cell, the discharge product Li_2S is shown on the separator of the lithium metal side indicating the migration of polysulfide species through the separator and the parasitic reaction between the polysulfide and the lithium metal, as shown in **Figure 6.14a**. The lithium anode also develops a film of Li_2S on its surface, as shown in **Figure 6.14b**. By observation via SEM imaging, numerous amounts of solid particles are shown on the separator of the lithium metal side. The SEM images and elemental mapping reveal the presence of Li_2S solid on the anode side. with overlap mapping, elemental mapping of sulfur, carbon and oxygen. The carbon element is mainly from the separator (polypropylene), and the also from the LiTFSI salt. Therefore, the EDS confirms that the particles on the lithium metal side is Li_2S mixed with LiTFSI, which indicates the migration of polysulfide species during discharge.

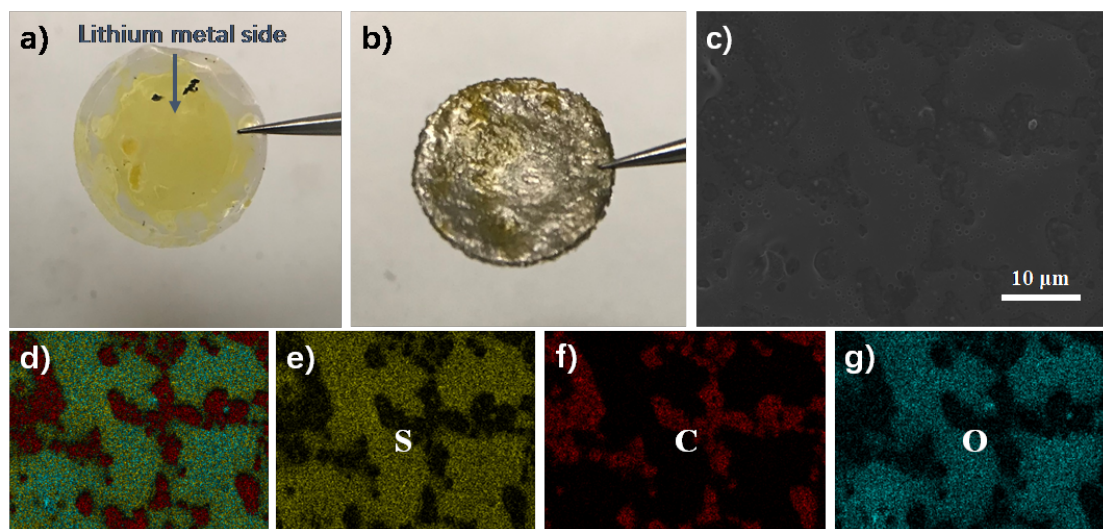


Figure 6.15. (a) Picture of the lithium anode side of the separator, (b) picture of the lithium metal surface, (c) SEM image of the separator of the lithium anode side, EDS showing (d) overlap elemental mapping, (e) sulfur, (f) carbon and (g) oxygen of the cells with pristine separator at charge state.

Even upon charging, polysulfide species persist on the lithium anode side of the separator and the anode itself. The lithium metal taken from charged cell is clearly covered by liquid polysulfides catholyte. It has to be noted that the cells with pristine separator cannot be completely charged, therefore, the ended charging process leads the cell stopping at the severe shuttle happening state and the state of polysulfides rich phases. The SEM image in **Figure 6.15c** shows high amounts of liquid intermediates (polysulfides species) on the separator of the metallic lithium side. The elemental mapping of sulfur confirms that they are the polysulfide species and lithium salt mixture. During charge, the heavy shuttle effect results in polysulfides transporting through the separator and reacting with lithium metal, then being stored at the anode side. Therefore, the polysulfide species are observed on the lithium metal with overlapping mapping, elemental mapping of sulfur, carbon and oxygen are shown in **Figure 6.15d-g**. The presence of sulfur in the anode compartment is the expected

result of polysulfide shuttling through the separator and its retention in the anode compartment.

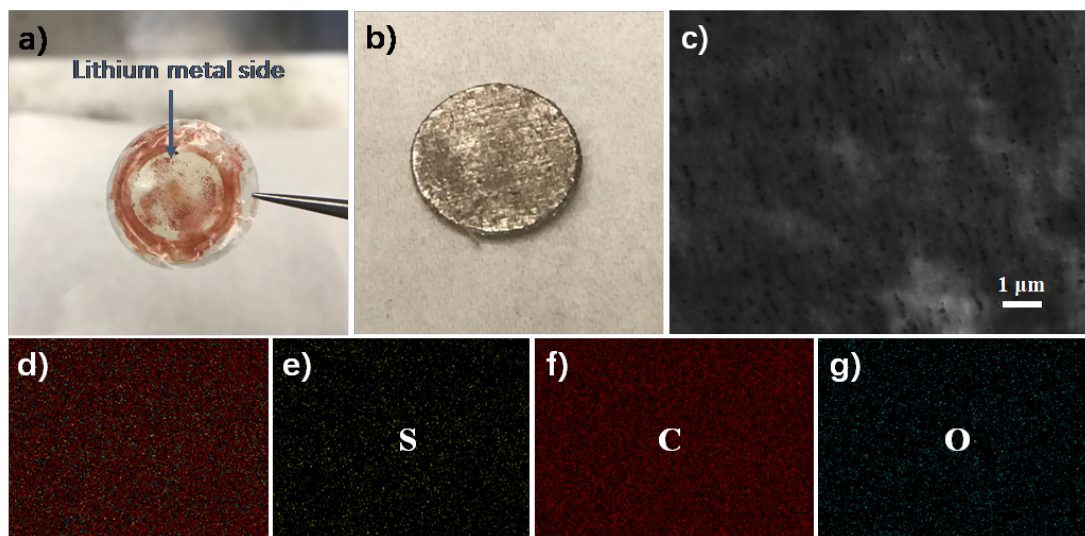


Figure 6.16. (a) Picture of the lithium anode side of the separator, (b) picture of the lithium metal surface, (c) SEM image of the separator of the lithium anode side, EDS showing (d) overlap elemental mapping, (e) sulfur, (f) carbon and (g) oxygen of the cells with CS-coated separator at discharge state.

Conversely, dissection of cells cycled in the presence of a CS-coated separator are free of polysulfide contamination in the anode compartment. The CS-coated separator is first taken from a discharged cell, it can be seen that the lithium metal side of the separator has a clean and smooth surface with rare solid. Furthermore, the lithium anode is also clean of sulfur species following discharge, as shown in **Figure 6.16**. SEM images of the anode side of the separator in **Figure 6.16c** clearly shows the porous structure of the separator without lithium sulfides. Instead, elemental mapping of sulfur shows a uniform background of sulfur which we attributed to the triflate moieties in the electrolyte. The overlap mapping is mostly filled with carbon element, as well as the carbon mapping, which are attributed to the separator. Besides them, the oxygen element is mainly from the triflate salt.

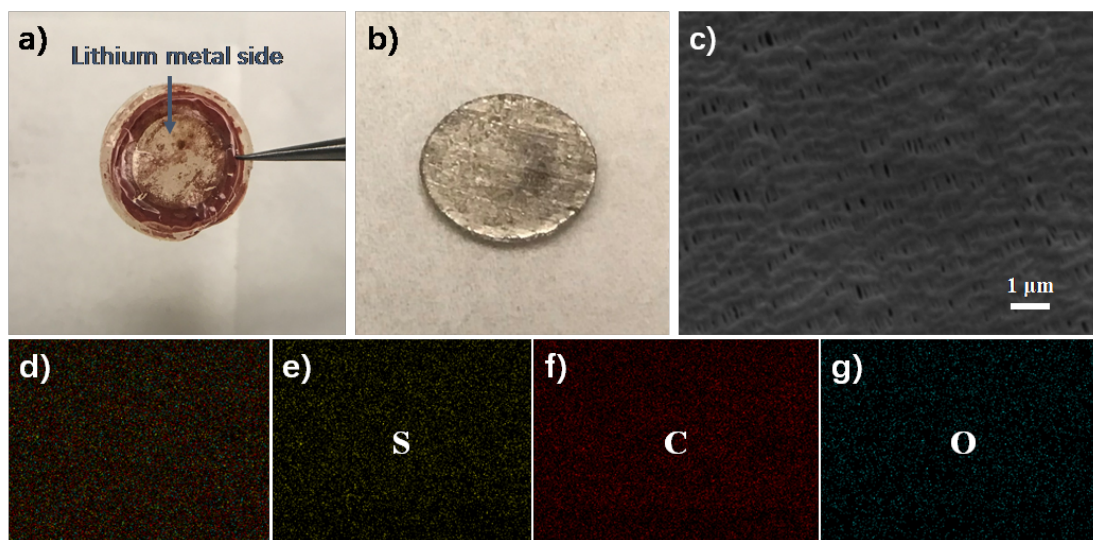


Figure 6.17. (a) Picture of the lithium anode side of the separator, (b) picture of the lithium metal surface, (c) SEM image of the separator of the lithium anode side, EDS showing (d) overlap elemental mapping, (e) sulfur, (f) carbon and (g) oxygen of the cells with CS-coated separator at charge state.

On the other hand, the morphology changes after charge were investigated via SEM. Similarly, no discharge products (sulfur) or polysulfide intermediates can be found on the lithium metal side of the separator or the lithium metal surface, upon charging either, as shown in **Figure 6.17**. The anode side of the CS-coated separator after charging also shows clear porous structure with similar elemental mappings scanned by EDS, as shown in **Figure 6.17d-g**, respectively. Among them, sulfur mapping and oxygen mapping are attributed from the triflate moieties in the electrolyte.

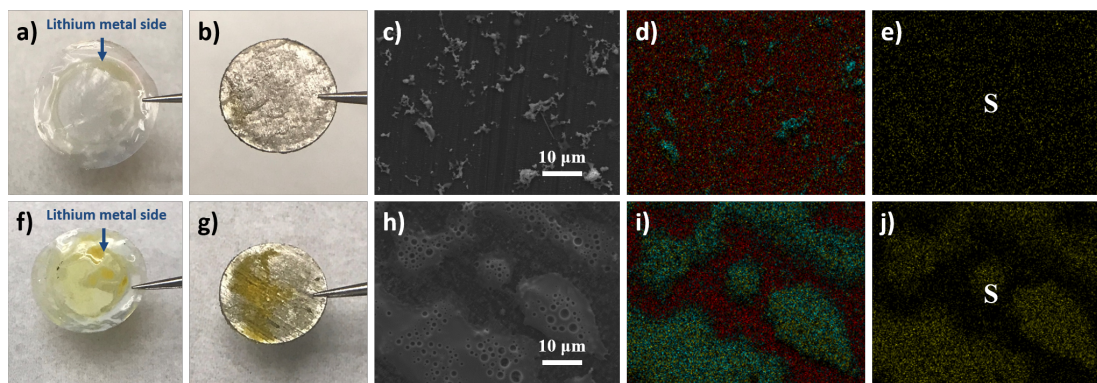


Figure 6.18. Picture of the lithium anode side of the separator at (a) discharge state, (f) charge state, picture of the lithium metal surface at (b) discharge state, (g) charge state, SEM image of the separator of the lithium anode side at (c) discharge state, (h) charge state, EDS showing overlap elemental mapping and sulfur at (d,e) discharge state, (i,j) charge state of the cells with PVdF-coated separator.

In addition, the electrochemical behaviors of the cells with pure PVdF-coated separators provided previously indicate that PVdF has limited effect on the prevention of the polysulfide shuttle. Therefore, the cells with pure PVdF-coated separators were opened and examined by SEM and EDS for morphological changes, as shown in **Figure 6.18a-j**. At the discharge state, yellow color materials are found on the lithium metal side of the PVdF-coated separator and on the lithium metal. With the discovery of materials on the separator in the SEM image, EDS scanning shows the distribution of the overlapped mapping and sulfur mapping, in which the sulfur element could be from the Li_2S and LiTFSI salt. Similarly, at the charged state, excessive dark yellow materials are found on the lithium metal side of the separator and also on the lithium metal. The combination of SEM images and EDS mapping on the lithium metal side of the separator detect high sulfur intensity, which demonstrates the shuttled and transported polysulfides species during charge.

6.5 Conclusion

In this work, we demonstrated a successful approach to suppress polysulfide shuttling in Li-S batteries by creating a chemically-selective barrier composed of a standard polymer separator and a macrocyclic cyanostar anion receptor. Mass spectrometry, UV-Vis titrations and cyclic voltammetry on solution samples all verify inclusion complexes are formed between polysulfides and cyanostar macrocycles. These solution-phase anion-binding properties of the cyanostar could be transferred to the separator by immobilizing the macrocycle in a polymeric PVdF binder layer. Cyanostar-mediated suppression of the polysulfide shuttle improved the Coulombic efficiency from 53% to average 80% compared to pristine separators, and stable cycling was achieved for over 100 cycles at a C/10 rate. This approach was shown to be superior to other non-ionophore macrocyclic hosts in overcoming the problem of the polysulfide shuttle. Future work could focus on improving the release of polysulfides from the cyanostar hybrid membranes and testing the compatibility of the separator with complementary approaches involving improved sulfur cathodes.

7. FUTURE WORK

7.1 Future Work on Solid Polymer Electrolyte (SPE) Project

In conventional lithium-ion batteries, one major challenge is the use of present carbonate-based liquid electrolyte. Damages on batteries shields and electrolyte leaks cause the reactions between the liquid electrolyte with oxygen and moisture in the air, further result in having hydrofluoric acid issues, circuit short and fire concerns. Much effort has been put to develop safer and more reliable electrolyte systems such as solid electrolytes. Among various kinds of solid electrolytes, one class can be classified into ceramic electrolytes including sulfides, oxides and phosphates [138,139]. The second class of solid electrolyte is the polymer electrolytes, which include solid polymer electrolytes and polymer gel electrolytes. On the other hand, some works related to the hybrid electrolytes include both ceramic and polymer also attract much attention. Therefore, the further work could be the development and use of solid polymer electrolyte or hybrid electrolyte.

7.2 Future Work on Liquid Metal Alloy Anode Project

Anode study is extremely important for batteries improvements and future applications. The anode materials which can deliver high comparable capacity and show high safety and stable cycling performance at the same time indicate high potential for real applications. One major study on anode areas is the insertion-based anode materials, such as graphite and $\text{Li}_4\text{Ti}_5\text{O}_{12}$, which show stable cyclability and long life. However, their performance is limited by the low capacity. Another study area is alloy-based anode materials like Co_3O_4 , Si, Ge and Sn metals. They can deliver a much higher capacity than insertion-based anode materials, however, have some lim-

itations such as low ion kinetics, huge volume expansion resulting in poor cycling life. Therefore, liquid metal and liquid alloys are a class of self-healing materials which can deliver high capacity and maintain morphology stability during recycling, also show good cycling performance at the same time.

REFERENCES

REFERENCES

- [1] M. S. Whittingham, "Lithium batteries and cathode materials," *Chemical reviews*, vol. 104, no. 10, pp. 4271–4302, 2004.
- [2] ———, "Electrical energy storage and intercalation chemistry," *Science*, vol. 192, no. 4244, pp. 1126–1127, 1976.
- [3] K. Mizushima, P. Jones, P. Wiseman, and J. B. Goodenough, "Li_xCoO₂ (0 ≤ x ≤ 1): A new cathode material for batteries of high energy density," *Materials Research Bulletin*, vol. 15, no. 6, pp. 783–789, 1980.
- [4] R. Yazami and P. Touzain, "A reversible graphite-lithium negative electrode for electrochemical generators," *Journal of Power Sources*, vol. 9, no. 3, pp. 365–371, 1983.
- [5] A. K. Padhi, K. S. Nanjundaswamy, and J. B. Goodenough, "Phospho-olivines as positive-electrode materials for rechargeable lithium batteries," *Journal of the electrochemical society*, vol. 144, no. 4, pp. 1188–1194, 1997.
- [6] K. M. Shaju and P. G. Bruce, "Macroporous Li (Ni_{1/3}Co_{1/3}Mn_{1/3})O₂: A high-power and high-energy cathode for rechargeable lithium batteries," *Advanced Materials*, vol. 18, no. 17, pp. 2330–2334, 2006.
- [7] M. M. Thackeray, S.-H. Kang, C. S. Johnson, J. T. Vaughey, R. Benedek, and S. Hackney, "Li₂MnO₃-stabilized LiMO₂ (M = Mn, Ni, Co) electrodes for lithium-ion batteries," *Journal of Materials chemistry*, vol. 17, no. 30, pp. 3112–3125, 2007.
- [8] N. Godshall, "Lithium transport in ternary lithium-copper-oxygen cathode materials," *Solid State Ionics*, vol. 18, pp. 788–793, 1986.
- [9] J. Kim and A. Manthiram, "A manganese oxyiodide cathode for rechargeable lithium batteries," *Nature*, vol. 390, no. 6657, p. 265, 1997.
- [10] A. R. Armstrong and P. G. Bruce, "Synthesis of layered LiMnO₂ as an electrode for rechargeable lithium batteries," *Nature*, vol. 381, no. 6582, p. 499, 1996.
- [11] M. S. Whittingham, "The role of ternary phases in cathode reactions," *Journal of The Electrochemical Society*, vol. 123, no. 3, pp. 315–320, 1976.
- [12] C. Delmas, H. Cognac-Auradou, J. Cocciantelli, M. Menetrier, and J. Doumerc, "The Li_xV₂O₅ system: An overview of the structure modifications induced by the lithium intercalation," *Solid State Ionics*, vol. 69, no. 3-4, pp. 257–264, 1994.
- [13] N. Nitta, F. Wu, J. T. Lee, and G. Yushin, "Li-ion battery materials: present and future," *Materials today*, vol. 18, no. 5, pp. 252–264, 2015.

- [14] X. Ji and L. F. Nazar, "Advances in Li-S batteries," *Journal of Materials Chemistry*, vol. 20, no. 44, pp. 9821–9826, 2010.
- [15] Y.-X. Yin, S. Xin, Y.-G. Guo, and L.-J. Wan, "Lithium–sulfur batteries: electrochemistry, materials, and prospects," *Angewandte Chemie International Edition*, vol. 52, no. 50, pp. 13 186–13 200, 2013.
- [16] L.-C. Zeng, W.-H. Li, Y. Jiang, and Y. Yu, "Recent progress in Li–S and Li–Se batteries," *Rare Metals*, vol. 36, no. 5, pp. 339–364, 2017.
- [17] A. Manthiram, Y. Fu, S.-H. Chung, C. Zu, and Y.-S. Su, "Rechargeable lithium–sulfur batteries," *Chemical reviews*, vol. 114, no. 23, pp. 11 751–11 787, 2014.
- [18] A. Abouimrane, D. Dambournet, K. W. Chapman, P. J. Chupas, W. Weng, and K. Amine, "A new class of lithium and sodium rechargeable batteries based on selenium and selenium–sulfur as a positive electrode," *Journal of the American Chemical Society*, vol. 134, no. 10, pp. 4505–4508, 2012.
- [19] C.-P. Yang, S. Xin, Y.-X. Yin, H. Ye, J. Zhang, and Y.-G. Guo, "An advanced selenium–carbon cathode for rechargeable lithium–selenium batteries," *Angewandte Chemie International Edition*, vol. 52, no. 32, pp. 8363–8367, 2013.
- [20] J. B. Goodenough and Y. Kim, "Challenges for rechargeable Li batteries," *Chemistry of materials*, vol. 22, no. 3, pp. 587–603, 2009.
- [21] J. Newman, "Karen. e thomas-alyea. electrochemical systems," 2012.
- [22] J. B. Goodenough and K.-S. Park, "The li-ion rechargeable battery: a perspective," *Journal of the American Chemical Society*, vol. 135, no. 4, pp. 1167–1176, 2013.
- [23] A. Manthiram, "Materials challenges and opportunities of lithium ion batteries," *The Journal of Physical Chemistry Letters*, vol. 2, no. 3, pp. 176–184, 2011.
- [24] B. Liu, J.-G. Zhang, and W. Xu, "Advancing lithium metal batteries," *Joule*, vol. 2, no. 5, pp. 833–845, 2018.
- [25] B. Liu, R. Fang, D. Xie, W. Zhang, H. Huang, Y. Xia, X. Wang, X. Xia, and J. Tu, "Revisiting scientific issues for industrial applications of lithium–sulfur batteries," *Energy & Environmental Materials*, vol. 1, no. 4, pp. 196–208, 2018.
- [26] P. G. Bruce, S. A. Freunberger, L. J. Hardwick, and J.-M. Tarascon, "Li–O₂ and Li–S batteries with high energy storage," *Nature materials*, vol. 11, no. 1, p. 19, 2012.
- [27] M. Barghamadi, A. Kapoor, and C. Wen, "A review on Li-S batteries as a high efficiency rechargeable lithium battery," *Journal of the Electrochemical Society*, vol. 160, no. 8, pp. A1256–A1263, 2013.
- [28] Y.-J. Li, J.-M. Fan, M.-S. Zheng, and Q.-F. Dong, "A novel synergistic composite with multi-functional effects for high-performance Li–S batteries," *Energy & Environmental Science*, vol. 9, no. 6, pp. 1998–2004, 2016.

- [29] M. Wu, Y. Cui, and Y. Fu, “Li₂S nanocrystals confined in free-standing carbon paper for high performance lithium–sulfur batteries,” *ACS applied materials & interfaces*, vol. 7, no. 38, pp. 21 479–21 486, 2015.
- [30] Y. V. Mikhaylik, I. Kovalev, R. Schock, K. Kumaresan, J. Xu, and J. Affinito, “High energy rechargeable li-s cells for ev application: status, remaining problems and solutions,” *Ecs Transactions*, vol. 25, no. 35, pp. 23–34, 2010.
- [31] Z. Li, J. T. Zhang, Y. M. Chen, J. Li, and X. W. D. Lou, “Pie-like electrode design for high-energy density lithium–sulfur batteries,” *Nature communications*, vol. 6, p. 8850, 2015.
- [32] M. A. Pope and I. A. Aksay, “Structural design of cathodes for Li-S batteries,” *Advanced Energy Materials*, vol. 5, no. 16, p. 1500124, 2015.
- [33] W. Guo and Y. Fu, “A perspective on energy densities of rechargeable Li-S batteries and alternative sulfur-based cathode materials,” *Energy & Environmental Materials*, vol. 1, no. 1, pp. 20–27, 2018.
- [34] M. Hagen, P. Fanz, and J. Tübke, “Cell energy density and electrolyte/sulfur ratio in Li–S cells,” *Journal of Power Sources*, vol. 264, pp. 30–34, 2014.
- [35] L. Luo and A. Manthiram, “Rational design of high-loading sulfur cathodes with a poached-egg-shaped architecture for long-cycle lithium–sulfur batteries,” *ACS Energy Letters*, vol. 2, no. 10, pp. 2205–2211, 2017.
- [36] S. Zhang, “Improved cyclability of liquid electrolyte lithium/sulfur batteries by optimizing electrolyte/sulfur ratio,” *Energies*, vol. 5, no. 12, pp. 5190–5197, 2012.
- [37] F. Y. Fan and Y.-M. Chiang, “Electrodeposition kinetics in Li-S batteries: Effects of low electrolyte/sulfur ratios and deposition surface composition,” *Journal of The Electrochemical Society*, vol. 164, no. 4, pp. A917–A922, 2017.
- [38] Y. Liang, Z. Tao, and J. Chen, “Organic electrode materials for rechargeable lithium batteries,” *Advanced Energy Materials*, vol. 2, no. 7, pp. 742–769, 2012.
- [39] P. Sang, Y. Si, and Y. Fu, “Polyphenyl polysulfide: A new polymer cathode material for Li-S battery,” *Chemical Communications*, 2019.
- [40] D.-Y. Wang, Y. Si, J. Li, and Y. Fu, “Tuning the electrochemical behavior of organodisulfides in rechargeable lithium batteries by n-containing heterocycles,” *Journal of Materials Chemistry A*, 2019.
- [41] Y. Cui, J. D. Ackerson, Y. Ma, A. Bhargav, J. A. Karty, W. Guo, L. Zhu, and Y. Fu, “Phenyl selenosulfides as cathode materials for rechargeable lithium batteries,” *Advanced Functional Materials*, vol. 28, no. 31, p. 1801791, 2018.
- [42] W. Guo, A. Bhargav, J. D. Ackerson, Y. Cui, Y. Ma, and Y. Fu, “Mixture is better: enhanced electrochemical performance of phenyl selenosulfide in rechargeable lithium batteries,” *Chemical Communications*, vol. 54, no. 64, pp. 8873–8876, 2018.
- [43] Y. Ma, “Computer simulation of cathode materials for lithium ion and lithium batteries: A review,” *Energy & Environmental Materials*, vol. 1, no. 3, pp. 148–173, 2018.

- [44] W. Guo, Z. D. Wawrzyniakowski, M. M. Cerda, A. Bhargav, M. D. Pluth, Y. Ma, and Y. Fu, "Bis (aryl) tetrasulfides as cathode materials for rechargeable lithium batteries," *Chemistry—A European Journal*, vol. 23, no. 67, pp. 16 941–16 947, 2017.
- [45] A. Bhargav, S. V. Patil, and Y. Fu, "A phenyl disulfide@ cnt composite cathode for rechargeable lithium batteries," *Sustainable Energy & Fuels*, vol. 1, no. 5, pp. 1007–1012, 2017.
- [46] S. S. Zhang, "Liquid electrolyte lithium/sulfur battery: fundamental chemistry, problems, and solutions," *Journal of Power Sources*, vol. 231, pp. 153–162, 2013.
- [47] D. Lin, Y. Liu, and Y. Cui, "Reviving the lithium metal anode for high-energy batteries," *Nature nanotechnology*, vol. 12, no. 3, p. 194, 2017.
- [48] P. Balakrishnan, R. Ramesh, and T. P. Kumar, "Safety mechanisms in lithium-ion batteries," *Journal of Power Sources*, vol. 155, no. 2, pp. 401–414, 2006.
- [49] A. Bhargav, M. Wu, and Y. Fu, "A graphite-polysulfide full cell with dme-based electrolyte," *Journal of The Electrochemical Society*, vol. 163, no. 8, pp. A1543–A1549, 2016.
- [50] U. Von Sacken, E. Nodwell, A. Sundler, and J. Dahn, "Comparative thermal stability of carbon intercalation anodes and lithium metal anodes for rechargeable lithium batteries," *Solid State Ionics*, vol. 69, no. 3-4, pp. 284–290, 1994.
- [51] S. Mori, H. Asahina, H. Suzuki, A. Yonei, and K. Yokoto, "Chemical properties of various organic electrolytes for lithium rechargeable batteries: 1. characterization of passivating layer formed on graphite in alkyl carbonate solutions," *Journal of power sources*, vol. 68, no. 1, pp. 59–64, 1997.
- [52] J. Hassoun, P. Reale, S. Panero, B. Scrosati, M. Wachtler, M. Fleischhammer, M. Kasper, and M. Wohlfahrt-Mehrens, "Determination of the safety level of an advanced lithium ion battery having a nanostructured sn-c anode, a high voltage lini0. 5mn1. 5o4 cathode, and a polyvinylidene fluoride-based gel electrolyte," *Electrochimica Acta*, vol. 55, no. 13, pp. 4194–4200, 2010.
- [53] M. Liu, D. Zhou, H. Jiang, Y. Ren, F. Kang, and T. Zhao, "A highly-safe lithium-ion sulfur polymer battery with SnO₂ anode and acrylate-based gel polymer electrolyte," *Nano Energy*, vol. 28, pp. 97–105, 2016.
- [54] N. Liu, L. Hu, M. T. McDowell, A. Jackson, and Y. Cui, "Prelithiated silicon nanowires as an anode for lithium ion batteries," *ACS nano*, vol. 5, no. 8, pp. 6487–6493, 2011.
- [55] S. Wu, C. Han, J. Iocozzia, M. Lu, R. Ge, R. Xu, and Z. Lin, "Germanium-based nanomaterials for rechargeable batteries," *Angewandte Chemie International Edition*, vol. 55, no. 28, pp. 7898–7922, 2016.
- [56] W. Li, X. Sun, and Y. Yu, "Si-, ge-, sn-based anode materials for lithium-ion batteries: From structure design to electrochemical performance," *Small Methods*, vol. 1, no. 3, p. 1600037, 2017.

- [57] X. Zhou, T. Li, Y. Cui, Y. Fu, Y. Liu, and L. Zhu, "In situ focused ion beam scanning electron microscope study of microstructural evolution of single tin particle anode for li-ion batteries," *ACS applied materials & interfaces*, vol. 11, no. 2, pp. 1733–1738, 2019.
- [58] X. Zhou, T. Li, Y. Cui, M. L. Meyerson, C. B. Mullins, Y. Liu, and L. Zhu, "In situ focused ion beam-scanning electron microscope study of crack and nanopore formation in germanium particle during (de) lithiation," *ACS Applied Energy Materials*, 2019.
- [59] Z. Chen, I. Belharouak, Y.-K. Sun, and K. Amine, "Titanium-based anode materials for safe lithium-ion batteries," *Advanced Functional Materials*, vol. 23, no. 8, pp. 959–969, 2013.
- [60] Y. Yan, Y.-X. Yin, S. Xin, J. Su, Y.-G. Guo, and L.-J. Wan, "High-safety lithium-sulfur battery with prelithiated si/c anode and ionic liquid electrolyte," *Electrochimica Acta*, vol. 91, pp. 58–61, 2013.
- [61] X. Wang, B. Wang, M. Meyerson, C. Mullins, Y. Fu, L. Zhu, and L. Chen, "A phase-field model integrating reaction-diffusion kinetics and elasto-plastic deformation with application to lithiated selenium-doped germanium electrodes," *International Journal of Mechanical Sciences*, vol. 144, pp. 158–171, 2018.
- [62] Y. He, Z. Chang, S. Wu, and H. Zhou, "Effective strategies for long-cycle life lithium-sulfur batteries," *Journal of Materials Chemistry A*, vol. 6, no. 15, pp. 6155–6182, 2018.
- [63] P. G. Bruce, S. A. Freunberger, L. J. Hardwick, and J.-M. Tarascon, "Li-O₂ and Li-S batteries with high energy storage," *Nature materials*, vol. 11, no. 1, p. 19, 2012.
- [64] A. Manthiram, Y. Fu, and Y.-S. Su, "Challenges and prospects of lithium-sulfur batteries," *Accounts of chemical research*, vol. 46, no. 5, pp. 1125–1134, 2012.
- [65] D. Aurbach, E. Pollak, R. Elazari, G. Salitra, C. S. Kelley, and J. Affinito, "On the surface chemical aspects of very high energy density, rechargeable Li-sulfur batteries," *Journal of The Electrochemical Society*, vol. 156, no. 8, pp. A694–A702, 2009.
- [66] L. Zhang, M. Ling, J. Feng, L. Mai, G. Liu, and J. Guo, "The synergetic interaction between LiNO₃ and lithium polysulfides for suppressing shuttle effect of lithium-sulfur batteries," *Energy Storage Materials*, vol. 11, pp. 24–29, 2018.
- [67] S. S. Zhang, "Role of LiNO₃ in rechargeable lithium/sulfur battery," *Electrochimica Acta*, vol. 70, pp. 344–348, 2012.
- [68] S.-H. Chung and A. Manthiram, "A polyethylene glycol-supported microporous carbon coating as a polysulfide trap for utilizing pure sulfur cathodes in lithium-sulfur batteries," *Advanced Materials*, vol. 26, no. 43, pp. 7352–7357, 2014.
- [69] W. Kong, L. Yan, Y. Luo, D. Wang, K. Jiang, Q. Li, S. Fan, and J. Wang, "Ultrathin mno₂/graphene oxide/carbon nanotube interlayer as efficient polysulfide-trapping shield for high-performance Li-S batteries," *Advanced Functional Materials*, vol. 27, no. 18, p. 1606663, 2017.

- [70] H. Al Salem, G. Babu, C. V. Rao, and L. M. R. Arava, "Electrocatalytic polysulfide traps for controlling redox shuttle process of Li-S batteries," *Journal of the American Chemical Society*, vol. 137, no. 36, pp. 11 542–11 545, 2015.
- [71] Q. Pang, X. Liang, C. Y. Kwok, and L. F. Nazar, "Advances in lithium-sulfur batteries based on multifunctional cathodes and electrolytes," *Nature Energy*, vol. 1, no. 9, p. 16132, 2016.
- [72] Y. Fu and A. Manthiram, "Orthorhombic bipyramidal sulfur coated with polypyrrole nanolayers as a cathode material for lithium-sulfur batteries," *The Journal of Physical Chemistry C*, vol. 116, no. 16, pp. 8910–8915, 2012.
- [73] Z. W. Seh, Q. Zhang, W. Li, G. Zheng, H. Yao, and Y. Cui, "Stable cycling of lithium sulfide cathodes through strong affinity with a bifunctional binder," *Chemical Science*, vol. 4, no. 9, pp. 3673–3677, 2013.
- [74] Y. Cui and Y. Fu, "Enhanced cyclability of Li/polysulfide batteries by a polymer-modified carbon paper current collector," *ACS applied materials & interfaces*, vol. 7, no. 36, pp. 20 369–20 376, 2015.
- [75] G. Ma, Z. Wen, J. Jin, M. Wu, X. Wu, and J. Zhang, "Enhanced cycle performance of Li-S battery with a polypyrrole functional interlayer," *Journal of Power Sources*, vol. 267, pp. 542–546, 2014.
- [76] C.-Y. Chen, H.-J. Peng, T.-Z. Hou, P.-Y. Zhai, B.-Q. Li, C. Tang, W. Zhu, J.-Q. Huang, and Q. Zhang, "A quinonoid-imine-enriched nanostructured polymer mediator for lithium-sulfur batteries," *Advanced Materials*, vol. 29, no. 23, p. 1606802, 2017.
- [77] J. Nelson, S. Misra, Y. Yang, A. Jackson, Y. Liu, H. Wang, H. Dai, J. C. Andrews, Y. Cui, and M. F. Toney, "In operando x-ray diffraction and transmission X-ray microscopy of lithium sulfur batteries," *Journal of the American Chemical Society*, vol. 134, no. 14, pp. 6337–6343, 2012.
- [78] S.-E. Cheon, K.-S. Ko, J.-H. Cho, S.-W. Kim, E.-Y. Chin, and H.-T. Kim, "Rechargeable lithium sulfur battery i. structural change of sulfur cathode during discharge and charge," *Journal of The Electrochemical Society*, vol. 150, no. 6, pp. A796–A799, 2003.
- [79] D.-W. Wang, Q. Zeng, G. Zhou, L. Yin, F. Li, H.-M. Cheng, I. R. Gentle, and G. Q. M. Lu, "Carbon-sulfur composites for Li-S batteries: status and prospects," *Journal of Materials Chemistry A*, vol. 1, no. 33, pp. 9382–9394, 2013.
- [80] A. Eftekhari, "The rise of lithium-selenium batteries," *Sustainable Energy & Fuels*, vol. 1, no. 1, pp. 14–29, 2017.
- [81] H. Ye, Y.-X. Yin, S.-F. Zhang, and Y.-G. Guo, "Advanced Se-C nanocomposites: a bifunctional electrode material for both li-se and li-ion batteries," *Journal of Materials Chemistry A*, vol. 2, no. 33, pp. 13 293–13 298, 2014.
- [82] L. Zeng, W. Zeng, Y. Jiang, X. Wei, W. Li, C. Yang, Y. Zhu, and Y. Yu, "A flexible porous carbon nanofibers-selenium cathode with superior electrochemical performance for both li-se and na-se batteries," *Advanced Energy Materials*, vol. 5, no. 4, p. 1401377, 2015.

- [83] Z. Li, L. Yuan, Z. Yi, Y. Liu, and Y. Huang, "Confined selenium within porous carbon nanospheres as cathode for advanced Li-Se batteries," *Nano Energy*, vol. 9, pp. 229–236, 2014.
- [84] Z. Zhang, X. Yang, Z. Guo, Y. Qu, J. Li, and Y. Lai, "Selenium/carbon-rich core-shell composites as cathode materials for rechargeable lithium-selenium batteries," *Journal of Power Sources*, vol. 279, pp. 88–93, 2015.
- [85] J. Li, X. Zhao, Z. Zhang, and Y. Lai, "Facile synthesis of hollow carbonized polyaniline spheres to encapsulate selenium for advanced rechargeable lithium-selenium batteries," *Journal of Alloys and Compounds*, vol. 619, pp. 794–799, 2015.
- [86] C. Luo, Y. Xu, Y. Zhu, Y. Liu, S. Zheng, Y. Liu, A. Langrock, and C. Wang, "Selenium@ mesoporous carbon composite with superior lithium and sodium storage capacity," *ACS nano*, vol. 7, no. 9, pp. 8003–8010, 2013.
- [87] Y. Liu, L. Si, Y. Du, X. Zhou, Z. Dai, and J. Bao, "Strongly bonded selenium/microporous carbon nanofibers composite as a high-performance cathode for lithium-selenium batteries," *The Journal of Physical Chemistry C*, vol. 119, no. 49, pp. 27 316–27 321, 2015.
- [88] C. Luo, J. Wang, L. Suo, J. Mao, X. Fan, and C. Wang, "In situ formed carbon bonded and encapsulated selenium composites for Li-Se and Na-Se batteries," *Journal of Materials Chemistry A*, vol. 3, no. 2, pp. 555–561, 2015.
- [89] X. Wang, Z. Zhang, Y. Qu, G. Wang, Y. Lai, and J. Li, "Solution-based synthesis of multi-walled carbon nanotube/selenium composites for high performance lithium-selenium battery," *Journal of Power Sources*, vol. 287, pp. 247–252, 2015.
- [90] Y. Qu, Z. Zhang, S. Jiang, X. Wang, Y. Lai, Y. Liu, and J. Li, "Confining selenium in nitrogen-containing hierarchical porous carbon for high-rate rechargeable lithium-selenium batteries," *Journal of Materials Chemistry A*, vol. 2, no. 31, pp. 12 255–12 261, 2014.
- [91] S. Jiang, Z. Zhang, Y. Lai, Y. Qu, X. Wang, and J. Li, "Selenium encapsulated into 3d interconnected hierarchical porous carbon aerogels for lithium-selenium batteries with high rate performance and cycling stability," *Journal of Power Sources*, vol. 267, pp. 394–404, 2014.
- [92] J.-M. Tarascon and M. Armand, "Issues and challenges facing rechargeable lithium batteries," in *Materials for Sustainable Energy: A Collection of Peer-Reviewed Research and Review Articles from Nature Publishing Group*. World Scientific, 2011, pp. 171–179.
- [93] Q. Pang, X. Liang, C. Kwok, and L. F. Nazar, "The importance of chemical interactions between sulfur host materials and lithium polysulfides for advanced lithium-sulfur batteries," *Journal of The Electrochemical Society*, vol. 162, no. 14, pp. A2567–A2576, 2015.
- [94] M. Wu, Y. Cui, A. Bhargav, Y. Losovyj, A. Siegel, M. Agarwal, Y. Ma, and Y. Fu, "Organotrissulfide: A high capacity cathode material for rechargeable lithium batteries," *Angewandte Chemie International Edition*, vol. 55, no. 34, pp. 10 027–10 031, 2016.

- [95] A. Bhargav, Y. Ma, K. Shashikala, Y. Cui, Y. Losovyj, and Y. Fu, “The unique chemistry of thiuram polysulfides enables energy dense lithium batteries,” *Journal of Materials Chemistry A*, vol. 5, no. 47, pp. 25 005–25 013, 2017.
- [96] M. Wu, A. Bhargav, Y. Cui, A. Siegel, M. Agarwal, Y. Ma, and Y. Fu, “Highly reversible diphenyl trisulfide catholyte for rechargeable lithium batteries,” *ACS Energy Letters*, vol. 1, no. 6, pp. 1221–1226, 2016.
- [97] A. Bhargav, M. E. Bell, J. Karty, Y. Cui, and Y. Fu, “A class of organopolysulfides as liquid cathode materials for high-energy-density lithium batteries,” *ACS applied materials & interfaces*, vol. 10, no. 25, pp. 21 084–21 090, 2018.
- [98] M. Hagen, D. Hanselmann, K. Ahlbrecht, R. Maça, D. Gerber, and J. Tübke, “Lithium–sulfur cells: the gap between the state-of-the-art and the requirements for high energy battery cells,” *Advanced Energy Materials*, vol. 5, no. 16, p. 1401986, 2015.
- [99] Z. Jian-Ming, T. M. Johnson, S. K. Clark, and Z. Xiang-Kun, “High precision measurement of selenium isotopic composition by hydride generation multiple collector inductively coupled plasma mass spectrometry with a ^{74}Se - ^{77}Se double spike,” *Chinese Journal of Analytical Chemistry*, vol. 36, no. 10, pp. 1385–1390, 2008.
- [100] A. R. Kamali and D. J. Fray, “Tin-based materials as advanced anode materials for lithium ion batteries: a review,” *Rev. Adv. Mater. Sci.*, vol. 27, no. 1, pp. 14–24, 2011.
- [101] S. Goriparti, E. Miele, F. De Angelis, E. Di Fabrizio, R. P. Zaccaria, and C. Capiglia, “Review on recent progress of nanostructured anode materials for Li-ion batteries,” *Journal of power sources*, vol. 257, pp. 421–443, 2014.
- [102] G. Ehrlich, C. Durand, X. Chen, T. Hugener, F. Spiess, and S. Suib, “Metallic negative electrode materials for rechargeable nonaqueous batteries,” *Journal of The Electrochemical Society*, vol. 147, no. 3, pp. 886–891, 2000.
- [103] L. Beaulieu, K. Eberman, R. Turner, L. Krause, and J. Dahn, “Colossal reversible volume changes in lithium alloys,” *Electrochemical and Solid-State Letters*, vol. 4, no. 9, pp. A137–A140, 2001.
- [104] F. Xin, X. Wang, J. Bai, W. Wen, H. Tian, C. Wang, and W. Han, “A lithiation/delithiation mechanism of monodispersed MSn_5 ($\text{M} = \text{Fe}, \text{Co}$ and FeCo) nanospheres,” *Journal of Materials Chemistry A*, vol. 3, no. 13, pp. 7170–7178, 2015.
- [105] Y. Xu, Q. Liu, Y. Zhu, Y. Liu, A. Langrock, M. R. Zachariah, and C. Wang, “Uniform nano-Sn/C composite anodes for lithium ion batteries,” *Nano letters*, vol. 13, no. 2, pp. 470–474, 2013.
- [106] K. J. Rhodes, R. Meisner, M. Kirkham, N. Dudney, and C. Daniel, “In situ xrd of thin film tin electrodes for lithium ion batteries,” *Journal of The Electrochemical Society*, vol. 159, no. 3, pp. A294–A299, 2012.
- [107] J. Hassoun, S. Panero, P. Reale, and B. Scrosati, “A new type of lithium-ion battery based on tin electroplated negative electrodes,” *Int. J. Electrochem. Sci.*, vol. 1, no. 3, pp. 110–121, 2006.

- [108] N. Tamura, R. Ohshita, M. Fujimoto, S. Fujitani, M. Kamino, and I. Yonezu, "Study on the anode behavior of Sn and Sn–Cu alloy thin-film electrodes," *Journal of Power Sources*, vol. 107, no. 1, pp. 48–55, 2002.
- [109] S. Yang, P. Y. Zavalij, and M. S. Whittingham, "Anodes for lithium batteries: tin revisited," *Electrochemistry communications*, vol. 5, no. 7, pp. 587–590, 2003.
- [110] K. J. Kreder III, B. T. Heligman, and A. Manthiram, "Interdigitated eutectic alloy foil anodes for rechargeable batteries," *ACS Energy Letters*, vol. 2, no. 10, pp. 2422–2423, 2017.
- [111] J. Hassoun, J. Kim, D.-J. Lee, H.-G. Jung, S.-M. Lee, Y.-K. Sun, and B. Scrosati, "A contribution to the progress of high energy batteries: A metal-free, lithium-ion, silicon–sulfur battery," *Journal of Power Sources*, vol. 202, pp. 308–313, 2012.
- [112] S. M. Wood, E. J. Powell, A. Heller, and C. B. Mullins, "Lithiation and delithiation of lead sulfide (PbS)," *Journal of The Electrochemical Society*, vol. 162, no. 7, pp. A1182–A1185, 2015.
- [113] J. Hassoun and B. Scrosati, "A high-performance polymer tin sulfur lithium ion battery," *Angewandte Chemie International Edition*, vol. 49, no. 13, pp. 2371–2374, 2010.
- [114] Y. Cui, T. Li, X. Zhou, A. Mosey, W. Guo, R. Cheng, Y. Fu, and L. Zhu, "Electrochemical behavior of tin foil anode in half cell and full cell with sulfur cathode," *Electrochimica Acta*, vol. 294, pp. 60–67, 2019.
- [115] J. Yang, Y. Takeda, N. Imanishi, and O. Yamamoto, "Ultrafine Sn and SnSb_{0.14} powders for lithium storage matrices in lithium-ion batteries," *Journal of The Electrochemical Society*, vol. 146, no. 11, pp. 4009–4013, 1999.
- [116] M. Winter and J. O. Besenhard, "Electrochemical lithiation of tin and tin-based intermetallics and composites," *Electrochimica Acta*, vol. 45, no. 1-2, pp. 31–50, 1999.
- [117] T. Ichitsubo, S. Yukitani, K. Hirai, S. Yagi, T. Uda, and E. Matsubara, "Mechanical-energy influences to electrochemical phenomena in lithium-ion batteries," *Journal of Materials Chemistry*, vol. 21, no. 8, pp. 2701–2708, 2011.
- [118] Y. Cui, M. Wu, C. Scott, J. Xie, and Y. Fu, "A binder-free sulfur/carbon composite electrode prepared by a sulfur sublimation method for Li–S batteries," *RSC Advances*, vol. 6, no. 58, pp. 52 642–52 645, 2016.
- [119] Y. Cui, A. Abouimrane, C.-J. Sun, Y. Ren, and K. Amine, "Li–Se battery: absence of lithium polyselenides in carbonate based electrolyte," *Chemical Communications*, vol. 50, no. 42, pp. 5576–5579, 2014.
- [120] J. Zhang, Y. Xu, L. Fan, Y. Zhu, J. Liang, and Y. Qian, "Graphene-encapsulated selenium/polyaniline core-shell nanowires with enhanced electrochemical performance for Li–Se batteries," *Nano Energy*, vol. 13, pp. 592–600, 2015.

- [121] J. He, Y. Chen, W. Lv, K. Wen, P. Li, Z. Wang, W. Zhang, W. Qin, and W. He, "Three-dimensional hierarchical graphene-cnt@ se: a highly efficient freestanding cathode for Li-Se batteries," *ACS Energy Letters*, vol. 1, no. 1, pp. 16–20, 2016.
- [122] Y. Cui, X. Zhou, W. Guo, Y. Liu, T. Li, Y. Fu, and L. Zhu, "Selenium nanocomposite cathode with long cycle life for rechargeable lithium-selenium batteries," *Batteries & Supercaps*, 2019.
- [123] A. N. Mistry and P. P. Mukherjee, "shuttle in polysulfide shuttle: Friend or foe?" *The Journal of Physical Chemistry C*, vol. 122, no. 42, pp. 23 845–23 851, 2018.
- [124] X. Fan, W. Sun, F. Meng, A. Xing, and J. Liu, "Advanced chemical strategies for lithium-sulfur batteries: A review," *Green Energy & Environment*, vol. 3, no. 1, pp. 2–19, 2018.
- [125] M. Barghamadi, A. Kapoor, and C. Wen, "A review on Li-S batteries as a high efficiency rechargeable lithium battery," *Journal of the Electrochemical Society*, vol. 160, no. 8, pp. A1256–A1263, 2013.
- [126] A. N. Mistry and P. P. Mukherjee, "Electrolyte transport evolution dynamics in lithium-sulfur batteries," *The Journal of Physical Chemistry C*, vol. 122, no. 32, pp. 18 329–18 335, 2018.
- [127] A. Eftekhari and D.-W. Kim, "Cathode materials for lithium-sulfur batteries: a practical perspective," *Journal of Materials Chemistry A*, vol. 5, no. 34, pp. 17 734–17 776, 2017.
- [128] Z.-Z. Yang, H.-Y. Wang, L. Lu, C. Wang, X.-B. Zhong, J.-G. Wang, and Q.-C. Jiang, "Hierarchical TiO₂ spheres as highly efficient polysulfide host for lithium-sulfur batteries," *Scientific reports*, vol. 6, p. 22990, 2016.
- [129] H. Al Salem, V. R. Chitturi, G. Babu, J. A. Santana, D. Gopalakrishnan, and L. M. R. Arava, "Stabilizing polysulfide-shuttle in a Li-S battery using transition metal carbide nanostructures," *RSC Advances*, vol. 6, no. 111, pp. 110 301–110 306, 2016.
- [130] S. Lee, C.-H. Chen, and A. H. Flood, "A pentagonal cyanostar macrocycle with cyanostilbene CH donors binds anions and forms dialkylphosphate [3] rotaxanes," *Nature chemistry*, vol. 5, no. 8, p. 704, 2013.
- [131] E. M. Fatila, M. Pink, E. B. Twum, J. A. Karty, and A. H. Flood, "Phosphate-phosphate oligomerization drives higher order co-assemblies with stacks of cyanostar macrocycles," *Chemical Science*, vol. 9, no. 11, pp. 2863–2872, 2018.
- [132] R. Rauh, F. Shuker, J. Marston, and S. Brummer, "Formation of lithium polysulfides in aprotic media," *Journal of Inorganic and Nuclear Chemistry*, vol. 39, no. 10, pp. 1761–1766, 1977.
- [133] T. Chivers and P. J. Elder, "Ubiquitous trisulfur radical anion: fundamentals and applications in materials science, electrochemistry, analytical chemistry and geochemistry," *Chemical Society Reviews*, vol. 42, no. 14, pp. 5996–6005, 2013.

- [134] C. R. Benson, E. M. Fatila, S. Lee, M. G. Marzo, M. Pink, M. B. Mills, K. E. Preuss, and A. H. Flood, "Extreme stabilization and redox switching of organic anions and radical anions by large-cavity, CH hydrogen-bonding cyanostar macrocycles," *Journal of the American Chemical Society*, vol. 138, no. 45, pp. 15 057–15 065, 2016.
- [135] W. S. Jeon, K. Moon, S. H. Park, H. Chun, Y. H. Ko, J. Y. Lee, E. S. Lee, S. Samal, N. Selvapalam, M. V. Rekharsky *et al.*, "Complexation of ferrocene derivatives by the cucurbit [7] uril host: a comparative study of the cucurbituril and cyclodextrin host families," *Journal of the American Chemical Society*, vol. 127, no. 37, pp. 12 984–12 989, 2005.
- [136] Y. Cui and Y. Fu, "Polysulfide transport through separators measured by a linear voltage sweep method," *Journal of Power Sources*, vol. 286, pp. 557–560, 2015.
- [137] J. Xie, H.-J. Peng, J.-Q. Huang, W.-T. Xu, X. Chen, and Q. Zhang, "A supramolecular capsule for reversible polysulfide storage/delivery in lithium-sulfur batteries," *Angewandte Chemie International Edition*, vol. 56, no. 51, pp. 16 223–16 227, 2017.
- [138] Q. Liu, Z. Geng, C. Han, Y. Fu, S. Li, Y.-b. He, F. Kang, and B. Li, "Challenges and perspectives of garnet solid electrolytes for all solid-state lithium batteries," *Journal of Power Sources*, vol. 389, pp. 120–134, 2018.
- [139] T. Li, H. Kang, X. Zhou, C. Lim, B. Yan, V. De Andrade, F. De Carlo, and L. Zhu, "Three-dimensional reconstruction and analysis of all-solid li-ion battery electrode using synchrotron transmission X-ray microscopy tomography," *ACS applied materials & interfaces*, vol. 10, no. 20, pp. 16 927–16 931, 2018.

VITA

VITA

Yi Cui was born in Liaoning, China. He received his B.S. in Polymer Material Science and Engineering from Beijing University of Chemical Technology (BUCT) in 2011. Then he went to Worcester Polytechnic Institute (WPI) as a masters student and worked on the study of 3-D printing materials and technology. After he got his M.S. degree from WPI in 2014, he joined Purdue University and received his second M.S. degree in Mechanical Engineering in 2016. He is currently pursuing his Ph.D. degree in the School of Mechanical Engineering at Purdue University. His research focuses on the development of the Li-S and Li-Se batteries electrode materials, membrane materials for Li-S batteries, and development of metal and alloy anode materials for lithium batteries. He has more than 20 peer reviewed papers and conference presentations in total during his Ph.D. study.